IPP-Report

Max-Planck-Institut
für Plasmaphysik

Sofía Aurora Díaz Esteban

Investigations of the Structure of the Electron Temperature Profile around the Separatrix with the Thermal Helium Beam Diagnostic at ASDEX Upgrade

IPP 2021-13
September 2021

Master's Thesis in
Applied and Engineering Physics
at Technische Universität München

Investigation of the Structure of the Electron Temperature Profile around the Separatrix with the Thermal Helium Beam Diagnostic at ASDEX Upgrade

Author:	Sofía Aurora Díaz Esteban
Submission Date:	May 31st, 2021
First Promoter:	Prof. Dr. Ulrich Stroth
Second Promoter:	Prof. Dr. Rudolf Neu
IPP Supervisor:	Prof. Dr. Elisabeth Wolfrum
IPP Supervisor:	Dr. Michael Griener

Max-Planck-Institut für Plasmaphysik

Abstract

In a scenario of global warming and increasing world population, there is a clear motivation to develop fusion power plants as a long-term solution to the world's energy needs. One of the most advanced options to achieve fusion power is a tokamak, a toroidal chamber that confines the high-temperature plasma by a set of toroidally symmetric magnetic coils combined with a strong current flowing in the plasma itself. The power flux across the boundary of a magnetically confined plasma in steady-state is the sum of the externally induced heating plus the power of the fusion reactions in the plasma's core minus the radiation power and the produced neutrons. This power leaves the region of closed field lines by crossing the separatrix and entering the region of open field lines, the so-called scrape-off layer (SOL). The power and temperature decay widths in the near SOL ($\lambda_{q_{\|\mathrm{e}}}$, λ_{T_e}) characterise this heat flux since they reflect the ratio between the transport parallel to the magnetic field lines down to the divertor due to Spitzer-Härm electron conduction and the perpendicular transport along the major radius involving anomalous transport processes. In order to improve the knowledge of the behaviour of these quantities, a thermal helium beam (THB) diagnostic with superior spatiotemporal resolution has been implemented in the ASDEX Upgrade (AUG) tokamak. In this thesis, a database of high (H-mode) and low confinement (L-mode) regimes is built to analyse the near SOL electron temperature and density profiles directly measured with the THB. The aim of this thesis is to study the structure of the electron temperature profile within the database and to investigate the near SOL temperature fall-off lengths measured by the THB diagnostic and compare them with the already established Thomson scattering (TS) system at AUG.

A match between the point of highest positive curvature of the THB temperature profiles and the position of the separatrix predicted by magnetic reconstruction is seen for the complete H-mode database. These experimental findings are supported by the results from a 1.5 D modelling of the heat balance equation from closed to open field lines with a full perpendicular description and an assumption-limited parallel sink term. Regarding the temperature fall-off lengths, it can be seen that the obtained values with the THB data are not constant around the separatrix due to the transport changes. The measured fall-off lengths present the dependencies established by the Goldston scaling: an inverse relation with the plasma current and no dependence on the heating power. For the comparison with the edge Thomson scattering system, similar THB and TS fall-off length values are obtained when the chosen radial ranges for evaluating the two different diagnostics overlap.

Zusammenfassung

In einem Szenario von globaler Erwärmung und wachsender Weltbevölkerung gibt es eine klare Motivation, Kernfusionskraftwerke als eine langfristige Lösung für den Energiebedarf der Welt zu entwickeln. Eine der fortgeschrittensten Möglichkeiten zur Gewinnung von Fusionsenergie ist der Tokamak, eine toroidale Kammer, in der das Hochtemperaturplasma durch einen Ring aus torroidal symmetrischen Magnetfeldspulen in Kombination mit einem starken Strom, der im Plasma fließt, eingeschlossen wird. Der Leistungsfluss über die Randschicht eines magnetisch eingeschlossenen Plasmas im stationären Zustand ist die Summe der extern induzierten Heizung und der Energie der Fusionsreaktionen im Kern des Plasmas abzüglich der abgestrahlten Leistung und der Neutronen. Diese Leistung verlässt den Bereich der geschlossenen Feldlinien, indem sie die Separatrix überquert und in den Bereich der offenen Feldlinien, die so genannte Abschälschicht (*engl.* SOL), eintritt. Die Leistungs- und Temperaturabfalllänge ($\lambda_{q_{\|\mathrm{e}}}$, λ_{T_e}) in der nahen Abschälschicht charakterisieren diesen entweichenden Wärmefluss, da sie das Verhältnis zwischen dem Transport parallel zu den Magnetfeldlinien hinab zum Divertor aufgrund der Spitzer-Härm-Elektronenleitung und des senkrechten Transports radial nach außen unter Beteiligung anomaler thermischer Transportprozesse widerspiegeln. Um Erkenntnisse über das Verhalten dieser Größen zu gewinnen, wurde im ASDEX Upgrade (AUG) Tokamak eine thermische Heliumstrahldiagnostik (*engl.* THB) mit hoher räumlicher und zeitlicher Auflösung implementiert. In dieser Arbeit wird eine Datenbank mit Regimen mit hohem (*engl.* H-Mode) und niedrigem Einschluss (*engl.* L-Mode) aufgebaut, um die Temperatur- und Dichteprofile der Elektronen am Plasmarand zu analysieren. Das Ziel dieser Arbeit ist es, die Struktur des Elektronentemperaturprofils zu analysieren, die mit der THB-Diagnostik gemessenen Temperaturabfalllängen zu untersuchen und sie mit der bereits etablierten Thomson-Streuungsdiagnostik (*engl.* TS) am AUG zu vergleichen. Für die komplette H-Mode-Datenbank ist eine Übereinstimmung zwischen dem Punkt der höchsten positiven Krümmung in den THB-Temperaturprofilen und der Position der Separatrix, die vom magnetischen Rekonstruktionscode IDE vorhergesagt wird. Diese experimentellen Befunde werden durch die Ergebnisse einer 1,5 D-Modellierung der Wärmebilanzgleichung von geschlossenen zu offenen Feldlinien mit einer vollständigen senkrechten Beschreibung und einem annahmebeschränkten parallelen Sinkterm unterstützt. Bei den Temperaturabfalllängen ist zu erkennen, dass die mit den THB-Daten erhaltenen Werte um die Separatrix herum nicht konstant sind. Ferner folgen sie den Abhängigkeiten, welche durch die Goldston-Skalierung vorhergesagt werden: eine inverse Relation mit dem Plasmastrom und keine Abhängigkeit von der Heizleistung. Beim Vergleich der THB- mit den TS-Daten ergeben sich ähnliche Abfalllängen, wenn sich die gewählten radialen Bereiche zur Auswertung der beiden unterschiedlichen Diagnostiken überschneiden.

A la memoria de mi abuela Santas

Contents

1.Introduction

Every small advance in how we make use of energy is linked to a step in our evolution as a species [Pî12]. We grow in the light of a technology, we expand, we stagnate, we block, until a new technology is discovered, suitable for our new circumstances and needs. Humanity in the 21^{st} century, in a scenario of global warming and increasing population [UN19], has reached this blockage. In order to overcome this situation, a transformation of the global energy system must be carried out.

At the moment, the world's primary energy supply comes mainly from burning different fossil fuels. The use of these technologies is always accompanied by an excessive release of the greenhouse gas CO_2 into the atmosphere, which has devastating consequences for the environment. Since the adoption of the *Paris Agreement* in 2015 [NAT15], more and more countries are moving towards alternative technologies to reduce their carbon footprint. Among the different CO_2-neutral options, we can find renewable energies and nuclear fission power plants. Renewable energies have yet a low share but are the fastest growing and cheapest form of energy [Sen08]. Conversely, the share of nuclear and hydro-power plants remains constant. In the case of fission nuclear power plants, this is due to social acceptance and the unresolved problem of radioactive nuclear waste. In hydroelectric power plants this situation is due to the social and environmental impact of the sites.

Even though a formidable job is being done in the field of the renewable energies, just their contribution to the electricity grid may not be sufficient in the future. Another possible and complementary solution to this blockage could be to replicate here our sun, responsible for almost any form of energy on our planet. It is theoretically known that the power reaching the earth's crust in one and a half hours is greater than the world's energy consumption from all sources combined in one year. This can help us to imagine how powerful is the process that makes the sun radiate [Tsa20].

This source of energy is nuclear fusion, a nuclear reaction by which atomic nuclei, if they overcome the Coulomb barrier, fuse together releasing energy from the difference in mass between the reactants and products. On the sun, due to the strong gravity and quantum tunneling, hydrogen atoms fuse already at 15 million °C. On earth, however, because of the weaker gravitational forces, the gas composed by the hydrogen atoms need to be heated to temperatures as high as 150 million °C. This is how they form a quasineutral electrically conductive medium with collective behaviour, known as plasma, the fourth state of matter. On earth, a *tokamak*, which is in essence a toroidal chamber with powerful magnetic fields used for the confinement of the plasma, is one of the most advanced options on the path to achieving fusion power.

This work will be performed with data from ASDEX Upgrade (Axially Symmetric Divertor EXperiment), a midsize tokamak located in Garching [Isa10] designed for power exhaust research, a key aspect for the correct design of future fusion power plants. One of the most important constraints in the design of fusion technologies is predicting the maximum heat flux which originates in the core plasma and transfers to the divertor plates. The divertor plates are the only region where the plasma is supposed to touch the walls of the tokamak. In this way, these plates are used to exhaust impurity particles and to dissipate heat. This resulting power load onto the divertor targets crucially depends on the plasma edge heat and particle transport.

In this work, the main focus will be on the plasma edge region, formed specifically only by the first open magnetic flux surfaces, the so-called near scrape-off layer (near SOL). There, an exponentially radially decaying heat flux profile is assumed. Of particular importance in the near SOL are the electron temperature (T_e) and electron density (n_e) profiles and their respective decay lengths (λ_{T_e} and λ_{n_e}), as their investigation might lead to a better predictability of the heat exhaust in future fusion devices.

In this thesis, the structure of the electron temperature and density profiles around the separatrix measured with the thermal helium beam diagnostic (THB) is studied. The thermal helium beam diagnostic (THB) is a plasma edge diagnostic installed at the ASDEX Upgrade tokamak (AUG) which provides simultaneous measurements of n_e and T_e with superior spatiotemporal resolution in our region of interest [Gri18].

This thesis is structured as follows: chapter 2 introduces the fundamentals of nuclear fusion, magnetic confinement in tokamaks, followed by a short overview of the near SOL physics and scaling laws. In chapter 3, the diagnostic techniques that are used, namely the thermal helium beam diagnostic (THB) and the Thomson scattering (TS) system are introduced. Moreover, the experimental database collected for the following analysis is presented. In chapter 4, the structure of electron temperature (T_e) and density profiles (n_e) around the separatrix with THB data is investigated. Two approaches for the study of the profile derivatives and their extrema points are presented. From the analysis of the electron temperature structure of attached H- and L-mode discharges in conduction-limited regime and linear regime in section 4.4, a self-consistent connection between the extrema of the electron temperature curvature ($\partial_R^2 T_\mathrm{e}$) and the position of the separatrix (R_sep) is revealed. In order to understand the physics behind these experimental agreements, a simple 1.5 D modelling for the heat balance equation from closed to open field lines is carried out in chapter 5. The solution profiles from the differential equation and their derivatives are compared to the experimental data. A comparison of the simulation profile from the turbulence code GRILLIX and its derivatives with the experimental data is also presented in section 5.3. Finally, in order to calculate the temperature (λ_{T_e}) and density (λ_{n_e}) fall-off lengths with the THB data, three different fits comprising different radial regions (namely the *local* fit, the *1-λ-averaged* fit and the *across-separatrix* fit) are introduced in chapter 6. The dependencies of λ_Te with the global (the plasma current I_p, safety factor q_{95} and heating power P_h) and local parameters are also studied in this chapter. A comparison between the temperature fall-off lengths measured with the Thomson scattering system and the thermal helium beam diagnostic is shown in the section section 6.3.

2. Theoretical Background

2.1. Nuclear Fusion Basics

Whereas an atomic transition might emit a photon in the visible spectrum of a few electron volts, the energy of the products released from a nuclear reaction can lie in the MeV range. This is due to the nuclear force, which is powerfully attractive between nucleons at distances of about 1 fm, but it rapidly decreases to insignificance at distances beyond $\approx 2.5\,\text{fm}$ [Coo89]. There are two possible ways in which a yield of energy could be achieved with nuclear reactions: either by the breakup of heavier nuclei (fission) or by the combination of lighter nuclei into nuclei which are more tightly bound (fusion). If the combined nuclear mass is less than that of Fe, element with the highest binding energy per nucleon, then the nuclear particles will be more tightly bound than they were in the lighter nuclei, and that decrease in mass is released in form of energy according to the Einstein relationship ($E = mc^2$) [Pou17].
In order to come within the nuclear force range, the energy of the center-of-mass system formed by the reactants needs to overcome the Coulomb barrier, which could be derived from the Coulomb potential of the nuclei at its effective radius [Str11]. For example, for an interaction between the hydrogen isotopes deuterium (${}^2_1\text{D}$) and tritium (${}^3_1\,\text{T}$), a potential barrier of $\approx 0.4\,\text{MeV}$ (corresponding to $T \approx 4500\,\text{MK}$) is expected. However, the sun is already fusing light elements with much lower temperatures at its core ($E \approx 1.9\,\text{keV}$ and $T \approx 19\,\text{MK}$). This is because the particles in the high energy tail of the Maxwell distribution composing the plasma of the sun are more likely to tunnel, increasing in this way the probability for the colliding nuclei to penetrate the Coulomb barrier, allowing fusion to take place at lower temperatures.
The best candidate to achieve controlled fusion on earth is the deuterium-tritium (D-T) reaction (Eq. 2.1), since it exhibits the maximum value of the cross-section at the lowest temperatures (around $\approx 15\,\text{keV}$, $T \approx 175\,\text{MK}$) [Str11]:

$$ {}^2_1\text{D} + {}^3_1\,\text{T} \longrightarrow {}^4_2\,\text{He}\ \ (3.52\,\text{MeV}) \quad + \quad \text{n}\ \ (14.06\,\text{MeV}) \tag{2.1} $$

Contrary to fission energy, the major by-product of this reaction is helium: an inert, non-toxic gas that can be easily disposed of. The other product are free neutrons that can escape the magnetic confinement heating the blankets of the plant, where these neutrons are absorbed and their energy is converted into heat. This heat can be converted into usable energy in the traditional way (e.g. using the heat to produce steam that can drive turbines to produce electricity). However the absorption of the neutrons it does not only produces heat but causes the activation of the components of the wall chambers. In this way, some of the the reactor's structural steels can meet the requirements to be classified as low level waste (LLW) and thus need to be disposed as radioactive waste. Nevertheless unlike the case of fission reactors, waste with medium or high activity can never be produced in fusion reactors [San20] and the activation is low enough so that the activated steel materials can be recycled or reused within 100 years [Bai21]. Moreover,

both products are accompanied by an increment in their kinetic energies, whose order is higher than the energy gain obtained with the typical fission reactions.
Another advantage is that both fusion fuels are widely available and nearly inexhaustible. Deuterium can be distilled from all forms of water, while tritium will be produced during the fusion reaction as fusion neutrons interact with a lithium blanket covering the walls of the future fusion power plant. For this purpose, the $^{6}_{3}$Li-reaction is preferred [Kon17]:

$$^{6}_{3}\mathrm{Li} + \mathrm{n} \quad \rightarrow \quad ^{4}_{2}\mathrm{He} + ^{3}_{1}\mathrm{T} \quad (4.78\,\mathrm{MeV}) \tag{2.2}$$

In this reaction, 4.78 MeV are additionally released, so that the total energy liberated per fusion reaction effectively increases to 22.36 MeV as it can be seen in Fig. 2.1. One possibility for the tritium breeding system could be to use a solid pebble bed with lithium ceramics. In this system, tritium is collected from the blankets via pore diffusion and the purge flow containing helium is collected and disposed of via flow convection using a coolant to extract the extra helium heat coming from the breeding reaction [Kon17].

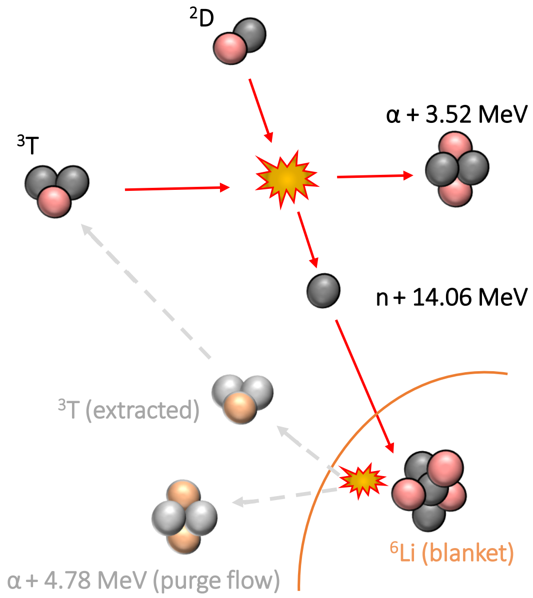

Figure 2.1.: Illustration for the D-T and T-Breeding nuclear reactions starting with D and T (recycled) and ending with a total amount of 22.36 MeV of released energy

Even if at microscopic level the fusion of two light nuclei releases a high energy, few fusion reactions in long times will not produce a large amount of power. In order to produce a large quantity of energy, the involving nuclei must be confined for enough time, in a volume where there is a number high enough of these elements, and have enough kinetic energy.

These conditions can be quantified with the *triple product*, which relates the plasma particle density n, its temperature T and the energy confinement time τ_E, which characterizes the time in which the plasma loses its energy.

In the case of the D-T reaction, this condition is [Cos16]:

$$n \cdot T \cdot \tau_E > 3 \cdot 10^{21}\ \mathrm{m}^{-3}\ \mathrm{keV}\ \mathrm{s} \tag{2.3}$$

From the products of the D-T reaction, only the α-particles remain confined with the other particles in the plasma and can transfer their energy to the other particles by collisions, thus heating in this way the plasma. This plasma is said to be *ignited* when only the α-particle heating is enough to entirely compensate the power losses.

Another important quantity to measure the success of a fusion device is the power amplification *Q-factor*, which is the ratio between the thermonuclear power produced and the heating power supplied. However it is reasonable to not aim for the full ignition to keep a better control of the plasma parameters by external heating.

ITER, the world's largest tokamak being built in Cadarache, is expected to be the first device to produce a considerable energy output, demonstrating the feasibility of fusion energy. ITER is designed to produce a ten times return on invested energy: 500 MW of fusion power from 50 MW of input power ($Q \geq 10$) [Aym02].

2.2. Magnetic Confinement in Tokamaks

In order to achieve a suitable fusion reaction rate in a laboratory, a D-T plasma which fulfils Eq. 2.3 is needed. Due to this requirement, a direct contact with the surrounding walls of the container can not be used to hold back the laboratory plasma. One possibility to enclose this plasma is with magnetic fields in order to control the trajectories of the charged particles within the plasma with the configuration of the magnetic field lines. In order to explain the different properties of laboratory plasmas in magnetic confinement devices, the plasma is treated as a fluid in this chapter. For this description, it will be assumed that the plasma is in local equilibrium and that collisions are frequently enough to balance out deviations from a Maxwell distribution. In this picture, fluid quantities like mass density, charge density and temperature or pressure are used. To describe the plasma dynamics quantitatively, fluid equations are employed. The formulation of these come from the equations of hydrodynamics but also taking into account the magnetic properties and electrical conductivity of the plasma, this is known as *magneto-hydrodynamic* (MHD) equations. The first MHD equations describe the transport of conserved quantities, i.e. they are the continuity equations for the mass density (ρ_{m}), charge density (ρ) and their corresponding mass flow ($\rho_m \boldsymbol{u}$) and net charge flow ($\boldsymbol{j}$):

$$\frac{\mathrm{d}\rho_m}{\mathrm{d}t} + \rho_m \nabla \cdot \boldsymbol{u} = 0 \tag{2.4}$$

$$\frac{\partial \cancel{\rho}}{\cancel{\partial} t} + \nabla \cdot \boldsymbol{j} = 0 \tag{2.5}$$

where the temporal derivative for the charge density is neglected due to the quasinetrality properties of the plasma. The fourth MHD equation expresses the generalized Ohm's law for a plasma. It is the third MHD equation where the fundamental concept behind MHD lies. It comes from the equation of motion and momentum conservation:

$$\rho_{\mathrm{m}} \frac{\mathrm{d}\boldsymbol{u}}{\mathrm{d}t} = \rho\,(\boldsymbol{E} + \boldsymbol{u} \times \boldsymbol{B}) - \nabla P \pm R_{\mathrm{ei}} \tag{2.6}$$

where $\boldsymbol{E}$ and $\boldsymbol{B}$ are the electric and magnetic fields, $\boldsymbol{u}$ the flow velocity, ∇P and R_{ei} the pressure and friction terms respectively.
Because of the quasineutrality of the plasma, the Coulomb term ($\rho\boldsymbol{E}$) can be neglected. Under the equilibrium condition ($\dot{\boldsymbol{u}} = 0$) and neglecting frictional forces, Eq. 2.6 could be rewritten as:

$$\nabla P = \boldsymbol{j}_{\mathrm{d}} \times \boldsymbol{B} \tag{2.7}$$

The fundamental concept behind this third MHD equation is that magnetic fields can induce diamagnetic currents in a plasma, which in turn polarizes the fluid and reciprocally changes the magnetic field itself.
The pressure force (left side of Eq. 2.7) is balanced by the Lorentz force (right side of Eq. 2.7) which generates a diamagnetic current ($\boldsymbol{j}_{\mathrm{d}}$). In this way, a magnetic field line responds, like a guitar string, to displacements in the plasma with a restoring force.

In the following, the main physical properties in terms of *equilibrium, confinement* and *stability* are analyzed for one of the simplest example devices using magnetic confinement, a simple magnetized torus with a plasma major radius (R_0) and a plasma minor radius (a) with only toroidal field lines (B_{t}) as illustrated in Fig. 2.2.

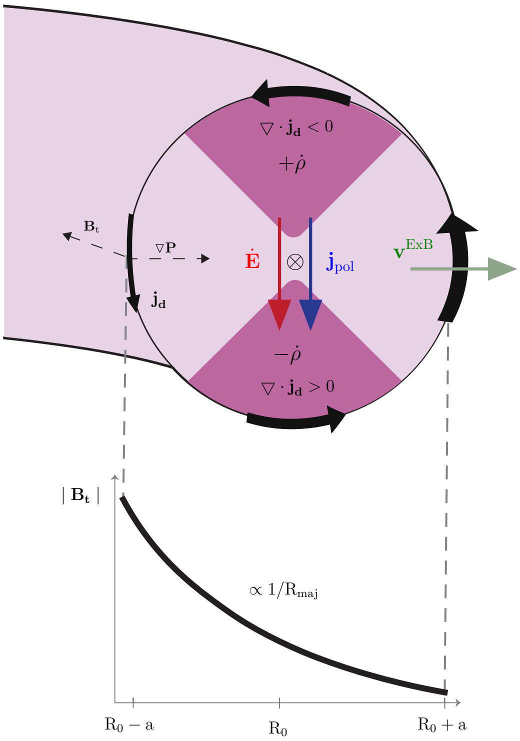

Figure 2.2.: Geometry for the left end cross-section of a simple magnetized torus. The confinement and equilibrium are explained in terms of the diamagnetic current ($\boldsymbol{j}_{\mathrm{d}}$) dependent to ∇P and $|B_{\mathrm{t}}|$; the charge accumulation ($\dot{\rho}$); the temporal electric field ($\dot{\boldsymbol{E}}$); the polarization current ($\boldsymbol{j}_{\mathrm{d}}$) and the ExB-drift ($\boldsymbol{v}^{\mathrm{ExB}}$)

For that purpose, an specific expression for $\boldsymbol{j}_{\mathrm{d}}$ from Eq. 2.7 is needed:

$$\boldsymbol{j}_{\mathrm{d}} = \frac{\boldsymbol{B} \times \nabla P}{B^2} \tag{2.8}$$

In a simple magnetized torus, the pressure (P) is highest on the toroidal axis, so that there is a radial pressure gradient (∇P).

Using the Ampère's Law for this torus, it can be seen that the toroidal field strength ($|\boldsymbol{B}_\mathrm{t}|$) goes inversely proportional to the major radius ($\propto 1/R_\mathrm{maj}$) as depicted in Fig. 2.2. Knowing the directions and proportionalities for ∇P and $|\boldsymbol{B}_\mathrm{t}|$ and using Eq. 2.7, it is now easy to visualize the diamagnetic current, which flows counter clockwise in the poloidal direction and is proportional to the major radius ($j_\mathrm{d} \propto R_\mathrm{maj}$). Due to this proportionality, $\boldsymbol{j}_\mathrm{d}$ is stronger on the low field side (LFS) than on the high field side (HFS). This causes a negative divergence of the diamagnetic current on the top and a positive one on the bottom of the torus. This leads, as indicated in the continuity equation for the charge density Eq. 2.5 ($\nabla \cdot \boldsymbol{j}_\mathrm{d} = -\dot{\rho}$), to the appearance of charges on the upper ($+\dot{\rho}$) and lower ($-\dot{\rho}$) sides of the torus. These charge accumulations induce a time dependant electric field (in red in Fig. 2.2) which in turn induces a polarization current proportional to this electric field ($\boldsymbol{j}_\mathrm{pol} \propto \dot{E}$, in blue in Fig. 2.2). This polarization current works against the escaping diamagnetic current, compensating the charge accumulation. In this way, the total current in the plasma is short-circuited ($\nabla \cdot \boldsymbol{j}_\mathrm{d} + \nabla \cdot \boldsymbol{j}_\mathrm{pol} = 0$) and the *equilibrium* and quasineutrality of the plasma is maintained.

However, the *confinement* is lost as the formation of the time dependant electric field together with the already present magnetic field ($\boldsymbol{B}_\mathrm{t}$) drives a perpendicular to $\boldsymbol{B}_\mathrm{t}$ and radially outwards flow, $\boldsymbol{v}^\mathrm{ExB}$ (in green in Fig. 2.2). Due to the time dependence of $\boldsymbol{E}$, $\boldsymbol{v}^\mathrm{ExB}$ is an accelerated flow, what means that the plasma is lost (displaced out of the device) very quickly.

Although the equilibrium condition for the simple magnetized torus is fulfilled, in order for the plasma to be stable, also an *stability* condition must be accomplished. Thus, it is studied how the plasma in this simple magnetized torus reacts to small periodically deviations from a determined shape (mode), as illustrated in Fig. 2.3.

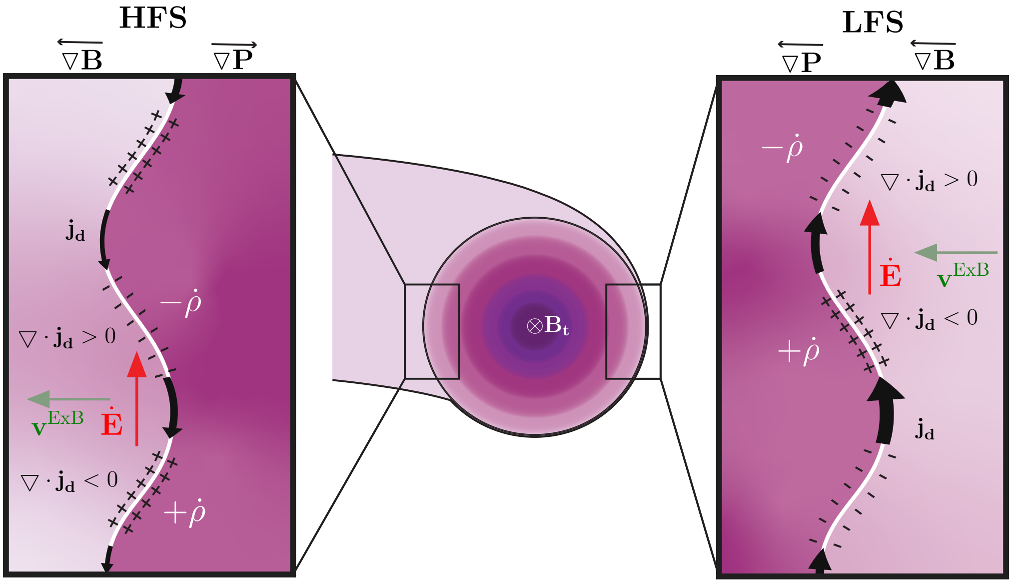

Figure 2.3.: Illustration for the interchange stability in a simple magnetized torus between two layers of different radially outwards decreasing densities (depicted by the color gradient). Both sides HFS and LFS and their respective $\nabla\mathbf{B}$ and $\nabla\mathbf{P}$ configurations are illustrated. Also the divergences at both sides for $\boldsymbol{j}_\mathrm{d}$ and the correspondent induced $\dot{\boldsymbol{E}}$ and driven $\boldsymbol{v}^\mathrm{ExB}$ are included.

Using Eq. 2.7, it can be derived that the diamagnetic current points upwards on the LFS and downwards on the opposite side, following the disturbed magnetic isobars along the boundary between two layer of different mass densities (darker colors indicate higher densities in Fig. 2.3). Due to the dependence of the strength of the diamagnetic current with R, $\boldsymbol{j}_\mathrm{d}$ is either compressed leading to a positive polarized charge along that area in the interface, or expanded leaving negative charges. In the same way as for the confinement study, the charge accumulations induce an electric field which triggers an ExB velocity flow, $\boldsymbol{v}^\mathrm{ExB}$. In this case, the difference between the HFS and the LFS plays an important role: due to the differences in the field strength gradient and the pressure gradient at both sides, there are also different curvatures of the magnetic isobars at both sides. On the HFS at the left side of the Fig. 2.3) where $\triangledown\mathbf{B}$ and $\triangledown\mathbf{P}$ are anti-parallel, it can be seen that $\boldsymbol{v}^\mathrm{ExB}$ has a stabilising effect, what is known as favorable curvature. On the other side, the LFS, $\triangledown\mathbf{B}$ and $\triangledown\mathbf{P}$ are parallel. In this case the ExB velocity flow amplifies the initial perturbation and the plasma is left unstable and the curvature is unfavorable.

It is proved in this way that a simple magnetized torus does not provide a good confinement nor an stable plasma. A solution to fight both, the charge accumulation effects and the instability effects is to add a poloidal component ($\boldsymbol{B}_\mathrm{p}$) in order to have helical field lines. A helical field line will therefore connect the regions of positive (top) and negative charge (bottom) so that the ExB velocity flow is balanced out. Moreover this twisting of the field lines connect the areas of favourable and unfavourable curvature, allowing the stabilising effect of the HFS to overcome the destabilising effect of the LFS. Thus, the plasma is confined and left stable if a poloidal component is added. Instability is only achieved when the amplitude of the deformation of the isobars on the LFS is greater than on the HFS.

As a measure for the twisting of a field line, one takes the rotational transformation (ι), defined as the number of turns that a field line makes in poloidal direction while going around the torus in the toroidal direction [Miy05]:

$$\iota = 2\pi \frac{R}{a} \frac{B_\mathrm{p}}{B_\mathrm{t}} \tag{2.9}$$

However, it is the safety factor (q_s), defined as the number of toroidal revolutions for one poloidal revolution, the parameter preferred to qualify the plasma stability in axisymmetric toroidal geometries [Miy05]:

$$q_\mathrm{s} = \frac{a}{R} \frac{B_\mathrm{t}}{B_\mathrm{p}} \tag{2.10}$$

Due to the variation of the poloidal and toroidal field with the minor radius, q_s is changing from the plasma core to the edge region. In order for the plasma to be magnetohydrodynamically stable, the safety factor should be higher than 2 in the edge region [Wes05], meaning that higher values of q_s would lead to a more stable plasma. However, if q_s is too high, the confinement would be degraded, as a trade off between stability and confinement is required.

A tokamak is one of the most promising approaches using magnetic fields to produce an stable and confined plasma in order to achieve fusion on earth. The magnetic structure of a tokamak is composed by a toroidal (B_t), poloidal (B_p) and also a vertical (B_v) field components, as it can be seen in Fig. 2.4 a). This last component is needed to compensate the hoop stress that suffers the poloidal component in a toroidal configuration. The toroidal magnetic field (B_t) is generated by planar toroidal coils. An externally driven toroidal current in the plasma (I_p) then generates the poloidal contribution to the magnetic field (B_p). The generation of this current in the plasma is based in the transformer principle: by changing the magnetic flux in the transformer core, the first winding, a current is produced in the plasma, the secondary loop. This turns the tokamak in an intrinsically pulsed machine. The current in the plasma, circulates until the increasing current in the coils of the central solenoid reaches the maximum allowed value. At this moment, the plasma current and the current in the central solenoid coils are ramped down and a new cycle can be started.

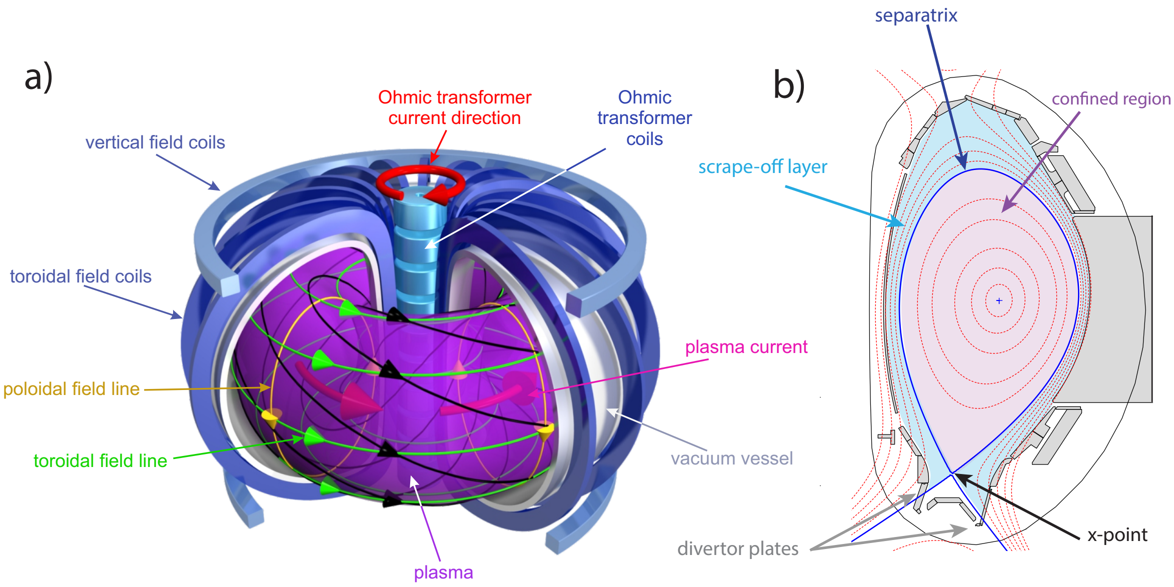

Figure 2.4.: a) Schematic illustration of a tokamak (adapted from Christian Brandt, IPP) showing the different magnetic field components as well as the primary ohmic transformer, toroidal and vertical coils. b) Poloidal cross-section of the plasma inside the tokamak in a lower single null magnetic configuration showing the different regions of the plasma: the confined region in purple, the separatrix in blue and the scrape-off-layer in light blue.

2.2.1. Flux Surfaces in the divertor configuration

In a tokamak, helical magnetic field lines run in nested surfaces (S) of constant magnetic flux. This means that these surfaces are not crossed by the magnetic field. The MHD equilibrium condition, i.e. Eq. 2.7, is fulfilled for these regions, having constant values for the magnetic flux, current density and pressure. In a toroidal geometry, these nested flux surfaces are labeled with the universal flux coordinate, the so-called normalized poloidal flux radius (ρ_pol), which is defined as the normalized poloidal flux:

$$\rho_\mathrm{pol} = \sqrt{\frac{\Psi - \Psi_\mathrm{axis}}{\Psi_\mathrm{sep} - \Psi_\mathrm{axis}}} \tag{2.11}$$

where Ψ is the poloidal flux corresponding to the integral of the toroidal magnetic field component ($\boldsymbol{B}_{\mathrm{t}}$) over the poloidal area (S_{p}):

$$\Psi = \int_{S_{\mathrm{p}}} \boldsymbol{B}_{\mathrm{t}} \cdot \boldsymbol{n} dS \tag{2.12}$$

This flux coordinate (ρ_{pol}) is used to identify the different equilibria regions of the plasma in a divertor configuration in a tokamak. It has the value $\rho_{\mathrm{pol}} = 0$ in the magnetic axis (blue cross in Fig. 2.4 (b) at the plasma center) and it is $\rho_{\mathrm{pol}} = 1$ at the separatrix (blue line in Fig. 2.4 (b)), which is the last closed flux surface. The separatrix separates the closed magnetic field lines (in purple in in Fig. 2.4 (b)) and the open ones which intersect with the vessel components. The x-point is the point of this last closed flux surface where the poloidal magnetic field vanishes(in Fig. 2.4, crossing point of the separatrix). The region of open field lines outside the separatrix, called scrape-off layer (in pink in Fig. 2.4 (b)), is directly connected to the divertor plates (at the bottom in grey in Fig. 2.4 (b)), which are baffle plates where the plasma particles and impurities which are not anymore confined are pumped off and the heat coming from the core is dissipated. The heat load on the divertor plates is a matter of great concern. In the actual mid-sized tokamaks it has a value of around 50 MWm^{-2} [Her02] but in future larger devices, the plasmas scenarios need to be adapted in order to handle the material constraints.

In tokamaks with a divertor, q_{s} from Eq. 2.10 diverges to infinity at the separatrix, so if the lines are not closed, it is more useful to consider the safety factor just inside the separatrix at the flux surface that encloses 95% of the toroidal flux, what is also known as q_{95}.

2.2.2. Divertor Regimes

The divertor is thus used to control the power exhaust and to protect the main plasma from the sputtered particles from the the wall materials, which would contaminate the plasma. There are different divertor configurations to control the heat power loads on to the divertor plates. One possibility is when the power is fully deposited on the baffle plates. This configuration is known as *attached* and is the scenario chosen to work with in this thesis.

Another option could be to partially shield the divertor plates from the main plasma by apertures so that an increase in neutral gas pressure can be achieved there. The increased pressure makes it easier to pump out the helium and to extract energy and momentum from the diverted plasma due to friction with the neutral gas by means of charge exchange recombination processes. This divertor regime, only efficient for low temperature plasmas (in the divertor $< 5eV$) is known as *detachment* or *detached plasma* [Str11].

2.3. Confinement Regimes

The most typical stationary modes that can operate in a tokamak are the low confinement (also known as L-mode) and the high confinement regimes (H-mode).

The *H-mode*, discovered at ASDEX in 1982, is characterised by strong turbulence suppression, originating from a so-called edge transport barrier (ETB) in plasma temperature and density as well as by high energy confinement times, typically enhanced by a factor of 2 [Wag82] compared to corresponding L-mode values. Due to the formation of the ETB, the flow of particles and energy across the flux surfaces is reduced, giving rise to improved confinement properties. This high confinement regime can be reached when the plasma is heated strongly and a threshold heating power ($P_{\text{threshold}}$) level is exceeded. The H-mode is the consequence of a self-organizing process in the plasma, however the stabilising mechanisms, enabling the transition to H-mode have not been completely elucidated. One of the most widely accepted theories states that the suppression of turbulence is the consequence of the formation of a sheared flow layer and an associated edge radial electric field [Cav16].

The local suppression of turbulence leads to a reduction of transport and a steepening of the edge profiles as it can be seen in Fig. 2.5. These steep gradients at the edge lead to specific MHD instabilities in the H-mode, known as *edge localised modes* (ELMs) [Zoh96]. During these events, the plasma pressure profile relaxes periodically towards less steep slopes, until the edge transport barrier recovers and rebuilds itself and the pressure profile steepens again before crashing at the following ELM (depicted in dashed dark green in Fig. 2.5 (c)). As a consequence, large particles and heat bursts escape from the plasma at each ELM, leading to large power fluxes to the plasma facing materials on the vacuum chambers. There are different types of ELMs and in this work the focus relies on type-I ELMs, the most energetic ones. These large ELMs occur at the edge with a frequency between 10-200 Hz, which depends on the heating power. Its initialization can be described by a coupled peeling-ballooning mode as described in [Sny04].

The operational regime dominated by turbulence is the low-confinement regime, or in short *L-mode.* In contrast to the H-mode, the L-mode occurs with a power below the power threshold ($P_{\text{threshold}}$). This confinement regime is not interesting as a future plasma scenario for a future fusion reactor, however the L-mode is the ideal regime to study plasma turbulence [Man18].

Another regime, not studied in this work but which could be a possible candidate for a fusion reactor, is the improved L-mode regime or *I-mode.* The I-mode regime exhibits an edge energy transport barrier but without the accompanying particle transport barrier. This implies, among others benefits, that there are not any ELMs and that the energy confinement is like the one in the H-mode but with a lower degree of accumulation of helium ashes [Man18].

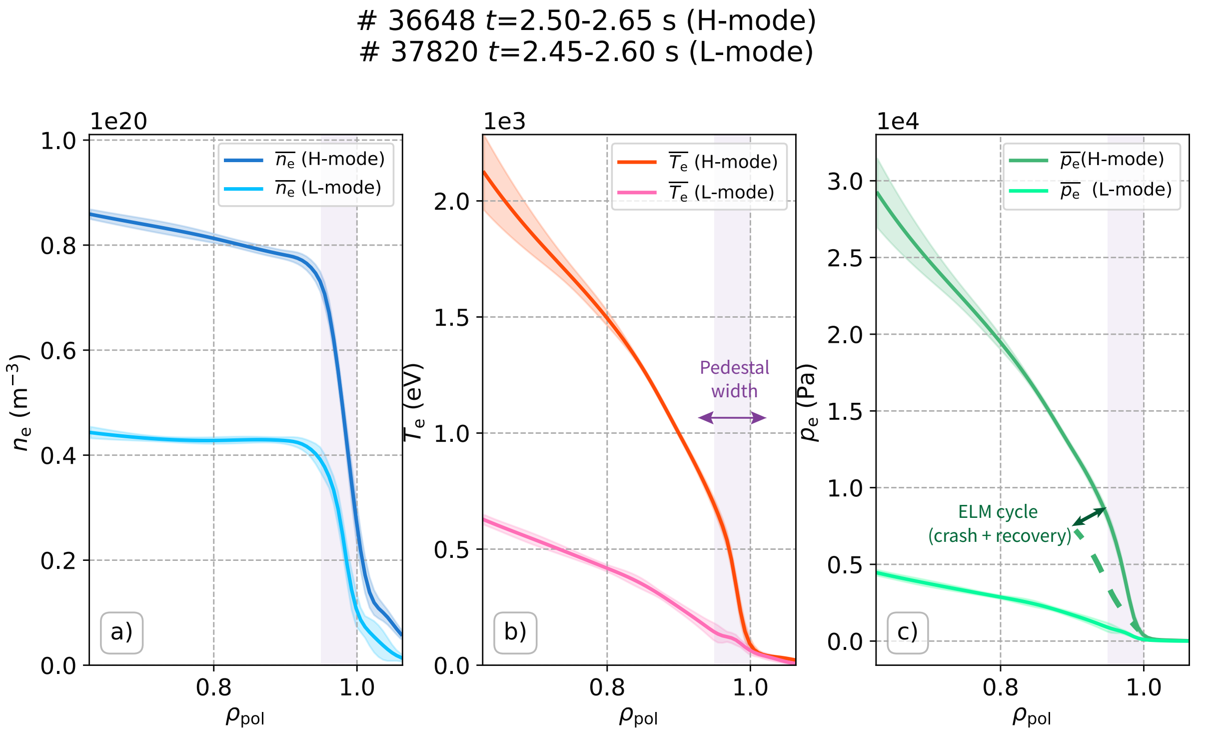

Figure 2.5.: Comparison for the high (darker colors) and low (brighter colors) confinement regimes for the electron density (a), electron temperature (b) and electron pressure (c) profiles along the plasma radius ρ_{pol}. The pedestal region is shaded in light purple and the beginning of the ELM-relaxed pressure profile is drawn in green (dashed).

2.4. Near SOL Fall-Off Lengths

The plasma *edge region*, which extends from the outer region of the confined plasma, through the separatrix and the *scrape-off layer* (SOL), to the inner wall of the vacuum chamber, plays a fundamental role in the dissipation processes of the power coming from the confined region. Of particular importance is the scrape-off-layer, which constitutes the interface region between two very different states: the hot confined fusion plasma in the core of the tokamak and the material surfaces of the fusion machine's solid structure, i.e. the region where $\rho_{\mathrm{pol}} > 1$. The focus of this work relies specifically only on the first open magnetic flux surfaces, the so-called *near scrape-off layer* (near SOL).

In the SOL region, heat flows radially (perpendicular to $\mathbf{B}$) from the confined region to the wall and poloidally (parallel to $\mathbf{B}$) from the upstream region to the divertor plates. Different studies with experimental data for the divertor target heat fluxes, have shown evidence for a purely exponential radial decay of the parallel heat flux ($q_{\parallel e}$) in the scrape-off layer [Eic13]:

$$q_{\parallel e}(r) = q_{\parallel 0}\, \mathrm{e}^{-r/\lambda_{q_{\parallel e}}} \tag{2.13}$$

were r is the radial coordinate relative to the separatrix in the SOL, $q_{\|0}$ the parallel heat flux at the separatrix and $\lambda_{q_{\|e}}$ the SOL power decay length. This width, dependant to the competition between transport processes perpendicular and parallel to the magnetic field, plays a major role in characterizing the area of the divertor plate onto which the radial power from the plasma core is deposited, also known as wetted area (S_w). Because the parallel transport rate is orders of magnitude faster than the perpendicular transport rate, SOL power widths are quite small. However, if these widths are too narrow, the material in the divertor can be damaged. But if they are too wide, the wall components can suffer the effects of the high power loads. A correct trade-off between the different transport mechanisms in the SOL is thus needed to control the power exhaust processes in future fusion devices [Sin17].

2.4.1. Heat and Particle Fluxes in the SOL

The density and temperature profiles in the near SOL are shaped by particle and heat transport. In this section the dominant processes contributing to diffusion/conduction and convection of particles and heat in the near SOL are introduced.

In diffusive processes, heat is transported by particle collisions. *Diffusion* can be described in this way as a random walk of particles following a path of aleatory successive microscopic steps of equal size. The probability for the location of a particle is therefore distributed as a Gaussian around the origin of the path. This distribution is the broader, the more steps are made. In case of a plasma, the collisions between the particles are caused by the Coulomb force, which acts in the plasma only at small distances and angles due to the effective shielding of the electromagnetic fields at distances beyond the Debye length (λ_D), which is the fall-off length of the negative exponential shielding function accompanying the Coulomb term in the Debye-Hückel potential (ϕ) [Str11]:

$$\phi(r) = \frac{q_0}{4\pi\epsilon_0}\frac{1}{r}e^{-\sqrt{2}r/\lambda_D} \tag{2.14}$$

which results from solving the Poisson equation for an external charge (q_0) introduced in the plasma. In Eq. 2.14 ϵ_0 denotes the absolute dielectric permitivity and r is the radial coordinate.

Heat transport by electron *conduction* is a transfer process based on direct contact between bodies, in this case electrons, without exchange of matter but due to the heat flow from a body of higher temperature to a body of lower temperature in contact to the first one, accordingly to the second law of thermodynamics. Thus, electron heat conduction ($\boldsymbol{q}_\mathbf{e}$) in a particular direction is proportional and opposite to the electron temperature gradient (∇T_e), reducing in this way the temperature gradient in that direction. This proportionality, also known as thermal conductivity (κ_e), expresses the physical property to conduct heat, as it is showed in the Fourier's law [Arf84] in Eq. 2.15:

$$\boldsymbol{q}_\mathbf{e} = -\kappa_\mathrm{e}\nabla T_\mathrm{e} \tag{2.15}$$

The thermal conductivity of matter depends on its microscopic structure: in a completely ionized gas it is mainly due to random two-body electron collisions [Spi53]. In this way, it can be seen that the electron conduction is linked with heat diffusion processes in a plasma, being their constants coupled by:

$$\chi_{\mathrm{e}} \equiv \frac{\kappa_{\mathrm{e}}}{n_{\mathrm{e}}} \tag{2.16}$$

where χ_{e} is the thermal diffusivity and n_{e} the electron density. This allows to rewrite Eq. 2.15 as:

$$\mathbf{q}_{\mathrm{e}} = -n_{\mathrm{e}}\chi_{\mathrm{e}}\nabla T_{\mathrm{e}} \tag{2.17}$$

Convection, or more specifically just *advection*, if the diffusion contribution is completely ignored, is the other most important mechanism regarding particle flux (i.e. $\mathbf{\Gamma} = n\mathbf{u}$ with $\mathbf{u}$ as the average velocity of the plasma mass flow in the single fluid picture) in the scrape-off layer. It causes a transfer of heat due to the macroscopic bulk motion of the particles within the plasma. Contrary to the heat diffusion/conduction processes, the net flow of particles responsible for convective mechanisms can create temperature gradients in the plasma.

2.4.2. Power Balance in the SOL

In the following, the expressions for the aforementioned transport mechanisms are derived for the specific geometry of the SOL, illustrated in Fig. 2.6, which can be described either as a 2D region with the first dimension defined as the direction parallel ($\|$) to the field lines and the second dimension as the radial spatial coordinate perpendicular ($\perp$) to the flux surfaces; or as a simplified 1 + 1/2 D geometry with a full perpendicular description and assumption-limited description for the parallel coordinate. It is assumed that in the divertor (downstream location, in red in Fig. 2.6), there can be significant sinks for the charged particles, momentum and energy. For the source location, it will be accepted that all the power coming from the core due to turbulent processes and magneto-hydrodynamic instabilities, enters the SOL in a poloidally localized and broad region around the midplane (upstream point).

In a toroidally confined plasma, inside the separatrix, the connection length (L_{c}) is commonly defined as the length, measured along the magnetic field, to complete a poloidal turn. In the SOL, the connection length associated with a given point is defined as the shortest distance from that point to the divertor material surface measured along the field line through that point. In this thesis, this point is the separatrix position in the midplane. L_{c} plays an important role in determining the temperature profile of the SOL plasma as longer connection lengths allow a significant temperature drop along field lines from hot upstream separatrix temperatures to reasonably low divertor target temperatures. In this way, a large value of connection length (L_{c}) increases the role of cross-field transport and may lead to broader power deposition profile and lower peak heat fluxes [Boz13].

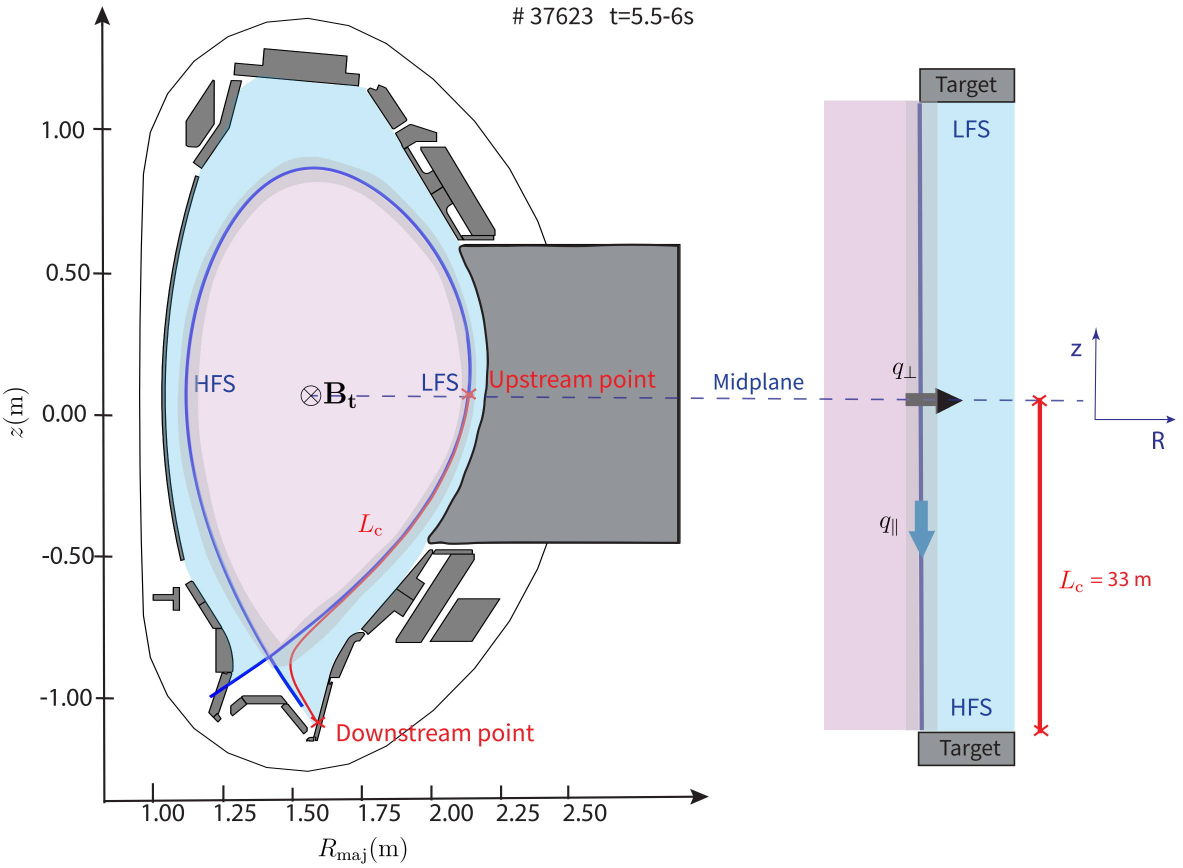

Figure 2.6.: Illustration for the geometry of the scrape-off layer in 2D (left) and in a simplified description (right), including the different heat fluxes with respect to the direction of the magnetic field lines. The separatrix is marked in blue, the confined region in violet and the scrape-off layer in light blue. In red the connection length is indicated for the discharge # 37 623 at ASDEX Upgrade for t = 5.5–6 s from the separatrix position ($R_{\mathrm{maj}} = 2.14\,\mathrm{m}$) in the midplane to the closest divertor target. The region from closed to open field lines, which is modelled in chapter 5 is shadowed in grey.

Assuming the thermal diffusivity χ_{e} and the particle diffusivity D_{e}, from the Fick's law for electron diffusion:

$$\mathbf{\Gamma}_{\mathrm{e}} = -D_{\mathrm{e}} \nabla n_{\mathrm{e}} \tag{2.18}$$

to be constant, an exponentially radially decaying profile for both variables, electron temperature (T_{e}) and electron density (n_{e}) with respective decay lengths ($\lambda_{T_{\mathrm{e}}}$ and $\lambda_{n_{\mathrm{e}}}$) and values at the separatrix (T_0 and n_0), is derived:

$$n_{\mathrm{e}}(r) = n_0\ \mathrm{e}^{-r/\lambda_{n_{\mathrm{e}}}} \tag{2.19}$$

$$T_{\mathrm{e}}(r) = T_0\ \mathrm{e}^{-r/\lambda_{T_{\mathrm{e}}}} \tag{2.20}$$

where r is the radial coordinate relative to the separatrix position in the SOL. These profiles are determined by competition between transport across and along the field lines. In particular, $\lambda_{T_{\mathrm{e}}}$ reflects the ratio of transport parallel and perpendicular to the field lines, being dependant on both global and local plasma parameters. This quantity is key in fusion research as its investigation might lead to better predictability of the heat exhaust in future fusion devices.

High Recycling/Conduction Regime

When the divertor densities increase and the majority of the ionization occurs in the SOL, mainly close to the divertor targets, the plasma is under attached conditions in the *conduction limited* or *high recycling regime*, where diffusive process are dominant and convection is reduced. In these conditions, the particles can move rapidly along the field lines, but only extremely slowly between the surfaces [Sun17a]. This will be the scenario of most of the discharges analysed in this work.

The parallel electron heat flux ($q_{\parallel\mathrm{e}}$) from the Fourier's law from Eq. 2.15 can be written according to [Spi53] as:

$$q_{\parallel\mathrm{e}} = -\kappa_{0\parallel e} T_{\mathrm{e}}^{\frac{5}{2}} \nabla_{\parallel} T_{\mathrm{e}} \tag{2.21}$$

where $\kappa_{0\parallel\mathrm{e}}$ denotes the Spitzer-Härm electron heat conduction coefficient and T_{e} the electron temperature profile in radial direction in the SOL. The expression for the parallel gradient can be simplified using the relation $L_{\mathrm{c}} = \pi R_{\mathrm{maj}} q_{95}$ to calculate the connection length to

$$q_{\parallel\mathrm{e}} = -\kappa_{0\parallel\mathrm{e}} T_{\mathrm{e}}^{\frac{5}{2}} \frac{T_{\mathrm{e,u}}}{\pi q_{95} R_{\mathrm{major}}} \tag{2.22}$$

where $T_{\mathrm{e,u}}$ indicates the electron temperature in the upstream point (see Fig. 2.6), q_{95} is the safety factor at 95% flux inside the separatrix (see Eq. 2.10) and R_{major} is the major radius coordinate.
In case of the cross-field heat flux, the Fourier's law can be written as

$$q_{\perp\mathrm{e}} = -\kappa_{\perp} \nabla_{\perp} T_{\mathrm{e}} = -n_{\mathrm{e,u}} \chi_{\perp} \frac{T_{\mathrm{e,u}}}{\lambda_{T_{\mathrm{e}}}} \tag{2.23}$$

where the perpendicular conductivity ($\kappa_{\perp}$) has been rewritten using Eq. 2.16 and the perpendicular gradient has been expressed in terms of the temperature fall-off length ($\lambda_{T_{\mathrm{e}}}$).

A simple model known as the "*two-point model*" is used to connect the up and downstream (indicated with the indices u and t respectively) temperatures in the SOL when conduction processes are dominant [Pit97]. Integrating Eq. 2.21 leads to the following relation between the electron upstream temperature ($T_{\mathrm{e,u}}$), the upstream parallel power density ($q_{\parallel\mathrm{e,u}}$) and the connection length:

$$T_{\mathrm{e,u}} \approx \left(\frac{7 q_{\parallel\mathrm{e,u}} L_{\mathrm{c}}}{2\kappa_0} \right)^{2/7} \tag{2.24}$$

In this regime there is a simple relationship between the power (i.e fall-off length for power crossing the SOL, defined as the power coming from the confined region taking into account the radiation losses: $P_{\text{SOL}} = q_{||}A_{||} = q_{\perp}A_{\perp} = P_{\text{tot}} - P_{\text{rad}}$) and temperature decay lengths, that is:

$$\lambda_{T_{\text{e,u}}} = \frac{7}{2}\lambda_{q_{||\text{e}}} \tag{2.25}$$

By manipulating Eq. 2.23 to Eq. 2.25, the following proportionality for the parallel conducted power fall-off length $\lambda_{q_{||e}}$ can be derived [Pit97]:

$$\lambda_{q_{||\text{e}}} \propto \frac{L_{\text{c}}\; n_{\text{e,u}}\chi_{\perp}T_{\text{e,u}}}{q_{||\text{e,u}}} \tag{2.26}$$

Eq. 2.26 depends on the relation between the upstream temperature ($T_{\text{e,u}}$) to the parallel power density ($q_{||\text{e,u}}$), which is different depending on the transport regimes. In case of a high-recycling regime, the gradients in temperature are strong, what leads to the following dependencies for the target parameters:

$$T_{\text{t}} \propto \frac{1}{n_{\text{u}}^2} \tag{2.27}$$

$$n_{\text{t}} \propto n_{\text{u}}^3 \tag{2.28}$$

This shows how the temperature at the target could be decreased by the amplification of the particle flux.

2.4.3. Linear/Sheath Limited Regime

When the plasma density is very low and the difference in temperature in the up and downstream points is low, the SOL is said to be in a *linear regime.* This regime is also called the *sheath-limited regime*, as it is the transfer of heat due to the electrostatic sheath and a net particle flow what limits the heat losses, rather than the parallel thermal conduction[Pit97]. This results in linear relations between the temperatures and densities in the source and sink locations:

$$n_{\text{t}} \cong n_{\text{u}}/2 \tag{2.29}$$

$$T_{\text{t}} \cong T_{\text{u}} \tag{2.30}$$

2.5. Power Exhaust and Scaling Laws

In order to predict the confinement empirical methods are used. These are based on large number of data from many tokamak devices and can be then extrapolated to larger tokamaks (e.g. ITER). In recent years multiple attempts have been made in order to scale $\lambda_{q_{\|e}}$. For JET and ASDEX Upgrade, an empirical parametric scaling has been derived in attached divertor conditions, for $\lambda_{q_{\|e}}$[Eic11a]:

$$\lambda_{q_{\|e,u}} = (0.73 \pm 0.38) B_{\mathrm{t}}^{-0.78\pm0.25} q_{95}^{1.20\pm0.27} P_{\mathrm{h}}^{0.1\pm0.11} R_{\mathrm{maj}}^{0.02\pm0.2} \tag{2.31}$$

With $\lambda_{q_{\|e}}$ in mm, the toroidal magnetic field (B_{t}), in Tesla, the heating power (P_{h}) in MW, and major radius (R_{maj}) of the plasma in metres.

3. Experimental Setup and Database

3.1. The ASDEX Upgrade Tokamak

ASDEX Upgrade (AUG) is a midsize tokamak located in Garching since 1991 [Isa10] in charge of developing essential knowledge for the ITER test reactor, which is to realize an energy-producing plasma for the first time. It uses pure deuterium or hydrogen as working gas, so D-T fusion reactions (described in chapter 2) are mostly neglected. The most relevant technical parameters of AUG are listed below in the following table [Mey19]:

Table 3.1.: Technical data for the ASDEX Upgrade tokamak

Parameter	**Value**
Major plasma radius (R_0)	1.65 m
Minor plasma radius (a)	0.5 m
Toroidal field (B_t)	3.9 T
Plasma current (I_p)	1.2 MA
Pulse length	10 s
Plasma mixture	D, H
Plasma heating	27 MW

Large flywheel generators provide the electrical energy for supplying the magnetic field coils and the plasma heaters of ASDEX Upgrade. The plasma is examined with about 40 diagnostics, which could be divided into passive and active methods. The passive techniques measure radiation and particles ejected by the plasma. In contrast, the active methods measure the plasma reaction to external impact or injection of either a particle beam (like active spectroscopy through the injection of high energetic atoms), a material probe (e.g. Langmuir probes to measure particle fluxes) or electromagnetic waves [Hut02]. Using these diagnostics, up to 4 gigabytes of raw data are recorded per discharge, which are identified by shot numbers [Isa10]. In the following the plasma edge diagnostics used for this work, an active spectroscopy method, i.e. the thermal helium beam (THB), and active radiation method, i.e. the edge Thomson scattering system (TS), are introduced.

3.1.1. Thermal Helium Beam Diagnostic (THB)

The thermal helium beam diagnostic (THB) has been implemented at ASDEX Upgrade in 2018, offering a temporal resolution of 900 kHz with a spatial resolution of up to 3 mm at 32 lines of sight (LOS). The LOS cover a radial region of 8.5 cm from the very edge of the confined region to the scrape-off layer. It is used to measure T_e and n_e profiles at the low field side of AUG ($R_{maj} = 2.19$ m and $z = -0.16$ m) with respect to the midplane [Gri18].

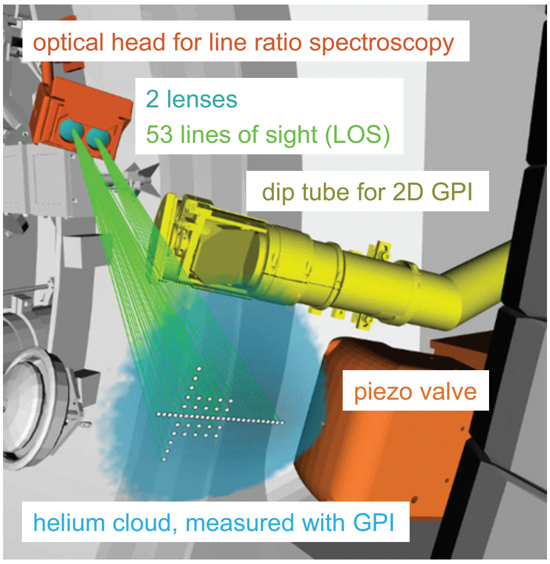

Figure 3.1.: From front to background: the helium cloud is illustrated in blue, the piezoelectric valve is indicated in orange, the optical head for the 2D imaging of the gas cloud in yellow, 53 (27 radial + 26 poloidal) lines of sight (LOS) in green and the optical head for the line ratio spectroscopy with the two lenses in orange. [Gri18]

The emmitted light coming from the collisions between the electrons and the locally injected helium via the piezo valve, is observed in 27 radial lines, which are collected by the optical head (in orange in Fig. 3.1). The collected light is guided through optical fibers to a polychromator system that measures the intensity of the 587 nm, 667 m, 706 nm, and 728 nm helium lines simultaneously for 32 channels with filter-photomultiplier arrays. This diagnostic is mainly used for the calculation of equilibrium profiles, but its fast and spatially highly resolved electron temperature and density profile measurements allows to additionally measure fast and turbulent phenomena [Gri20].

Ratios between two singlet lines are used to calculate the electron density, while electron temperature profiles are obtained from spin-mixed ratios.

These ratios are then used and fitted to obtain the density and temperature profiles from a new collisional radiative model (CRM): electrons excite the He atoms and from He line emissions electron properties can be backwards derived. In this CRM, dynamic state populations are used for the excited and ground states. Re-absorption effects within the helium cloud have also been included in this new model [Wen21].

3.1.2. Thomson Scattering Diagnostic (TS)

This diagnostic is based on the elastic scattering between an electron and a photon, where the photon is re-emitted with the same frequency but in a different direction. In a plasma with many electrons, the Doppler broadening of the Gaussian-shaped scattering power allows electron temperature reconstruction while the electron density can be deduced from the intensity of the scattered light. At AUG, the light of 6 powerful monochromatic Nd:YAG laser (vertically launched) is scattered by the free electrons in the plasma for the edge region. They each have a wavelength of 1064 nm, a pulse energy lower than 1 J, a repetition rate of 20 Hz and a pulse duration of 1 ns. The lasers, separated by a radial distance of 2.7 mm, travel through the volume vertically. For the measurement position, the intersection between the active laser and the middle of the detector's field of view is taken. There are 11 scattering volumes in total depicted in fig. 3.2, which results in 11 data points each time a measurement is carried out. Edge TS system also allows simultaneous measurements for the density and temperature profiles with a good spatial resolution (3 mm). However, this diagnostic offers a slow temporal resolution (120 Hz), and quite noisy data coming only from a tiny fraction ($1/10^{13}$) of scattered light, requiring optimized detectors to handle the low signal levels [Kur11].

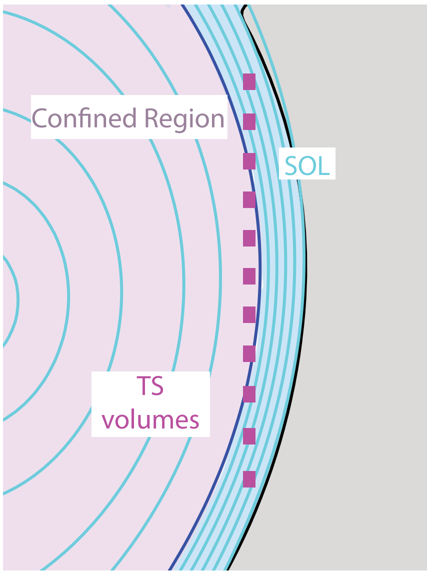

Figure 3.2.: Poloidal cross section of AUG showing the edge Thomson Scattering System. The measurement volumes are located vertically in the poloidal plane as depicted in this illustration by the dashed purple line. The confined region (in violet) as well as the scrape-off layer (in blue) are also depicted.

3.2. Plasma Scenarios

For this work, a database of AUG discharges in an attached divertor configuration (mainly in the high recycling regime, but also linear regime) of 33 discharges, 21 type-I ELMy H-modes and 12 L-modes is built. Data are accumulated over steady-state intervals of a maximum duration of 700 ms.

For the H-modes, the data in the studied time windows are synchronized to the onset of each type-I ELM using the shunt divertor current.

In the following table 3.2, the key plasma parameters within the database are summarised. These are the plasma current, the safety factor, the toroidal field, and total heating power. While I_p and P_h show a good variation within the built database, B_t is mostly comprised around 2.5 T for the majority of discharges for both H- and L-modes.

Table 3.2.: Range and median of the key parameters in the database of analyzed discharges

	H-mode discharges		**L-mode discharges**	
	Range	Median	Range	Median
Plasma current (I_p) in MA	(0.6–1.2)	0.8	(0.7–1.2)	0.8
Toroidal field (B_t) in T	(1.9–2.6)	2.5	(1.5–2.5)	2.5
Safety factor (q_{95})	(3.6–7.4)	4.7	(3.6–5.9)	4.3
Plasma heating (P_h) in MW	(1.5–16)	5.6	(0.0–2.5)	0.5

In order to include a discharge in the database, it is proved before that the time window studied for this discharge remains in steady-state conditions, i.e. the main definition parameters within the analysed time interval are constant.

These are the plasma current I_p, the total stored energy in the plasma W_MHD, the heating power (usually neutral beam injection and electron cyclotron resonance heating power), the inline integrated electron density n_e and the core electron temperature T_e. Also, the fueling must be uniform, with deuterium values much higher than the diagnostic He inlet. In the case of H-modes, the shunt current of the inner divertor I_div must show a constant frequency of current peaks in order to separate in an optimised way the ELM phases from the inter-ELM phases. The reason for this is because the time evolution of the shunt divertor current mimics the evolution of the divertor heat flux: an initial oscillatory phase, during which current reversals can occur, followed by a bulk phase, whose shape resembles the peak heat flux profiles measured by IR thermography are typical signatures for ELM phases [Kno19]. The major outer radius R_aus of the separatrix position at the mid-plane, the height of the current centroid z_squad and the measured emission at 667.8 nm of injected helium must also be constant.

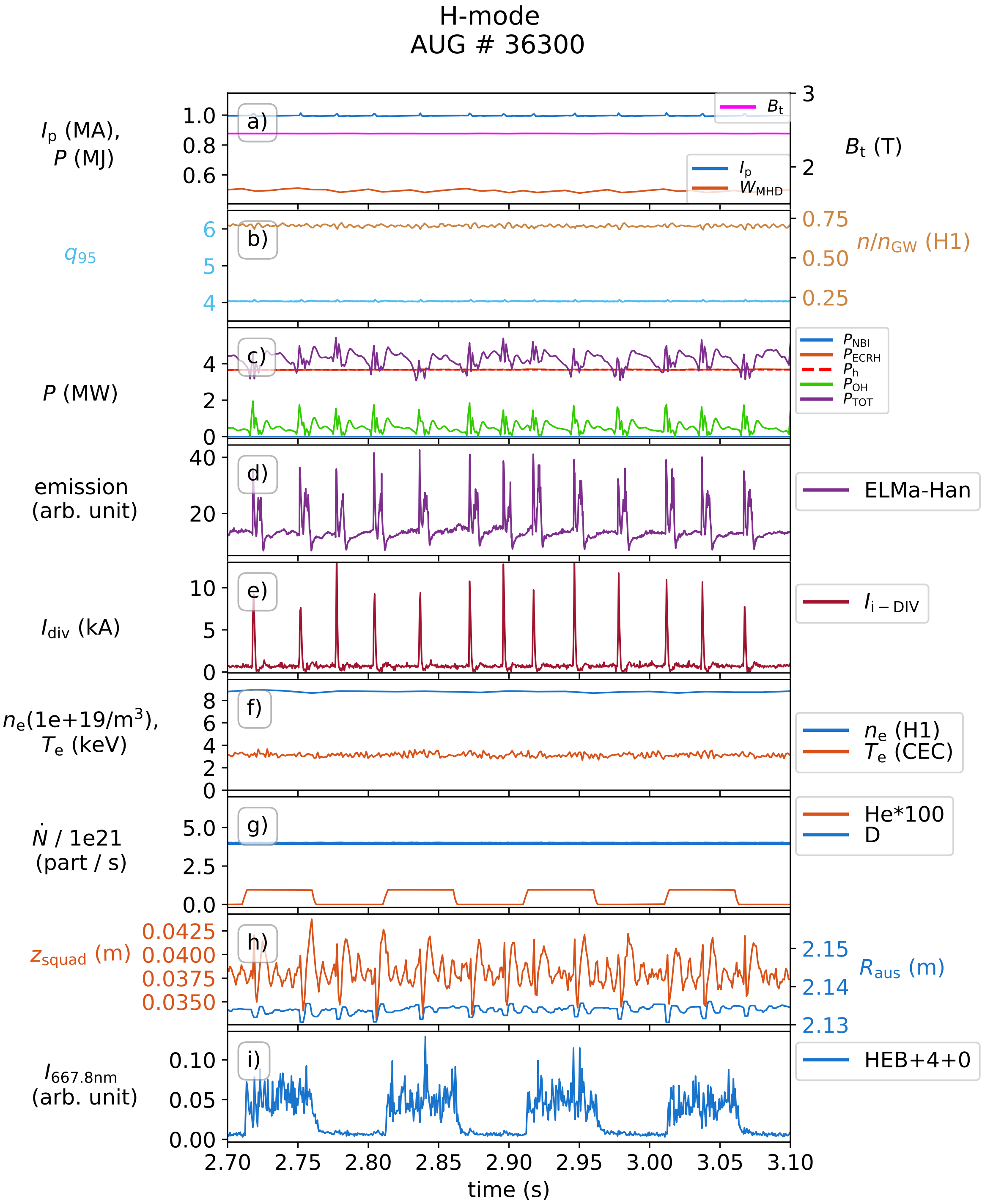

Figure 3.3.: Experimental time traces of AUG discharge # 36 300 for the time interval $t = 2.7$–3.1 s, presenting steady-state conditions (constant phases) in the plasma current I_p, the stored energy W_MHD and toroidal field B_t in subplot (a), the safety factor q_{95} and the Greenwald fraction n/n_GW in subplot (b), the heating power P_h (for this case only electron cyclotron emission radiation heating power P_ECRH), the ohmic power P_OH and the total power P_TOT in subplot (c), D-α emission signal in (d), the divertor current I_div in subplot (e), the inline integrated electron density n_e and the core electron temperature T_e in (f), the plasma fueling in (g), the outer major radius R_aus and the height of the current centroid z_squad in (h), and the He emission signal for the fourth radial LOS in (i).

4. Experimental Analysis of Electron Temperature and Density Profiles

A major part of this thesis is the analysis of near SOL electron temperature and density profiles and its corresponding fall-off lengths measured with the Thermal Helium Beam diagnostic under steady-state heat flux conditions, observed in type I-ELMy H-modes and L-modes. In order to do this, it is necessary to establish the limits for the near SOL, starting at the magnetic separatrix. In this way, determining the position of the separatrix (R_{sep}) within the profiles given by the collisional radiative model evaluation for the THB data is a crucial point in this work.

Although there is a reasonable understanding of how heat is confined in the core of a tokamak, or of how the heat from particles or waves is transferred to the tokamak plasma, a validated understanding of how heat escapes through the separatrix across the scrape-off layer and it is deposited in the plasma-facing components, like the walls or the divertor targets, is still lacking [Gol11].

This escaping heat flux can be characterised by the power decay width ($\lambda_{q_{\|e}}$) in the near scrape-off layer. Due to the toroidal symmetry in a tokamak, this quantity corresponds to the surface area of the divertor target plates onto which the heat flux, transported along the open field lines, is distributed.

Different approaches have been attempted to explain the behaviour of this quantity, including a heuristic, drift-based model for the behaviour of the particle scrape-off layer width outside the separatrix (Λ) [Gol11]. This SOL width is governed by a drift-based cross-field particle transport across the separatrix, which should be of the order of the ion poloidal gyro-radius:

$$\rho_{\mathrm{p}}^{\mathrm{i}} = \frac{mv}{|q|B_{\mathrm{p}}} \tag{4.1}$$

where m is the particle mass, v the particle velocity, q the charge and B_{p} the poloidal magnetic field.

Regarding the heat transport, the cross-field heat flux is assumed to be anomalous electron heat diffusion and is adequate to fill the SOL particle width (Λ) with heat from the main plasma, so that $\Lambda \sim \lambda_{q_{\|e}}$. One of the most remarkable implications of this heuristic model is the strong inverse dependence of the SOL power width on the plasma current while there are relatively weak dependencies on other variables.

This model has been compared with experimental data from infrared thermography systems in two different tokamaks, JET and ASDEX Upgrade, for the inter ELM periods of H-mode discharges [Eic11b]. In these studies, the SOL power decay length is determined by analysing the heat flux profiles measured on the outer divertor target. As near SOL power flows towards the outer divertor targets, $\lambda_{q_{\|e}}$ is broadened by the effective magnetic flux expansion, parameterised as f_x. Moreover, the heat flux in the divertor region is also assumed to be broadened by perpendicular diffusion, included by convoluting the near SOL heat flux profiles with a Gaussian representing the power spreading factor (S):

$$q(s) = \frac{q_0}{2} \exp\left[\left(\frac{S}{2f_x\lambda_{q_{\parallel e}}}\right)^2 - \frac{s-s_0}{f_x\lambda_{q_{\parallel e}}}\right] \operatorname{erfc}\left(\frac{s-s_0}{S} - \frac{S}{2f_x\lambda_{q_{\parallel e}}}\right) + q_{\mathrm{BG}} \tag{4.2}$$

In 4.2 s_0 is the strike line position on the targets, S the width of the Gaussian, q_0 the peak heat flux and q_{BG} the background heat flux. In this way, the convolved form disentangles the SOL power width and the perpendicular diffusion taking place in the divertor targets.

A multi-machine empirical scaling has also been carried out [Eic13], showing strong dependencies with q_{95} and B_{t}, and a minor dependency with the heating power P_{h}. A satisfactory agreement between the power decay length provided by the heuristic model and the experimental data is also found. If the empirical scaling is extrapolated to ITER, it gives $\lambda_{q_{\parallel e}}^{\mathrm{ITER}} \sim 1$ mm under attached conditions, significantly lower than the projected and more desirable width from previous studies [Loa07].

As the scaling for the near SOL power widths was derived indirectly from infrared measurements at the divertor targets, therefore it would be interesting to perform direct upstream measurements to test the scaling. In this way, in [Sun15] a study of the near SOL decay lengths at ASDEX Upgrade with the Thomson scattering systems is carried out. Assuming a purely upstream exponentially radially decaying heat flux profile at the outer midplane separatrix region from [Sta10], a log-linear fit in the near SOL for an H-mode dataset is done in [Sun15] and both L-mode and H-mode databases in [Sun17a]. Both studies show that the obtained power decay lengths have the same parametric dependencies as the scaling inferred from the IR measurements. In [Hos19], the fall-off lengths in the near SOL inside/outside the separatrix measured with TS are calculated, stating that these decay lengths are constant and also have the same value within the near SOL and also inside the separatrix as the fall-off length evaluation is insensitive to the exact fit interval around the separatrix.

Thus, it can be seen that in order to develop a validated understanding of the power exhaust physics in the SOL, it is indispensable to carry out more experimental studies with edge diagnostics. The work of this thesis is motivated within this working frame. In particular, the main focus lies in the analysis of the structure of the experimental electron temperature and density profiles in the near scrape-off layer directly measured with the thermal helium beam, a newly implemented edge diagnostic with superior spatiotemporal resolution.

4.1. Temperature and Density Profiles from the Thermal Helium Beam Evaluation

For the evaluation of the ASDEX Upgrade thermal helium beam data, a new collisional radiative model [Wen21] has been implemented. Before this evaluation is carried out on the THB calibrated data, the raw data measured with the THB diagnostic are stored in the AUG shotfile system (level zero) under a HEB shotfile. A calibration shotfile HEC (level one) is then generated from the HEB shotfile. HEC contains the calibrated data as well as the position information of the LOS used. The final level two is an IDA (i.e integrated data analysis) shotfile, stored in the experimental campaign folder AUGE, containing the evaluated n_e and T_e profiles via forward modelling with a collisional radiative model. In this model, the dynamic state mixing and the re-absorption effects are included. A base for the populations of three metastables is sufficient to model the behaviour of the full system with enough precision. Ratios between two singlet helium lines are used to calculate the electron density, while electron temperature profiles are obtained from singlet-triplet ratios [Wen21, Gri18].

In an AUGE:IDA shotfile, there is not only thermal helium data but combined data from three heterogeneous diagnostics, namely deuterium cyanide laser interferometry (DCN), electron cyclotron emission (ECE), and Thomson scattering spectroscopy (TS). The combined analysis relies on the concept of integrated data analysis (IDA) within the framework of Bayesian probability theory, where improved results for the n_e and T_e profiles are obtained from the combined diagnostics with modelling information [Fis10].

The integration of the combined diagnostics relies on the magnetic equilibrium used to define a common coordinate system to which all spatially separated diagnostics have to be mapped. In this way, the THB data, integrated in the IDA framework, is parameterized in a grid over the poloidal coordinate (ρ_pol). This coordinate is then mapped via a magnetic equilibrium reconstruction code on the helium cloud, on particular on the lines of sight (LOS) from the experimental setup. It is important to mention that within this analysis there is no special treatment for the separatrix position (R_sep).

For all the discharges presented in this thesis, the modular IDE (i.e integrated data analysis equilibrium) package is used for the magnetic equilibrium reconstruction, as its modular code environment provides a flexible framework that can be easily extended with additional heterogeneous measurements, as in the case for the evaluation of the AUGE:IDA shotfiles [Fis16].

A typical density and temperature profile from an AUGE:IDA shotfile including the CRM evaluation can be seen in figures fig. 4.2 and fig. 4.1 respectively. The shaded regions in orange and green correspond to the domain where the signal to noise ratio of the THB data becomes lower as the THB uncertainties increase and the other diagnostic systems weigh more in the analysis. The region where all other diagnostics at the edge are switched off, so that the profile there is only is determined by the THB, corresponds to the not shaded region in fig. 4.2 and fig. 4.1 and it is around 3 cm broad at the plasma edge. The confident interval for the THB data can be checked with the software *IDAView 2.1*, which allows visualizing the absolute intensities for the He lines and their corresponding fits.

Different equilibria positions ($\rho_{\text{pol}} = 0.99$ with orange bar, 1 with blue, 1.04 with green) in poloidal coordinates obtained with IDE mapped to R_{major} with a linear interpolation are also represented with the in fig. 4.2 and fig. 4.1.

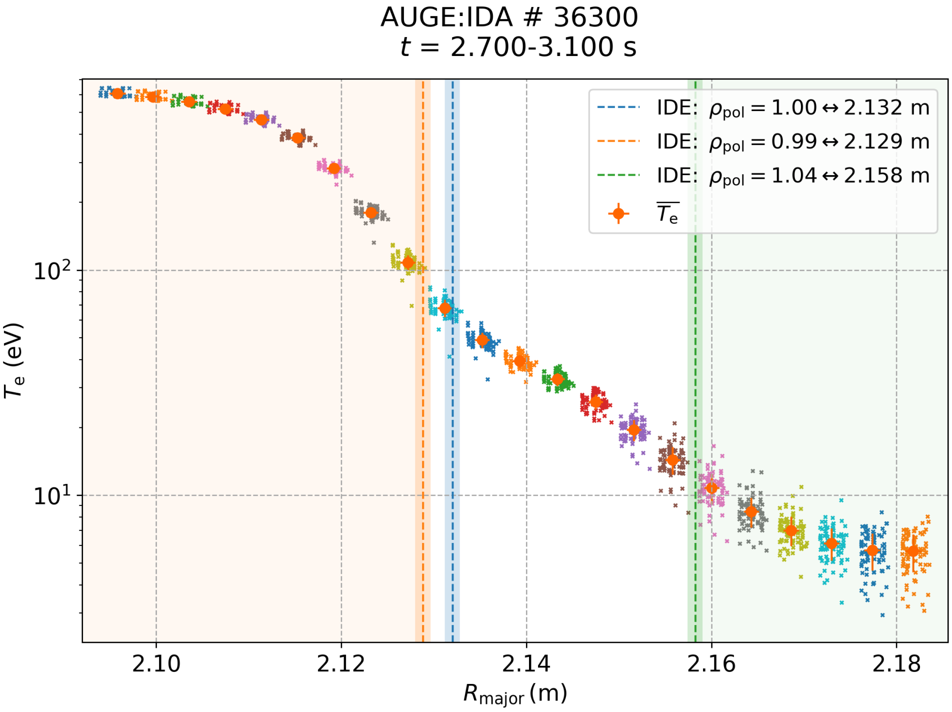

Figure 4.1.: Temperature profile in logarithmic scale from AUGE:IDA # 36 300, a type I-ELMy-H-mode with $I_p = 0.8$ MA, using the new collisional radiative model within the IDA framework. The orange bar ($\rho_{\text{pol}} = 0.99$) corresponds to lower limit bellow which deuterium cyanide laser interferometry (DCN), electron cyclotron emission (ECE), and Thomson scattering spectroscopy (TS) contribute to the evaluation more than the THB data. The green bar is the corresponding superior limit ($\rho_{\text{pol}} = 1.04$) and the blue bar represents the separatrix ($\rho_{\text{pol}} = 1$) position in natural coordinates. The points within a cluster with the same color are the different temperature values for the same poloidal coordinate for the different time points within the chosen time interval for the analysis ($t = 2.7 - 3.1$ s). The orange circles represent the temperature mean and averaged values per radial channel in the studied time interval of 400 ms.

In order to study the profiles in quasi steady state conditions, it is necessary to filter the type-I-ELMs in the H-mode discharges. To do that, an ELM shotfile is written using the software *ELM detection v4.1*. This program identifies the time phases corresponding to the signatures of an ELM in the poloidal divertor current I_{polsoli} and later a program separates the time trace spectrometer signal in data with and without ELM by Boolean masking, also taking into the account the recovery time for an ELM [Kir14] and the shift time between the signal in the divertor and the midplane, to where the diagnostics are mapped. The corresponding ELM synchronization for the discharge presented in fig. 4.1 and fig. 4.2 can be seen in the appendix A.1.

In fig. 4.1 the error bar within one single data point representing the systematic uncertainties (due to a bad calibration or a wrong atomic cross-section in the CRM) is not included. Instead of these errors, the statistical uncertainties for each cloud of points, corresponding to the same poloidal coordinate for different time points within the studied time window, is used. For all of these radial channels represented by a different colour in fig. 4.1, the mean and standard deviation values are calculated. The standard deviation values represent an upper limit for the statistical errors caused by the photon noise or plasma fluctuations.

As stated in the beginning of the chapter, a major part of this thesis is to determine the near SOL gradient lengths for temperature and density profiles. For this purpose, first the limits of the near SOL, and more specifically the position of the separatrix must be determined. Evidence for a purely exponential decay in the near SOL for the heat flux, density and temperature profiles can be found in different studies, involving experimental data [Sun15, Sun17b, Hos19] as well as theoretical models [Sta10]. Thus, it will be assumed as a first step, that the near scrape-off layer is defined for each variable in an independent way ($q_{\|\mathrm{e}}$, n_e, T_e) as the region from the separatrix on where its corresponding fall-off length (namely $\lambda_{q_{\|e}}$, λ_{n_e}, λ_{T_e}) is constant.

In order to identify the limits of the near SOL, it is chosen to work with logarithmic scales and derivatives. If the fall-off length is constant, the purely exponential radially decaying profile will result in a linear function with a constant slope after a logarithmic transformation. On the contrary, if the decay length changes, a kink in the slope would be seen in the logarithmic regime. This change in the linear trend of the profiles can be identified by calculating the derivatives of the profiles. This can be done with the profiles obtained from the CRM within the IDA work frame, as the AUGE:IDA profiles obtained are smooth, presenting continuous derivatives over the domain of interest. However, this evaluation with derivatives cannot be implemented with diagnostics that do not deliver smooth profiles, like the Thomson Scattering System. In the following, two different approaches to calculate the profile derivatives for the THB data are presented.

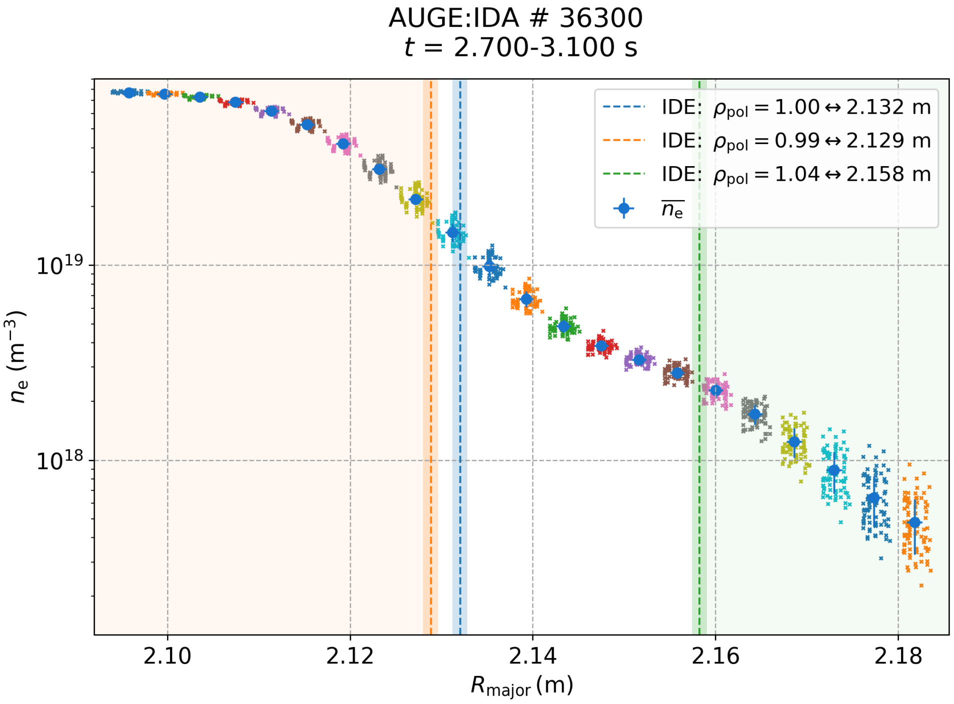

Figure 4.2.: Density profile in logarithmic scale for AUGE:IDA # 36 300, a type I-ELMy-H-mode with $I_\mathrm{p} = 0.8\,\mathrm{MA}$ for 400 ms ($t = 2.7 - 3.1\,\mathrm{s}$), using the new collisional radiative model within the IDA framework (cf. fig. 4.1 for the T_e profile). The shaded regions correspond to the domains where the THB evaluation is not reliable.The blue circles with errorbars are representing the mean as well as the standard deviation values for all the time points for each cluster of data points.

4.2. Finite Difference Approach for the Derivative Profiles

As this analysis is about radially decaying profiles, negative derivatives in logarithmic scale are preferred. The first approach is implemented using central differences by stepping forward half a step (Δx) and backward half a step for each time point, as this type of finite differentiation yields the most accurate results [Lan10] with an error estimation from the Taylor expansion to the order of $\mathcal{O}(\Delta x^2)$. First derivatives allow to visualize fall-off lengths as the decay length can be expressed in terms of the first derivative of the logarithm of the studied variable:

$$\lambda_{T_\mathrm{e}}(\mathrm{mm}) = \frac{1}{-\bigtriangledown \log\left[T_\mathrm{e}/\mathrm{eV}\right](\mathrm{m}^{-1})} \cdot 1 \cdot 10^3 \tag{4.3}$$

This inverse relation between the derivative and the decay length can also be seen in both fig. 4.3 and fig. 4.4: the larger the first derivative, the smaller the corresponding decay length is. And therefore, the narrower the SOL is, and the steeper and faster the temperature profile decays. The first derivative thus indicates the absolute steepness of the profile.

Contrary to initial assumption in which we have defined the near SOL as the region where the decay length remains constant, it can be seen that there is no constant trend around the region outside the separatrix, but that the derivative for both temperature and density profiles changes hugely around the separatrix region. It is also not constant inside the separatrix in the pedestal region or across the near SOL as stated in [Sun15, Sun17a, Hos19]. Due to the transport changes at the separatrix, there are narrower values for the decay length closer to the separatrix, which experience a quick broadening some millimeters further away from R_{sep}. In general it is observed that the lowest/narrowest temperature decay lengths are achieved in the pedestal region, while for the density the lowest/narrowest value is displaced outwards.

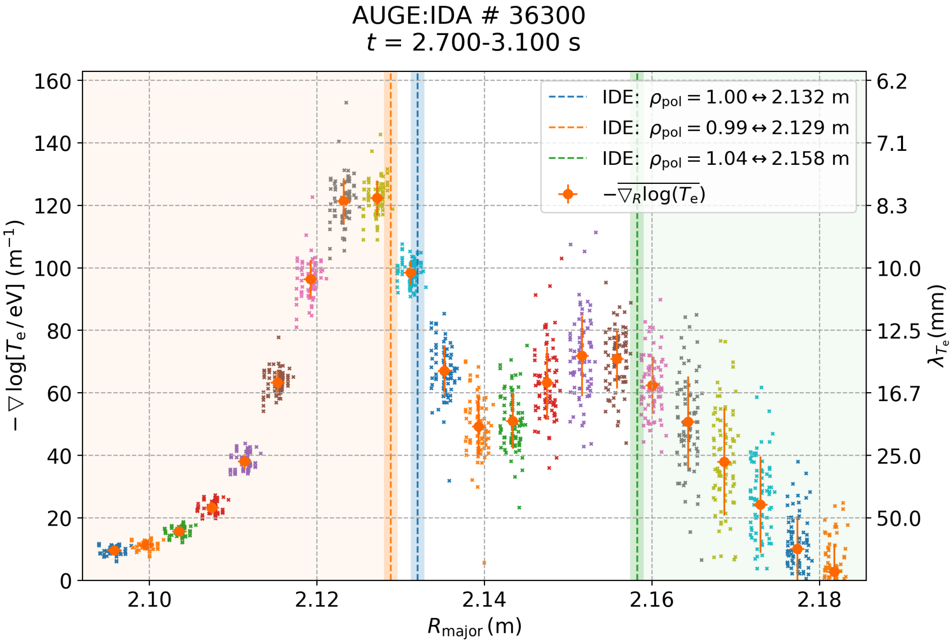

Figure 4.3.: Double y-axis plot of the negative first derivative with central difference of the logarithm of the temperature profile and its corresponding fall-off length. The mean values for the respective cluster are represented with orange circles. The narrowest values for the temperature decay length are observed inside the separatrix and then a quick broadening (higher values of λ_{Te}) across the region from closed to open field lines is observed.

As the fall-off length does not seem to be constant but varies massively around the separatrix, the focus lies now in studying the changes in the steepness and in the curvature of the profiles by analyzing the second derivatives. In order not to loose precision, the second derivative is directly calculated from the original points via direct central difference. This is done calculating the coefficients for the finite difference equation from the Taylor expansion evaluated for the original central points, dropping the outermost points of the radial range. In case of an uniform grid with a constant inter-space (Δx), this is equivalent to:

$$f_i'' = (f_{i+1} - 2 \cdot f_i + f_{i-1})/(\Delta x)^2 \tag{4.4}$$

where f_i'' is the second derivative correspondent to the i-th component. However, the array R_{major} conform a non-uniform grid, so eq. (4.4) needs to be adapted for this case. This is shown

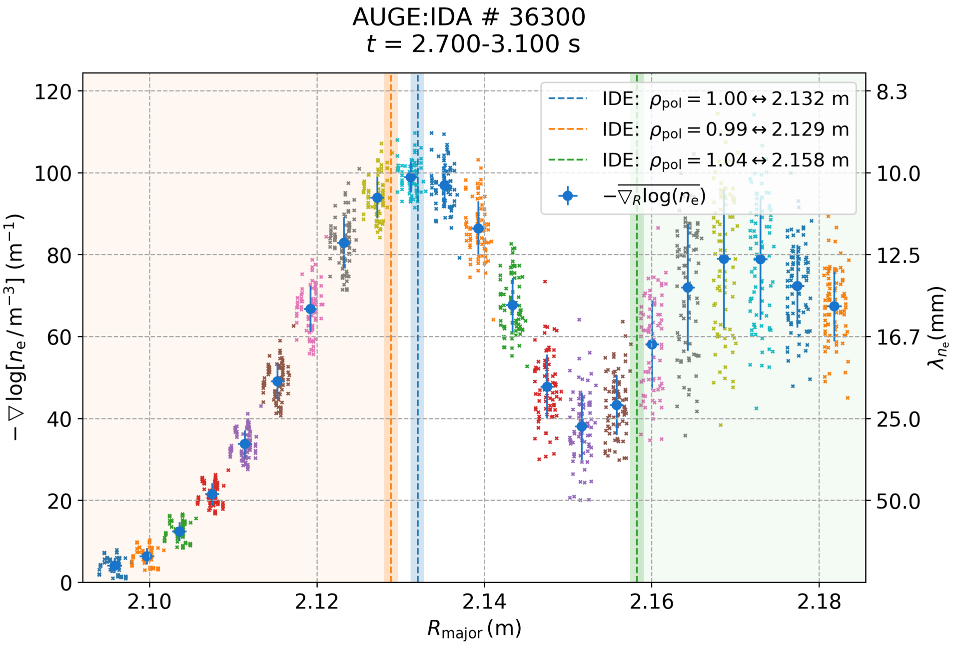

Figure 4.4.: Double y-axis plot of the negative first derivative with central difference of the logarithm of the density profiles and its corresponding fall-off length. The blue circles represent the mean values of the profiles. The lowest fall-off length values are observed close to the separatrix followed by a quick broadening in the near SOL.

in appendix A.3. For the evaluation of the shape of the whole dataset of discharges, a piece-wise linear (PWL) model [Nil20] is used for the *negative* second derivatives of the smooth profiles to find kinks. In this model 5 points are fit giving to 4 straight lines. For each point there is an x and y coordinate but the start and end positions are fixed. In this way, only a set of 8 parameters ($M_{\mathrm{P}} = [y_0,\ y_1,\ y_2,\ y_3,\ y_4,\ x_1,\ x_2,\ x_3]$) needs to be optimized.

From this fit, the two central points $[x_1 = R_{\mathrm{left}},\ x_2 = R_{\mathrm{lowest}}]$ correspond to the extrema positions of the profile, i.e. the lowest negative curvature point ($R_{\mathrm{Te,NEG}},\ R_{\mathrm{Ne,NEG}}$) and the highest positive curvature point ($R_{\mathrm{Te,POS}},\ R_{\mathrm{Ne,POS}}$) for both density and temperature profiles. As the *negative* derivatives are used for the calculation, the signs of the curvature are inverted. In this way, it can be seen that the maximum (minimum) of the *negative* second derivative in logarithmic scale is the point of lowest negative (highest positive) curvature.

For the errors of the first and second derivatives, only the standard deviations for the correspondent values per radial channel are regarded. The errors of the extrema position are given by the piece-wise linear model from the MAP (maximum a posteriori) [Bre90] estimate, which can be used to obtain a point estimate of an unobserved quantity on the basis of empirical data.

For the discharge # 36300 in fig. 4.5, the point of highest positive curvature in the temperature profiles corresponds to $R_{\mathrm{Te,POS}} = 2.132\,\mathrm{m}$. In fig. 4.5 it can also be seen that point of highest positive curvature matches the separatrix position (i.e. blue bar at $R_{\mathrm{sep}} \mid \rho_{\mathrm{pol}} = 1$). It should be again noted that the separatrix position has not received an special treatment in the CRM.

This agreement between the position of the separatrix and the point of positive curvature in the temperature profiles ($R_{\mathrm{Te,POS}} = R_{\mathrm{sep}}$) has also been seen in all 21 H-mode discharges from the built database and is studied in more detail in section section 4.4.

In the case for the L-mode database, a match between the position of the separatrix and the point of lowest curvature in the temperature profile is seen ($R_{\mathrm{Te,NEG}} = R_{\mathrm{sep}}$). The same is observed in the density profiles ($R_{\mathrm{Ne,NEG}} = R_{\mathrm{sep}}$).The curvature for a density profile of an L-mode example and the match between the separatrix position and the point of lowest negative curvature of the density profile ($R_{\mathrm{Ne,NEG}} = R_{\mathrm{sep}}$) are shown in fig. 4.6.

For the high density L-mode discharges (density shoulder formation discharges), matches between the position of the separatrix with the highest point of curvature have been observed in both temperature and density profiles (cf. appendix A.2).

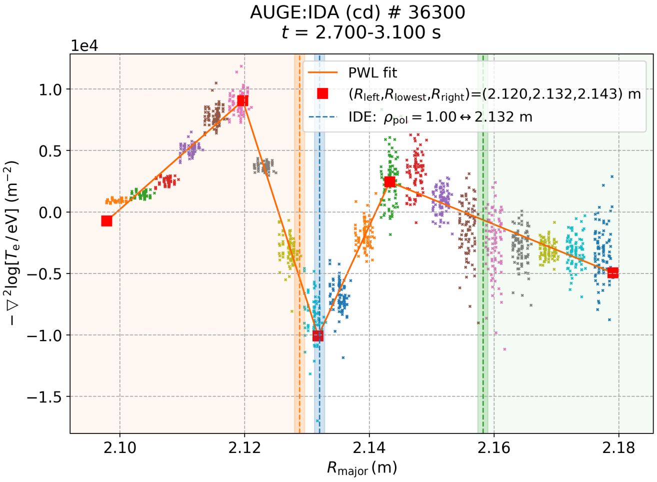

Figure 4.5.: Second negative derivative (calculated directly from the original profile with central difference) of the logarithm of the temperature profile for an H-mode discharge (# 36 300, $t = 2.7$–$3.1\,\mathrm{s}$). The optimized points (red squares) obtained from the PWL fit (orange line) are also plotted. It can be seen that the minimum of the second negative derivative profile (R_{lowest}), correspondent to the point of highest positive curvature, matches the position of the separatrix reconstructed with IDE ($R_{\mathrm{Te,POS}} = R_{\mathrm{sep}} = 2.132\,\mathrm{m}$).

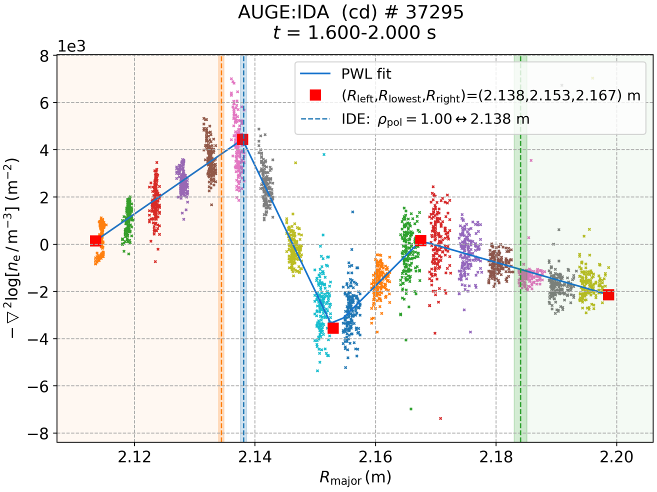

Figure 4.6.: Second negative derivative for a medium-density L-mode example (# 37295, $t = 1.6$–$2\,\mathrm{s}$). The point of lowest negative curvature is at $R_{\mathrm{Te,POS}} = 2.138\,\mathrm{m}$, matching the position of the separatrix reconstructed using IDE.

4.3. Analytical Approach for the Derivative Profiles

Another approach for the calculation of the profile derivatives is to interpolate each time profile contained in the studied interval with a spline function and then calculate the derivatives (first, second and also third order) in an analytical way. Quintic splines (k=5 with k as the degree of the spline function) are preferred for the interpolation of the original profiles because then the third derivatives (quadratic splines, i.e. $k = 2$) are smoother. To obtain the points of highest positive curvature and lowest negative curvature with this method, the roots of the third derivatives of the splines are calculated (i.e. $r_0 \mid f(r_0)''' = 0$). This approach supports the results from the finite difference derivation, showing the same shape and the same matches between the separatrix position and the extrema of the curvature profiles. This proves that the shape of the derivatives observed, as well as the agreements for the estimation of R_{sep}, are robust qualifiers to indicate the relative position of the separatrix within a smooth profile. In fig. 4.7 and fig. 4.8 the quintic splines used to interpolate the data points for the profiles and then calculate the first, second and third derivatives are shown. A *root-finding* algorithm was implemented to calculate the roots of the third (in red fig. 4.7) and second (in cyan in fig. 4.7) derivatives. The mean and standard deviation values for the roots for all time profiles are indicated with the color-coded error bars.

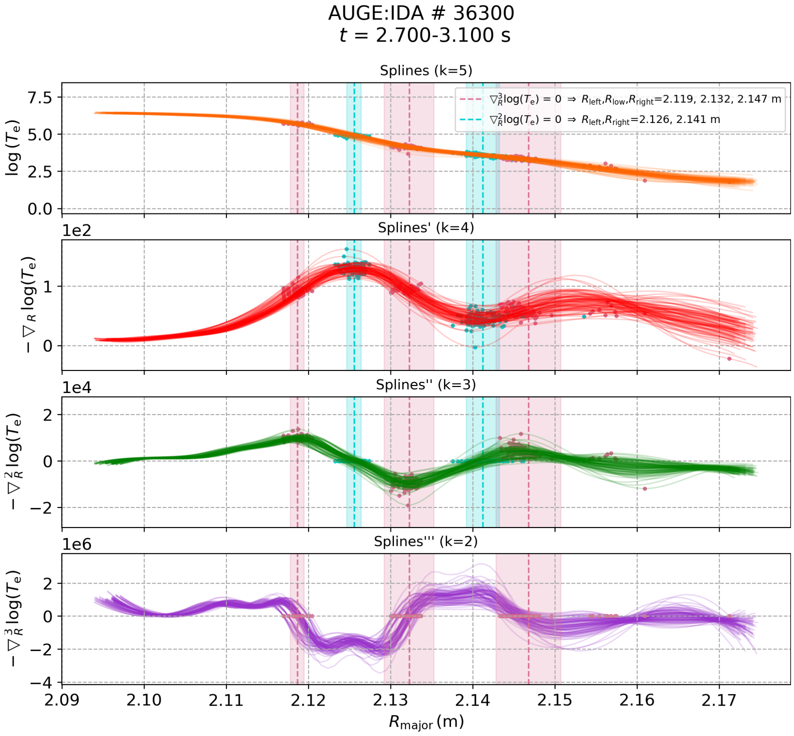

Figure 4.7.: Spline interpolation for the logarithmic temperature values and its derivatives (first, second and third order) for discharge # 36 300 $t = 2.7 - 3.1$ s. The roots for the second derivatives (in cyan) and the roots for the third derivatives (in red) are plotted. These root positions are then projected to the profiles with a lower order of derivation. With this method the point with the highest positive curvature ($R_{\text{Te,POS}}$) corresponds to the central root for the third derivative at 2.132 m, matching the separatrix position $\rho_{\text{pol}} = 1$. The same value was obtained for $R_{\text{Te,POS}}$ with the finite difference approach.

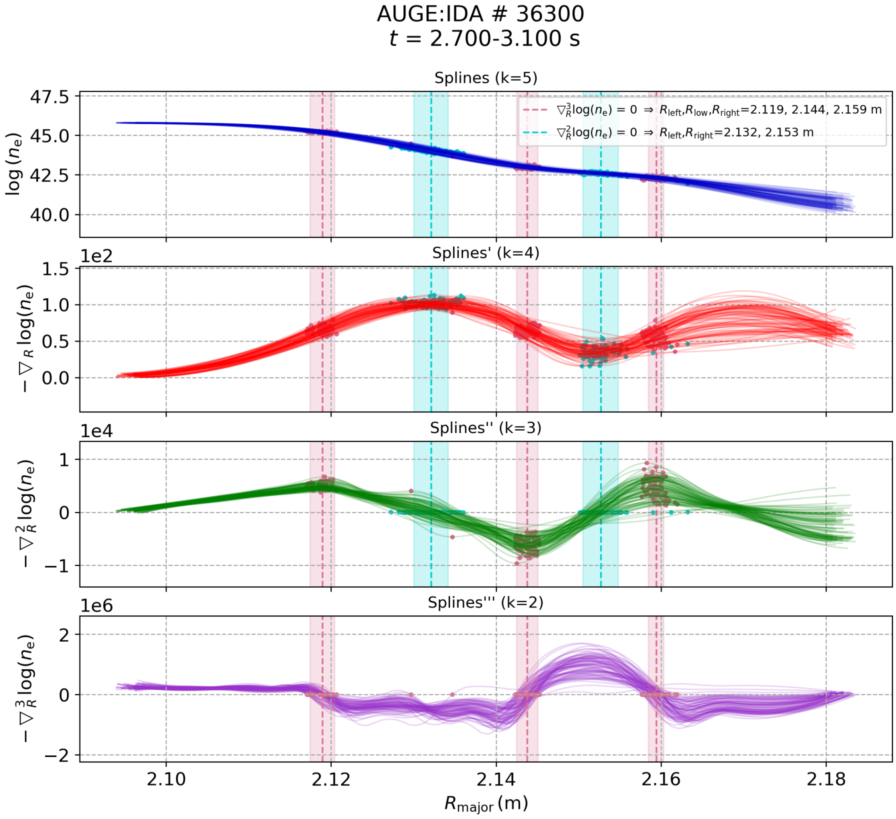

Figure 4.8.: Spline interpolation for the density profile and its derivatives (first, second and third order) for discharge # 36 300 $t = 2.7 - 3.1$ s. Same representation as in fig. 4.7 which shows the temperature splines and their roots.

4.4. Self-consistent Connection between the Structure of the Temperature Profile and the Separatrix Position

From the curvature studies it can be concluded that the position of the separatrix can be derived from the shape of the temperature structure, specifically the points of highest positive curvature and lowest negative curvature indicate the position of the separatrix.

In particular for the H-mode database, an almost 1:1 correlation between the point of highest positive curvature and the separatrix position ($R_{\text{sep}} = R_{\text{Te,POS}}$) can be seen when using the IDE code for the equilibria reconstruction, as shown in fig. 4.9. In this way, we can conclude from the analysis of the structure of the temperature profiles for the H-mode database in conduction-limited regimes under attached conditions, that the point of highest positive curvature is a very good qualifier to estimate the relative position of the separatrix within a profile.

A symmetry between the point of lowest negative curvature and highest positive curvature has been observed for the temperature profiles of the complete H-mode database. In fig. 4.10, the points of lowest negative curvature are also plotted together with the points of highest positive curvature against the separatrix position by IDE. Both trends present the same slope with an offset of 12.5 mm, i.e. the points of lowest negative curvature lie at a distance of 12.5 mm from the separatrix position: $R_{\mathrm{TeNEG}} - 0.0125\mathrm{m} = R_{\mathrm{sep}}$.

The analysis of the density curvature profiles have not shown any clear trend or match with respect to R_{sep}, as we can see in fig. 4.11.

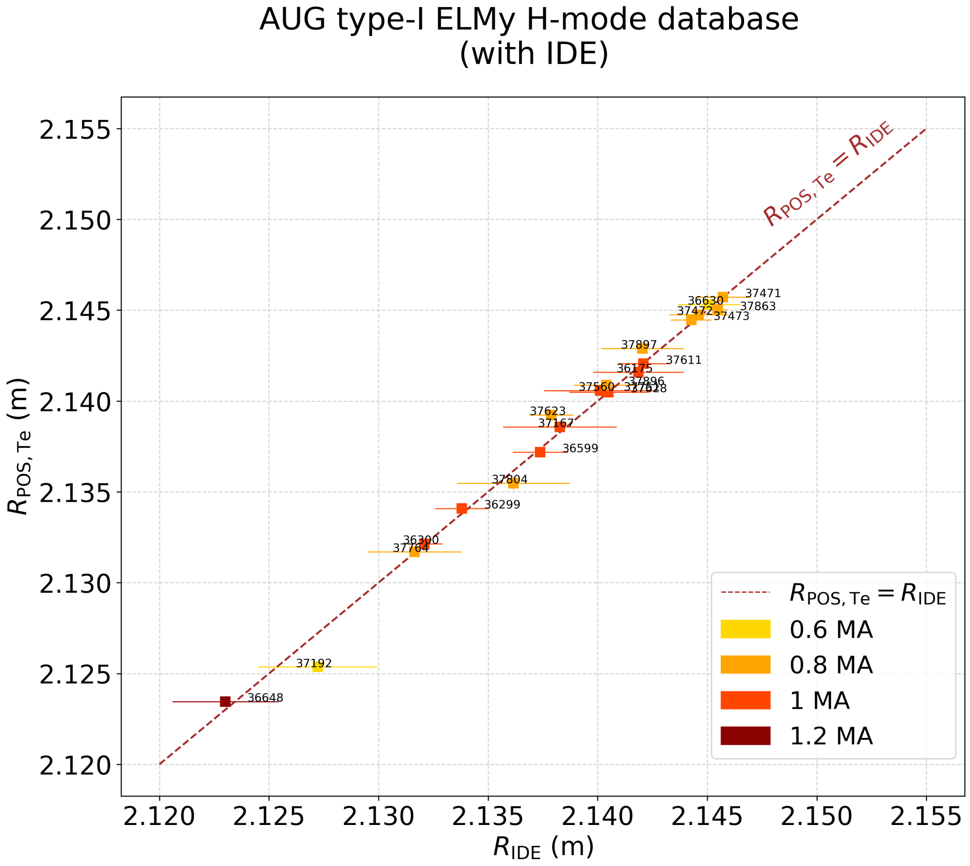

Figure 4.9.: Correlation between the separatrix position by IDE and the point of highest positive curvature in the temperature profiles for 21 discharges that compose the built database. The color coding shows discharges with different plasma current.

A less precised correlation is observed in fig. A.5 (in the appendix) when using the code EQH to read the equilibria. Nevertheless, it can be seen that the miss-alignment is not higher than 5 mm in any case. Thus it is concluded that EQH could be a good alternative for studies with radial uncertainties over 5 mm.

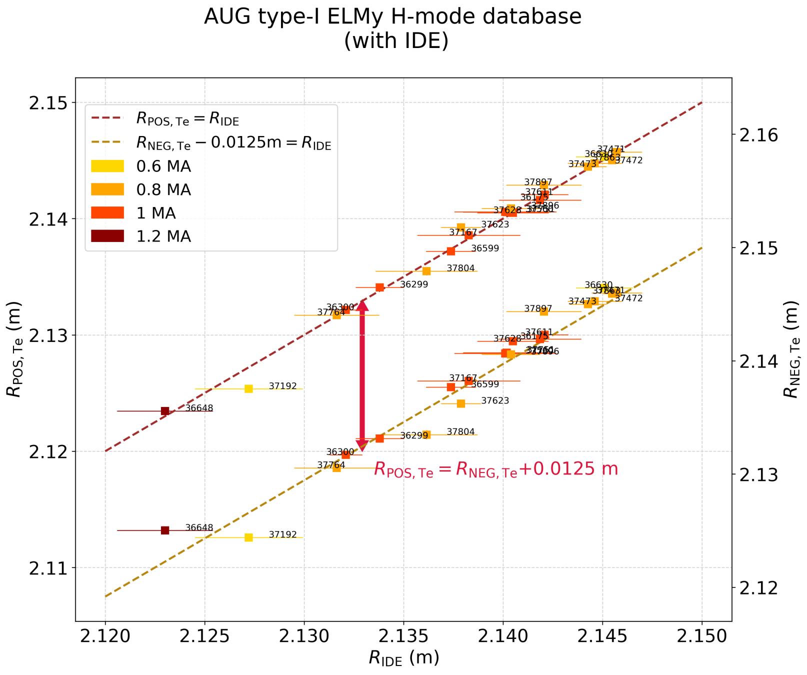

Figure 4.10.: Same representation as in fig. 4.9 but including also the points of lowest negative curvature, which present an offset with respect to the separatrix position of 12.5 mm.

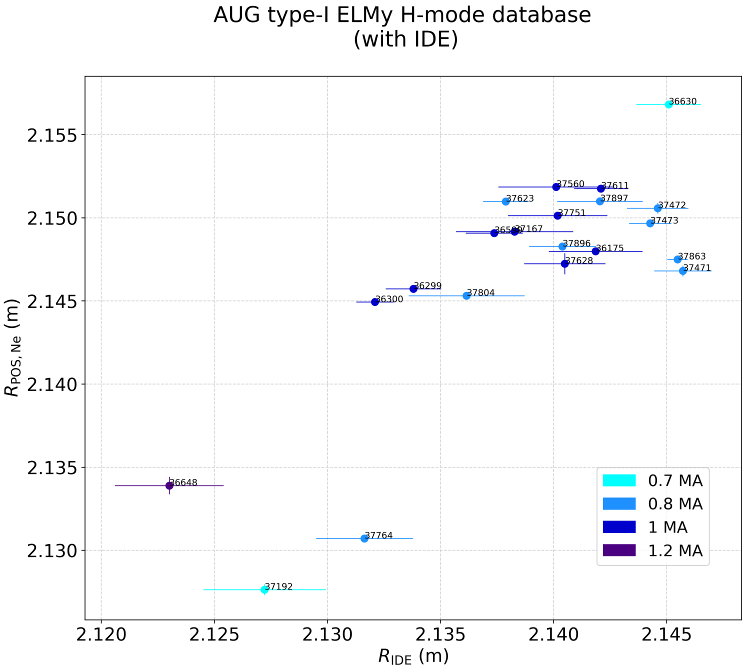

Figure 4.11.: Correlation between the separatrix position by IDE and the point of highest positive curvature in the density profiles for 21 discharges that compose the built database using cold colors to represent the different plasma currents. No clear trend or relation can be seen, in an opposite way to the temperature curvature analysis.

For the L-mode database, in addition to the discharges in the conduction-limited regime, three discharges (#35 893, #37 820 and #37 821) in the linear regime studying different effects on density shoulder formation in the far SOL, have also been included. Matches between R_{sep} and the negative curvature points in both temperature and density profiles have been detected for low and medium density L-mode discharges while agreements between the separatrix position and the point of highest positive curvature are observed for the density shoulder formation discharges.

In fig. 4.12 the matches between the extrema of the temperature curvature profiles and R_{sep} are presented. In opposition to the H-mode trend, the separatrix position matches the point of lowest negative curvature in the temperature profiles ($R_{\mathrm{TeNEG}} = R_{\mathrm{sep}}$) in all L-mode discharges in the conduction-limited regime. For L-mode discharges in the linear regime, #35 893 and #37 820 present the same agreement ($R_{\mathrm{TePOS}} = R_{\mathrm{sep}}$) as the H-mode database.
However for # 37 821 the match observed is $R_{\mathrm{TeNEG}} = R_{\mathrm{sep}}$. This suggests that in the linear regime where convection mechanisms predominates over conduction, the curvature profile changes, presenting different extrema. A more detailed study would be needed to address the agreements in convective regimes. It can also be observed that both trends in the temperature matches ($R_{\mathrm{TePOS}} = R_{\mathrm{sep}}$ and $R_{\mathrm{TeNEG}} = R_{\mathrm{sep}}$) within the studied L-mode database, present the same slope with an offset of 13 mm.

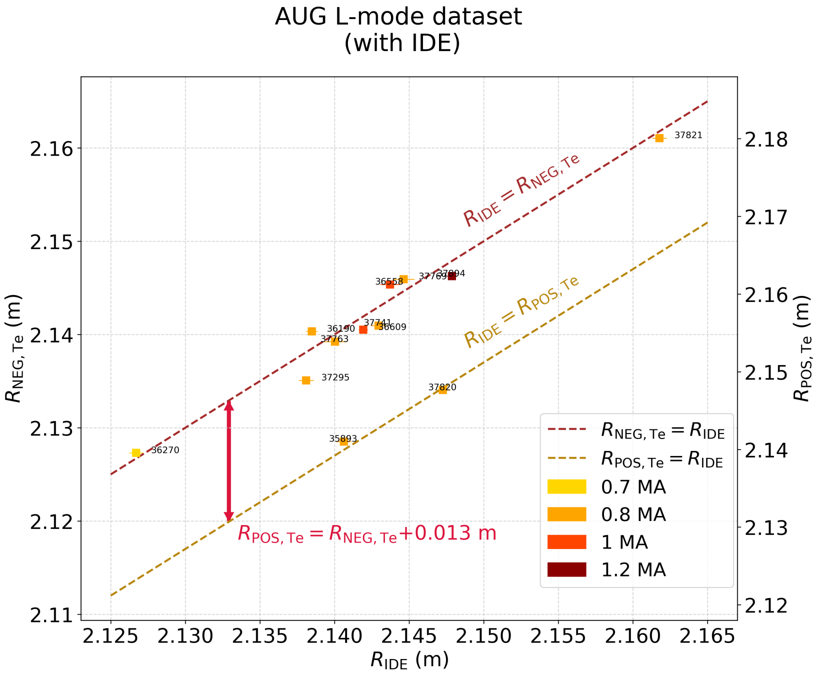

Figure 4.12.: Correlation between the separatrix position by IDE and the point of lowest negative and highest positive curvature in the temperature profiles for 12 L-mode discharges that compose the built database. For the temperature analysis warm colors have been chosen to represent the different plasma current values within the studied database.

The same trends are observed in the curvature density profiles for the L-mode database, shown in fig. 4.13. This means that in all L-modes in conduction-limited regimes, R_{sep} matches the point of lowest negative curvature and that the linear regime discharges present again different results with respect to the discharges in conduction-limited regimes. In the density study, the discharges #37 821 and #37 820 present a match between the point of highest positive curvature and R_{sep} while the discharge #35 893 present the same trend as the conduction-limited L-modes. This would imply that the linear regimes discharges present a match between the separatrix position and the point of lowest negative curvature in either the temperature, density or both profiles. In the L-mode case important trends in the density curvature profiles are seen (in opposition to the H-mode, where the matches were only observed the temperature curvature profiles). The offset between the curvature trends for the density analysis is of 11 mm.

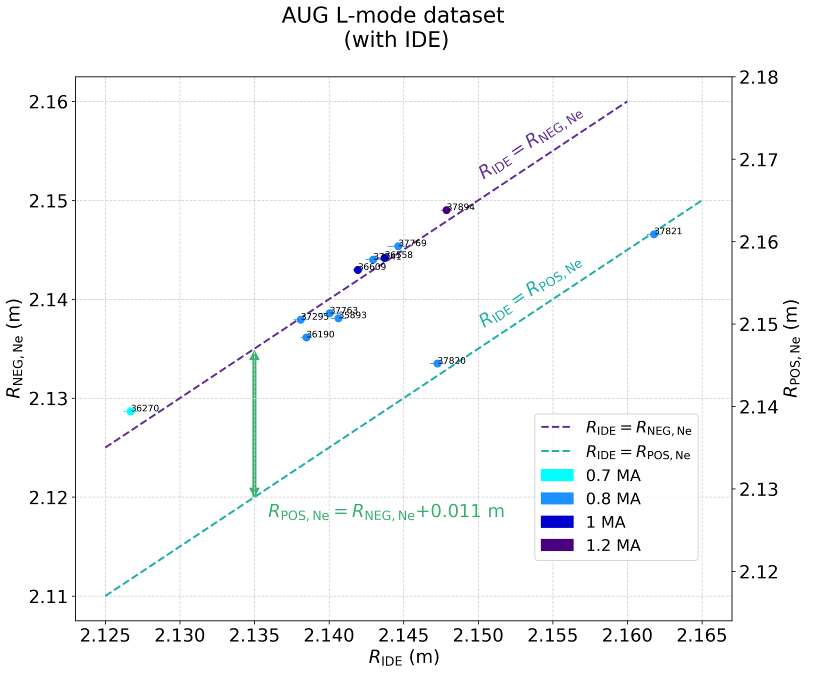

Figure 4.13.: Correlation between the separatrix position by IDE and the point of lowest negative and highest positive curvature in the density profiles (cold colors) for 12 L-mode discharges that compose the built database. The color coding shows discharges with different plasma current.

5.1.5 D Modelling for the Heat Balance Equation from Closed to Open Field Lines

In order to understand the physical mechanisms responsible for the agreement between the position of the separatrix and the points of highest positive curvature and lowest negative curvature from the temperature profiles showed in last chapter, a $1 + 1/2$ D SOL modelling for the heat balance equation for the upstream region (cf. section 2.4.2) from closed to open field lines is presented in the following.

In this model, a simplified $1 + 1/2$ D geometry with a full perpendicular description (by means of the radial coordinate R_{major}) and an assumption-limited description for the parallel coordinate (by means of the z coordinate along the field lines, $z \cong 2\pi r$) is used. This model is based on [Kei82], which solves the perpendicular heat conduction, treating parallel losses through a constant sink term describing the parallel heat losses to the divertor. In this model a 1.5 D near SOL geometry is used, which means that it is assumed that the temperature along a field line remains close to constant over most of its length:

$$\int_0^{L_c} T_{\mathrm{e}}(R,z)\,\mathrm{d}z \approx \text{constant} \Rightarrow T_{\mathrm{e}}(z,R) = T_{\mathrm{e}}(R) \tag{5.1}$$

This assumption for the parallel coordinate is not a limiting premise. The reason for this is because of the extreme non-linearity of the parallel heat conduction term, dominated by the Spitzer-Härm electron temperature conduction. Due to this transport mechanism the temperature along a field line remains close to constant over most of its length, with a decay only in the target-plate vicinity. So over most of the region where radial transport takes place, the temperature is constant along z, which is the basic assumption of the 1.5 D model.

In the version described in [Kei82], the perpendicular conductivity $\kappa_{\perp \mathrm{e}} = -n_{\mathrm{e,u}}\ \chi_{\mathrm{e}}$ in terms of the radial density profile and the perpendicular diffusivity constant, assumed to be radially independent. In opposition to the non-limited assumption for the description of the parallel coordinate, this is a critical assumption, as a change in transport across the separatrix could occur due to radial variation of the perpendicular conductivity $\kappa_{\perp \mathrm{e}}$, which could show up as a contribution to the second derivative against the radial coordinate of the temperature profile in the form of:

$$\delta\left[\frac{\mathrm{d}^2 T_{\mathrm{e}}}{\mathrm{d}R^2}\right] = -\frac{\mathrm{d}(n_{\mathrm{e,u}}\ \chi_{\mathrm{e}})}{\mathrm{d}R} / \frac{\mathrm{d}T_{\mathrm{e}}}{\mathrm{d}R} \tag{5.2}$$

In the modelling presented in this chapter, a radial dependence for the perpendicular conductivity $\kappa_{\perp \mathrm{e}}$ is included by means of introducing a radial dependant density profile ($n_{\mathrm{e}}(R)$). In this chapter, different simple assumptions for the input parameter set and the initial conditions are incorporated to the model in order to solve the ordinary differential equation (ODE) derived for the heat balance equation from closed to open field lines for the conduction-limited H-mode and L-mode scenarios.

The starting point is to calculate the integrated power fluxes for the perpendicular and parallel direction ($Q_\perp$ and $Q_\parallel$) from the power densities ($q_{\perp\mathrm{e}}$ and $q_{\parallel\mathrm{e}}$), derived already in section 2.4.2. For the direction along the field lines, the predominant heat mechanism is described by the Spitzer-Härm electron conduction equation:

$$q_{\parallel\mathrm{e}} = -\frac{\kappa_0}{L_\mathrm{c}}\; T_\mathrm{e}^{\frac{7}{2}}(R) \tag{5.3}$$

where κ_0 is the Spitzer-Härm electron heat conduction coefficient, with a value of [Str11]:

$$\kappa_0 \cong 2000\,\mathrm{W\ eV^{-7/2}m^{-1}} = 2000\,\frac{1}{1.6\cdot 1\cdot 10^{-19}}\;\mathrm{eV^{-5/2}m^{-2}s^{-1}} \tag{5.4}$$

and L_c the connection length.

For the cross-field direction, the heat transport can be described using the Fourier‘s law:

$$q_{\perp\mathrm{e}} = -n_{\mathrm{e,u}}\,\chi_\mathrm{e}\,T_\mathrm{e}'(R) \tag{5.5}$$

with ’ denoting the first derivative against the major radius. The perpendicular conductivity $\kappa_{\perp\mathrm{e}}$ is expressed in terms of the radial density profile ($n_{\mathrm{e,u}}$) and the perpendicular diffusivity constant (χ_e).
These power densities are integrated over their corresponding perpendicular surface areas, either the magnetic flux surface ($A_2 = y\cdot z$) or the area between two magnetic flux surfaces ($A_1 = \mathrm{d}R\cdot z$). Both areas are depicted in fig. 5.1, where the volume between two flux surfaces (V), with a coordinate system composed by R, $z = 2\,\pi r$ (with r as the minor radius) and $y = 2\,\pi R$ is depicted:

$$V = \mathrm{d}R\cdot y\cdot z = 4\pi^2\;R\,r\,\mathrm{d}R \tag{5.6}$$

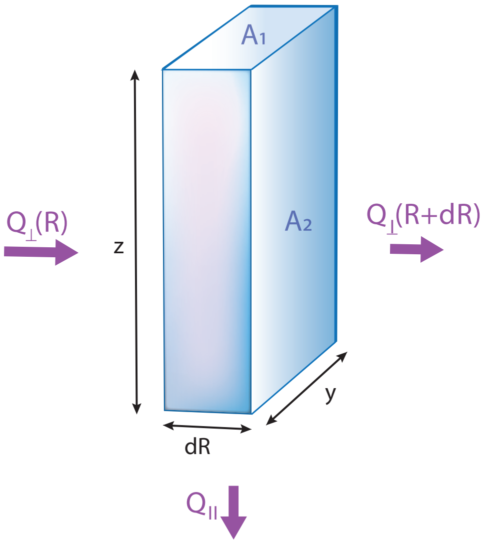

Figure 5.1.: Schematic illustration for the volume between two magnetic flux surfaces (V). The parallel integrated power density $Q_\parallel$ corresponds to the sink term decribing the losses to the divertor. Two different perpendicular heat contributions are depicted: the heat flux inside the confined region without the parallel losses ($Q_\perp(R)$) and the heat flux in the open field lines region, after the losses to the divertor plates ($Q_\perp(R+\mathrm{d}R)$).

In this way the heat balance in perpendicular and parallel direction for the integrated heat fluxes would be:

$$Q_{\|} \; + \; (Q_{\perp}(R + \mathrm{d}R) - Q_{\perp}(R)) = 0 \tag{5.7}$$

$$q_{\|e} \cdot A_1 \; + \; A_2 \, (q_{\perp e}(R + \mathrm{d}R) - q_{\perp e}(R)) = 0 \tag{5.8}$$

$$q_{\|e} \cdot \mathrm{d}R \cdot y \; + \; y \cdot z \, (q_{\perp e}(R + \mathrm{d}R) - q_{\perp e}(R)) = 0 \tag{5.9}$$

Including the expressions for the power densities derived above and grouping the coefficients, the following differential equation is obtained:

$$c_0 \, T_{\mathrm{e}}''(R) \; - c_1 \, T_{\mathrm{e}}^{\frac{7}{2}}(R) = 0 \tag{5.10}$$

with the coefficient c_0 accompanying the radial transport term:

$$c_0 = -2\pi \; r \; n_{\mathrm{e,u}} \; \chi_{\mathrm{e}} \tag{5.11}$$

and c_1 representing the parallel transport term.

$$c_1 = -\frac{\kappa_0}{L_{\mathrm{c}}} \tag{5.12}$$

The different input parameters grouped in the coefficients are studied for different cases in the following sections.

5.1. Modelling for the H-mode Scenario

The previous differential equation eq. (5.10) is solved for an H-mode case in attached conditions. For the inverse value of the connection length, an hyperbolic tangent function, positive and centered in R_{sep}, is used as transition function from closed to open field lines:

$$\frac{1}{L_{\mathrm{c}}} = \frac{1}{2 q_{95} \pi R} \cdot \tanh\left[((R - R_{\mathrm{sep}}) * \mathrm{width}) + 1\right] \tag{5.13}$$

represented in fig. 5.2. A width factor is also included in eq. (5.13). It indicates how abruptly the connection length changes from the region from closed to open field lines. Lower values imply smoother transition functions. Thus, a value of 350 is chosen for the H-mode case.

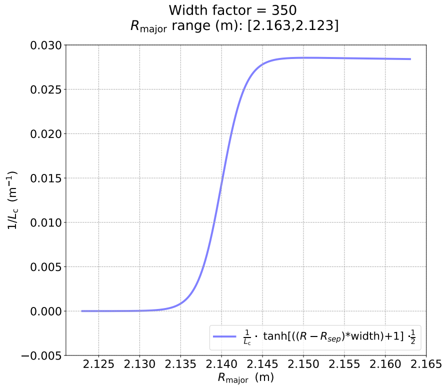

Figure 5.2.: Inverse of the connection length for the modelled H-mode case with a width factor of 350.The separatrix position is set at $R_{\mathrm{major}} = 2.14\,\mathrm{m}$.

For the density profile, an experimental profile from the discharge # 37 623, as a function of the major radius, is used. The profiles for the time interval chosen ($t = 5.5$-$6\,\mathrm{s}$), are interpolated with splines and the averaged profile, represented in fig. 5.3 is chosen as input parameter.

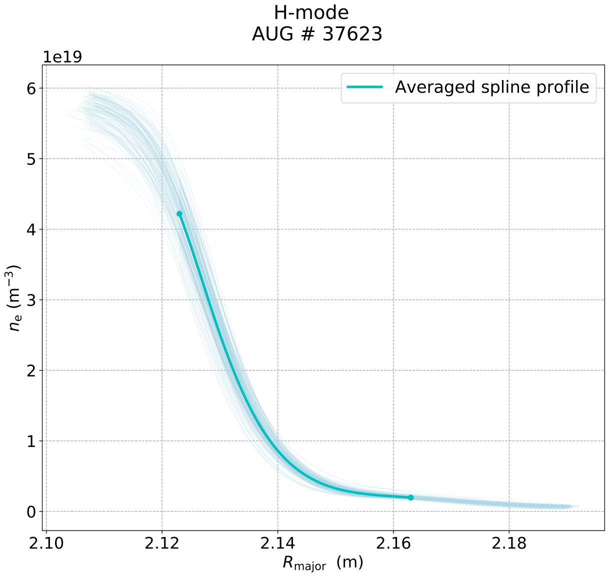

Figure 5.3.: Density profiles within the time interval $t = 5.5$-$6\,\mathrm{s}$ for # 37 623, $I_\mathrm{p} = 0.8\,\mathrm{MA}$. The spline interpolation for the mean values is also plotted with the brighter cyan line.

The other input variables to be studied are: the separatrix position R_{sep}, the safety factor q_{95} and the electron diffusivity constant χ_e. For the separatrix position and safety factor (in the header of fig. 5.4), the values chosen are obtained from the experimental data for # 37623. For the diffusivity constant, a value of $9.5\,\mathrm{m^2 s^{-1}}$ is chosen. This value is within the order of magnitude estimate from [Man20]. Typical radial velocities in the SOL are on the order of 100–1000 m/s, and typical correlation times on the order of 10 µs. This corresponds to typical SOL diffusion coefficients on the order of 0.1–10 $\mathrm{m^2 s^{-1}}$ which are also in the typical range used in transport codes.

For the computation of the solution of the second order ODE, the routine *Odeint* from python is used. This routine solves first order ODEs, so the second order ODE must be given as a system of two first order differential equations. In this routine the iterative *Adam's* method for non-stiff equations is used. It is based on the *Runge-Kutta* methods, where solutions of ODEs are approximated by a weighted sum of the slopes for an specific point, but in this case an adaptative stepsize is used. In this way, the *Adam's* method proves to be more economical than the *Runge-Kutta* method in most cases [Lan10].

In fig. 5.4 the input parameters are represented, as well as the solution profiles. From the plots it can be seen how well the separatrix position (introduced as a parameter in the system) matches the point of highest positive curvature of the modelled temperature profile, i.e. the minimum of the *negative* second derivative. The modelled profile shows the consequences of the parallel losses to the divertor via the Spitzer-Härm electron conduction.

This can be understood by considering that the negative radial gradients of the temperature are proportional to the radial heat flux and this is reduced going outwards due to the parallel losses.

In fig. 5.5, it can be be seen that the shape obtained from the modelling matches very well the experimental analysis. The highest values of the negative first derivatives are seen inside the separatrix in both modelled and experimental profile. After this, a quick broadening of the fall-off length values is observed in all the profiles.

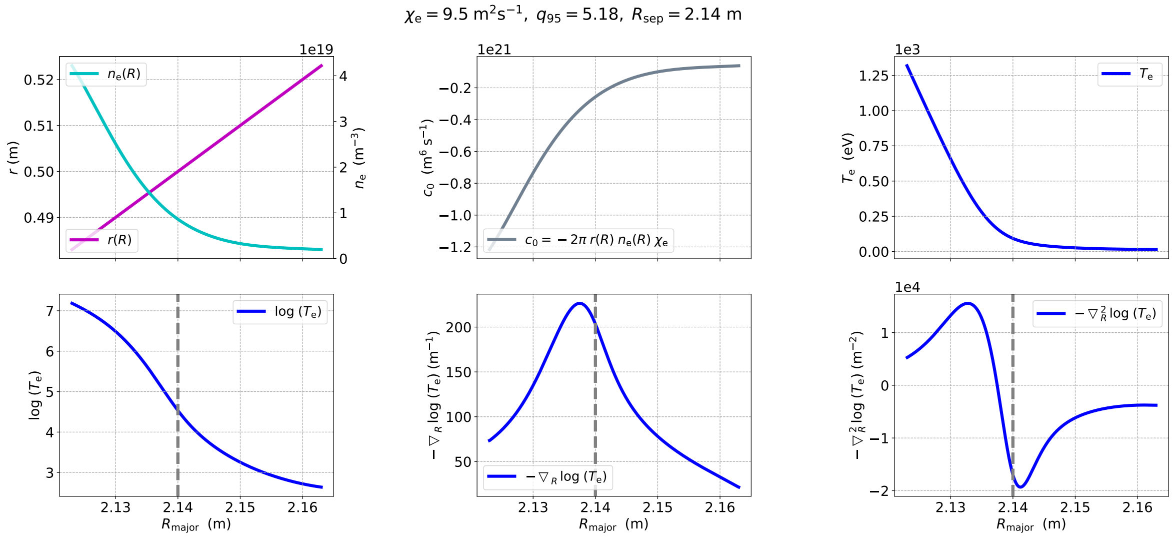

Figure 5.4.: The input parameters for the modelled H-mode example are represented including: the minor radius a in magenta, density profile n_e as a function of the major radius in cyan, the coefficient c_0 in gray. The solution of the 1.5 D modelling in natural scale, logarithmic scale and its negative derivatives are shown in blue.

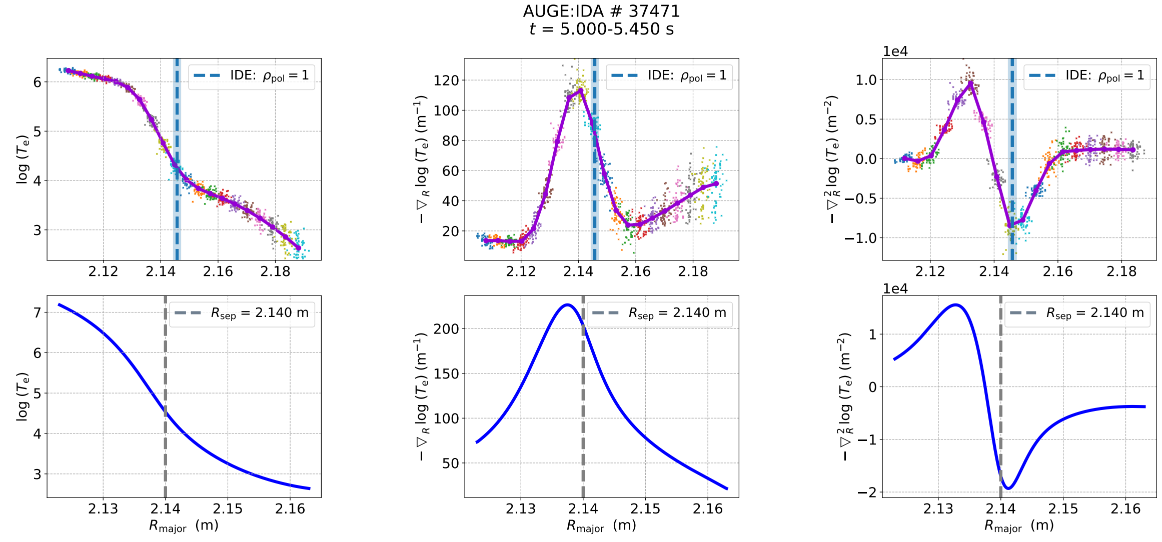

Figure 5.5.: In blue, the results from the 1.5 D modelling and its negative derivatives compared with the negative radial derivatives obtained from the experimental database (in purple for the mean values, in color for the whole time interval), in particular for # 37471 in t = 5–5.45 s. The gray vertical and dashed line denotes the separatrix position.

5.2. Modelling Comparison between H- and L-modes

In this section, the L-mode case is also modelled. The idea behind the explanation of the agreement between $R_{\mathrm{TePOS}} = R_{\mathrm{sep}}$ for H-modes and density shoulder formation discharges, and the opposite $R_{\mathrm{TeNEG}} = R_{\mathrm{sep}}$ for L-modes, is that at the separatrix, the transport changes massively and that the combination of slope at the pedestal and the slope of the near SOL profile in logarithmic scales are responsible for the different signs in the curvature of the profiles.

In particular in H-modes, the steepness of the edge transport barrier is the responsible mechanism for the matching of the separatrix position to the point of the highest positive curvature.

In case of medium and low density L-modes, there is no pedestal formation. A flatter slope in the inside of the separatrix region would be the cause for which most of L-modes follow the opposite trend as the H-modes.

In case of high density shoulder formation L-modes, there is also not an edge transport barrier but due to the fact that the near SOL profiles becomes flatter, the curvature at the separatrix result to be positive. This behaviour is illustrated fig. 5.6. There is an increase of the density decay length in the scrape-off layer (SOL) observed in many tokamaks during L-mode in a density shoulder formation discharge when a density threshold is reached. Also the temperature decay length goes broader as the overall contribution results in a positive curvature of the profiles at the separatrix [Car17] .

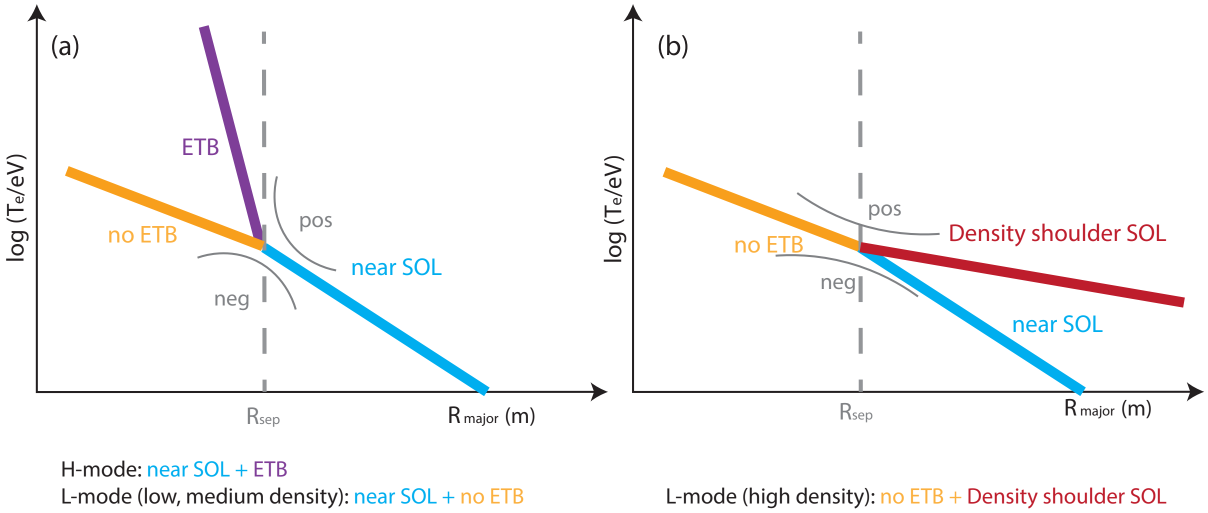

Figure 5.6.: (a) shows the H-mode case and medium-low density L-mode cases in attached regimes. (b) shows two trends for an L-mode, an attached one in blue and a density shoulder formation discharge in red. The different signs of the curvature are marked in grey.

In the following, both H- and L-mode scenarios will be modelled. The correspondent solution of of both scenarios without parallel losses to the divertor is also simulated solving eq. (5.10) with $c_1 = 0$:

$$c_1 = -\frac{\kappa_0}{L_\mathrm{c}} = 0 \Rightarrow c_0 \, T_e{}'' = 0 \tag{5.14}$$

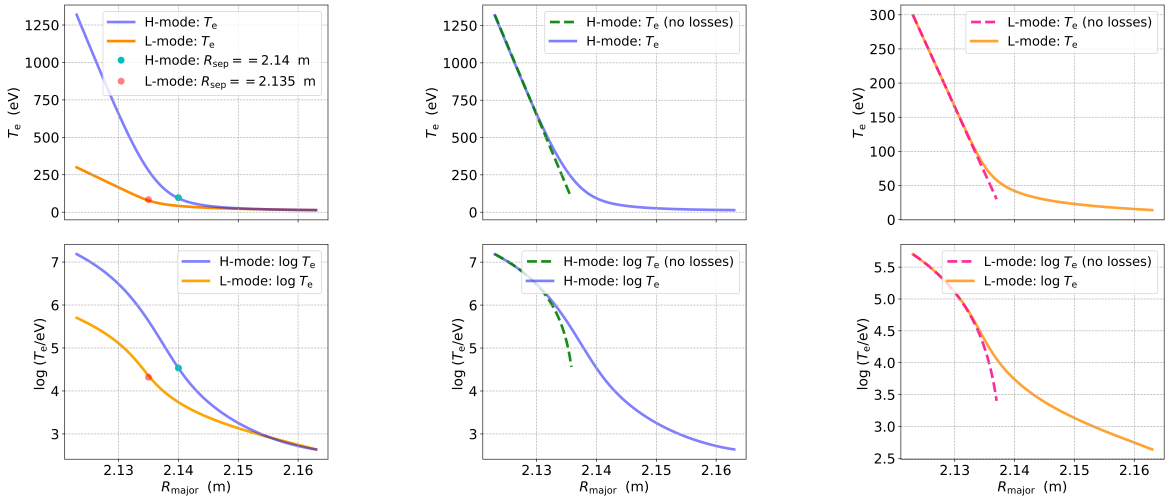

Figure 5.7.: The input parameters for the modelled medium-density L-mode example are represented including: the minor radius a in magenta, density profile n_e as a function of the major radius in cyan, the coefficient c_0 plotted in gray. In blue are shown the solution of the 1.5 D modelling in natural scale, logarithmic scale and its negative derivatives

For the modelling of an L-mode, lower initial temperature values are chosen as initial conditions in order to represent the flatter profiles due to the absence of the edge transport barrier. For the safety factor, the separatrix position values are chosen from the L-mode database (in the header of fig. 5.8). The diffusivity constant remains the same as with the H-mode case and the width factor is chosen this time as 700. In this case, the width factor needs to be higher as there is no transport barrier at the edge. Thus the magnetic field lines change more abruptly around the separatrix. For the density, a constant value of $9 \times 10^{18}\,\mathrm{m}^{-3}$ is chosen.

The derivatives of the modelled L-mode case are also calculated in fig. 5.8. It can be seen that for the second derivative case, the point of lowest negative curvature is much closer to the separatrix position as in the modelled H-mode case, although it does not match so well the separatrix position as it occurs with the H-mode case. A good reason for this It is also visible that the decay lengths are also not constant around the separatrix in the modelled profile.

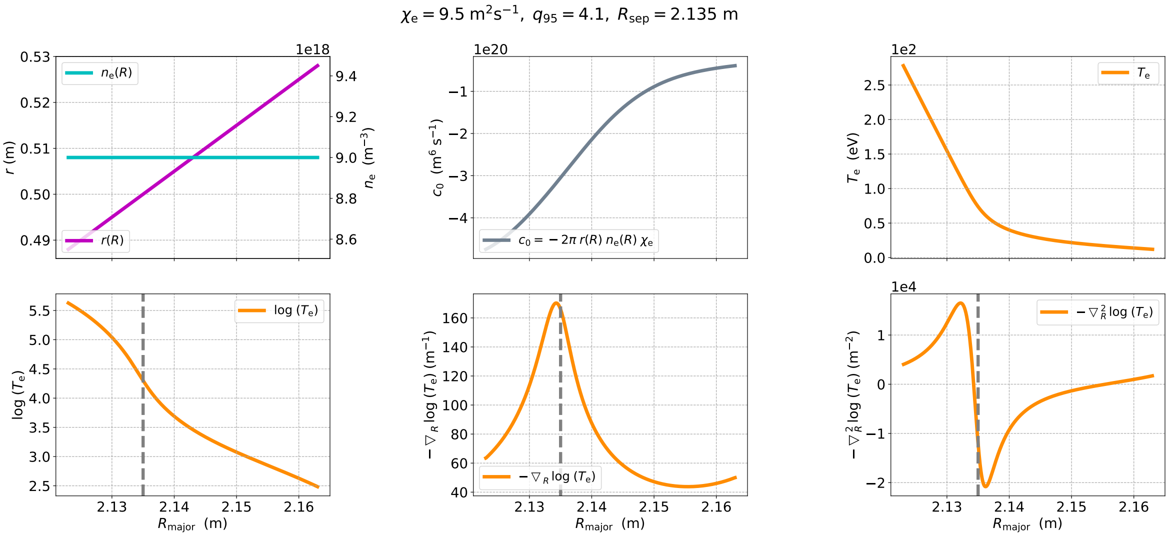

Figure 5.8.: Input parameters: minor radius, density profile, grouped under the coefficient c_0, natural scale temperature solution, logarithmic solution and its negative derivatives

5.3. L-mode Comparison with GRILLIX

In order to have better comparison for the L-mode case, a profile from the simulation code GRILLIX, as well as its derivatives are also compared with the experimental data with the thermal helium beam evaluation [Ste18].

GRILLIX is a turbulence simulation code, which studies the boundary plasma turbulence in realistic diverted configurations using EQH for the equilibria reconstruction. The most recently studies [Zho21] include the simulation of the L-mode discharge # 36 190, which is also included in the built database for this thesis. In fig. 5.9, the simulated profile and its derivatives are shown. It can be seen from the comparison between the experimental data and the simulated profile that the shape for the profiles and its derivatives fit quite well while the experimental data. It is also observed that the separatrix position obtained with GRILLIX is closed to the point of lowest negative curvature for the temperature profile. This agrees with the experimental matches described in chapter 4, where $R_{\mathrm{Te,NEG}} = R_{\mathrm{sep}}$ is seen for the conduction-limited L-mode discharges. Thus, it would be interesting to deepen the study of the curvature derivatives with data from other sources (other diagnostics and simulation profiles) to develop a method to estimate the position of the separatrix from the extrema of the curvature profiles.

From the analysis of the shape of the temperature profiles and its derivatives, it can be seen that all the different approaches (experimental data, simple modelling and the simulated discharge) agree well in a qualitative way. The fact that all these approaches show the same or a very similar shape also indicates that the fall-off lengths are not constant around the separatrix.

Table 5.1.: Mean and standard deviation for the separatrix temperature with experimental data, the simple modelling and the simulation

Temperature at R_{sep} (eV)	**H-mode discharges**	**L-mode discharges**
Experimental THB Data	80 ± 13 eV	95 ± 29 eV
Simple Modelling Data	97 eV	84 eV
Simulation Data	-	49 eV

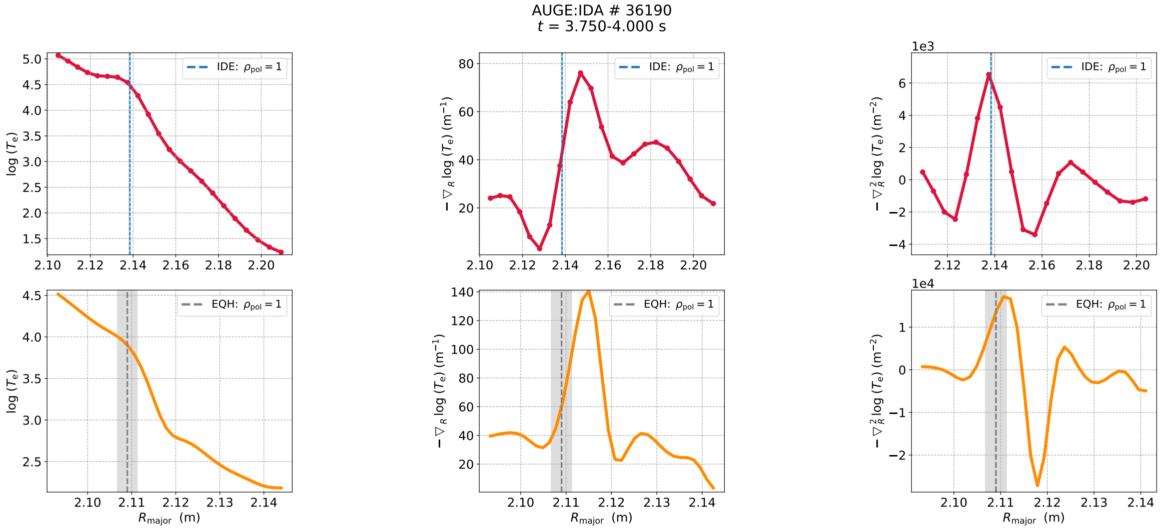

Figure 5.9.: Both experimental (in red) and with GRILLIX simulated data (in orange) and its derivatives for #36190 for the t= 3.75-4 s. The simulated profiles have higher gradient values and a narrower domain. It can also be seen that the separatrix position lies around the point of lowest negative curvature, as stated in the model developed in this chapter for low and medium L-modes. For the simulated profile the separatrix is at R_{sep}= 2.109 m while for the experimental data is at R_{sep}= 2.138 m

Finally, a comparison between the mean values for the electron temperature at the separatrix from the experimental database, the modelled discharges and reference values (50 eV±15 eV for L-modes and 100 eV±30 eV for H-modes) from power balance studies [Kal04, Neu02] is carried out. These results are included in table 5.1, where it is seen that both experimental data and modelling values agrees well, specially for the H-mode scenario.

6. Near Scrape-Off Layer Fall-Off Length Studies

In this section the methods used to calculate the near scrape-off layer gradient lengths, with both the thermal helium beam diagnostic (THB) and the edge Thomson scattering systems, are presented. For the calculations with THB data, three methods are presented, namely the across-separatrix fit, the local fit and the 1λ-averaged fit. For the TS data, a log-linear fit based in previous studies is used [Sun15, Sun17a]. Following these evaluations, different parametric dependencies of the temperature fall-off length against the plasma current, the safety factor and the heating power with both diagnostics are studied.

6.1. Near SOL Fall-Off Lengths with THB Data

Since the THB profiles are smooth, it was possible to work with the derivatives, and verify that the decay lenghts are not constant around the separatrix but vary greatly. For this reason, three different fits defined according to their radial domain are carried out.

Local Fit: This is the first fit studied where the local fall-off length value is obtained from the radial channel closest to the separatrix position. Due to the strong variation of λ_{Te} around the separatrix, a local analysis is performed using the radial channel closest to R_{sep}, defined as $R_{\mathrm{TePOS}} = R_{\mathrm{sep}}$ for H-modes and high-density L-modes, and as $R_{\mathrm{TeNEG}} = R_{\mathrm{sep}}$ for medium/low-density L-modes.

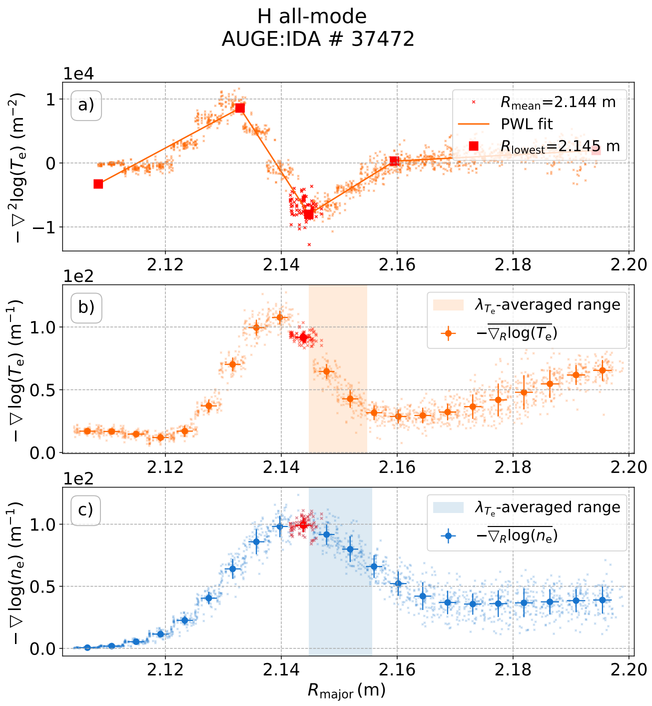

Figure 6.1.: Negative derivatives of the logarithmic data (n_e in blue and T_e in orange) to show how the separatrix (red middle square $R_{\mathrm{lowest}} = R_{\mathrm{TePOS}} = 2.145$ m) is used to choose the radial channel (in red). The shaded regions start at the position of the separatrix.

In other words, with this method, the radial channel closest to the position of the separatrix R_{sep} is calculated first in the second derivatives of the temperature profiles with respect to the logarithmic scale. This cloud of points is composed of all the temperature values corresponding to the same poloidal coordinate mapped to real space (R_{major}) for all the time points included the studied interval. To establish which radial channel corresponding to the same poloidal point in the magnetic flux grid is the closest to R_{sep}, the mean and standard deviation are computed for each of the radial channels. Then the distance from R_{sep} to the mean position of the cooresponding cloud of points is calculated, selecting the channel that minimizes this distance. This same radial channel is chosen in the profile of the first derivatives. eq. (4.3) allows to relate the value of the negative first derivative in logarithmic scale with the value of the decay length. Thus, the decay length with the local fit and its error are:

$$\lambda_{\text{Te}} \pm \Delta\lambda_{\text{Te}} \mid_{\text{local}} = 1 \cdot 10^3 \left(\frac{-1}{(\nabla_R \log T_{\text{e}})} \pm \frac{1}{(\nabla_R \log T_{\text{e}})^2} \right) \text{ [mm]} \tag{6.1}$$

1λ-averaged Fit: It is the second fit studied, based on the previous local approach. A linear fit is performed on a logarithmic scale for the temperature (or density) data points. The radial range is chosen from the separatrix position on until the position of the separatrix plus the value of the decay length from the local fit ($R_{\text{sep}} + \lambda_{\text{Te|Local}}$). In this way, the behavior of the decay length in the near SOL is analyzed in detail with this fit, assuming that the near SOL is the region where the fall-off length is constant, i.e both decay lengths for the temperature and density profiles are constant (with decay length values independent from each other) within this layer. Contrary to the local fit, the 1λ-averaged fit is suitable for identifying flattened density profiles, in which the scale length of the density gradient near main chamber surfaces ("far SOL") becomes large, as is the case for "density shoulder formation" discharges. An example of such a discharge can be seen in graph x in the appendix, where it can be seen that the difference between the local decay length and the 1λ-averaged value is much larger than for discharges of the same scenario under attached conditions. This is due to the high value of the 1λ-averaged fit for density shoulder formation discharges. For the fit, a log-linear fit using a least-squares algorithm which can be solved analytically [Lan10], is preferred over an exponential fit. For the log-linear fit, a linear function is used to fit the set of experimental points (in logarithmic scale):

$$(x_i, y_i \pm \sigma_i)\,, \quad i = 1, ...N_D \tag{6.2}$$

where y is the independent variable as a function of the dependent variable x. σ_i is the uncertainty in the ith value of y, for all N_D experimental points of the dataset. A model linear function g, which contains the dependence on x, and an dependence on the parameter set ($M_{\text{P}} = a_1, a_2, ..., a_{M_{\text{P}}}$) , is proposed to describe these data:

$$g(x) = g\left(x; \{a_1, a_2, \ldots, a_{M_P}\}\right) = g\left(x; \{a_m\}\right) \tag{6.3}$$

with $M_{\mathrm{P}} = 2$ for the linear case $(g(x; \{a_1, a_2\}) = a_1 + a_2 \cdot x)$. In the algorithm used, the initial conditions for the parameter set (initial slope and offset values for the linear function) are given. To measure how well the linear function g reproduces the experimental data, a χ^2 distribution of the sum of the squares of the independent standard deviations, is calculated:

$$\chi^2 \stackrel{\text{def}}{=} \sum_{i=1}^{N_D} \left(\frac{y_i - g\left(x_i; \{a_m\}\right)}{\sigma_i} \right)^2 \tag{6.4}$$

In this way the parameters a_1, a_2 in the theory function $g(x)$ and its errors $\sigma^2_{a_1}, \sigma^2_{a_2}$ are adjusted until a minimum in the chi-square distribution is found,

$$\frac{\partial \chi^2}{\partial a_m} = 0 \quad \Rightarrow \quad \frac{\partial g\left(x_i\right)}{\partial a_1} = 1, \quad \frac{\partial g\left(x_i\right)}{\partial a_2} = x_i \tag{6.5}$$

that is, finding a curve that produces the least value for the summed squares of the deviations of the data from the function $g(x)$. For the log-linear fit, using the expression 2.20 for the temperature case, $g(x)$ can be rewritten as:

$$g(x; \{a_1, a_2\})) = a_1 + a_2 \cdot x \quad \Rightarrow \quad \log T_{\mathrm{e}} = \log T_{\mathrm{e,sep}} + \left(\frac{-1}{\lambda_{T_{\mathrm{e}}}} \right) \cdot r \tag{6.6}$$

where r is the radial coordinate relative to the separatrix position in the SOL. The value and error for the fitted fall-off length can be derived knowing a_2 and σ_{a_2} :

$$\lambda_{\mathrm{Te}} \pm \Delta\lambda_{\mathrm{Te}} = 1 \cdot 10^3 \left(\frac{-1}{a_2} \pm \frac{\sigma_{a_2}}{(a_2)^2} \right) [\mathrm{mm}] \tag{6.7}$$

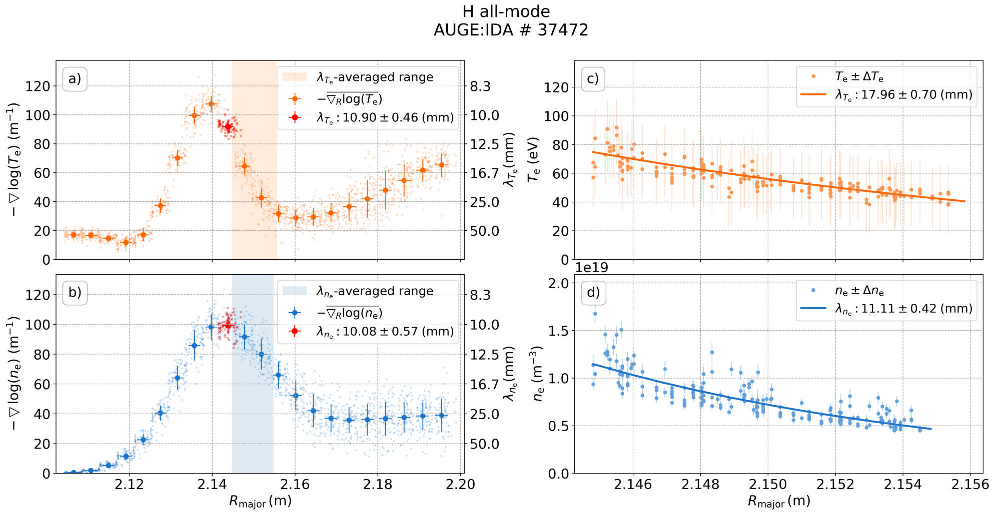

Figure 6.2.: Local fit (in red) and 1λ-averaged fits for both temperature (in orange) and density (in blue) profiles for the discharge # 37472 for the time interval $t = 4.5$-$5\,\mathrm{s}$. In the first column, the first negative derivatives in logarithmic scale are represented, and in the second column, the original data points in natural scale are plotted also showing the log linear fit in natural scale. The shaded region starts at the separatrix position.

Figure 6.2 shows both fits, the local fit is highlighted in red and the radial region for the averaged fit is shaded in the first column plots and the averaged fit illustrated in the second column.

Across-Separatrix Fit: In the last fit, the behavior of the decay length across the separatrix, i.e., from the zone of closed magnetic field lines to the nearest zone of open field lines, is studied. The radial region comprising the length of the corresponding local decay length centred on the separatrix is selected. This fit is used to test how sensitive the value of the decay length is, when the pedestal region is also included.

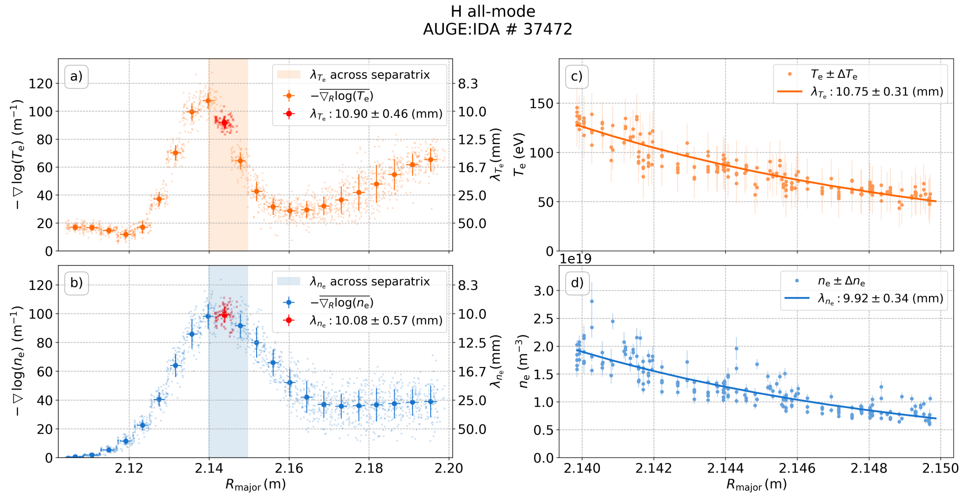

Figure 6.3.: Local (in red) and across separatrix fits for the discharge # 37472 for the time interval $t = 4.5$–5 s for both temperature (in orange) and density profiles (in blue). For the across separatrix fit a radial range of $(R_{\text{sep}} - \lambda_{\text{Te|Local}}/2, R_{\text{sep}} + \lambda_{\text{Te|Local}}/2)$, shaded in the plots in the first column, is chosen.

As it can be seen for the discharge example # 37472 showed in fig. 6.3, the difference between the values obtained from the local fit and the across separatrix do not differ much as their confidence intervals overlap. The other discharges within the built database shown in fig. 6.4 present similar results. Thus it can be concluded that both evaluations give comparable results, especially for the H-mode set. However, it can not be concluded that the decay length value inside the separatrix is the same as the one outside the separatrix. Both values differ hugely (as seen in any plot with first derivatives) but compensate each other if the fit to calculate the decay length across the separatrix is performed in a symmetrical way close enough to the separatrix. Inside the separatrix the temperature decay length is higher compared to the value in the near SOL. Therefore the exact positioning of the separatrix and the interval selected for the calculation is crucial.

6.2. Near SOL Fall-Off Length Parametric Dependencies with THB Data

The drift-based model in [Gol11], presented in chapter 4, states that the parallel heat flux width in the SOL shows a strong inverse dependence on the plasma current, with relatively weak dependencies on the other variables like the toroidal field, or the heating power. Experimental infrared measurements of the parametric dependencies of this SOL power decay length $\lambda_{q_{\|e}}$ showed a good agreement with the model [Eic11b]. In [Sun15] the scaling of the directly measured temperature fall-off lengths in the near SOL also shows the same parametric dependencies as the scaling inferred from downstream infrared measurements. This inverse relation of the SOL decay lengths with the plasma current implies a direct relation of the decay lengths with the safety factor, as q_{95} depends inversely on I_{p}:

$$q_{95} = \frac{r}{R}\frac{B_{\mathrm{t}}}{B_{\mathrm{p}}} \propto \frac{1}{I_{\mathrm{p}}} \tag{6.8}$$

This quantity is also directly proportional to the connection length (cf. eq. (2.9)). It can be seen that the longer the connection length is, the longer a magnetic field line is and thus lower is the parallel transport gradient between the SOL midplane and the divertor targets. As the decay length in the SOL can be understood as a measurement of the ratio between parallel and perpendicular transport, it can be derived that the stronger the parallel transport is, the narrower the fall-off lengths in the SOL will be:

$$\frac{1}{I_{\mathrm{p}}} \propto q_{95} \propto L_{\mathrm{c}} \propto \frac{1}{\nabla_{||}T_{\mathrm{e}}} \propto \lambda_{\mathrm{Te}} \tag{6.9}$$

At beginning of this section, the parametric dependencies of the temperature fall-off lengths measured with the thermal helium beam diagnostic are studied. In figure 6.4, the parametric dependencies for the H-mode dataset of the temperature decay lengths calculated with the three different fits (across the separatrix, local and 1λ-averaged fit) are showed. It can be seen that all the fits present an inverse dependence with the plasma current, a direct relation with the safety factor and no dependencies with the heating power. While the results of the across separatrix and local fit show very similar values, the averaged fit shows much higher temperature decay lengths. The fit with the clearest dependencies is the local fit. In figure 6.5 the same trends are found for the L-mode dataset. A local dependency study ($\lambda_{T_{\mathrm{e}}}$ against the temperature and density values at the separatrix) was also carried out using the thermal helium beam data, showing no clear trends.

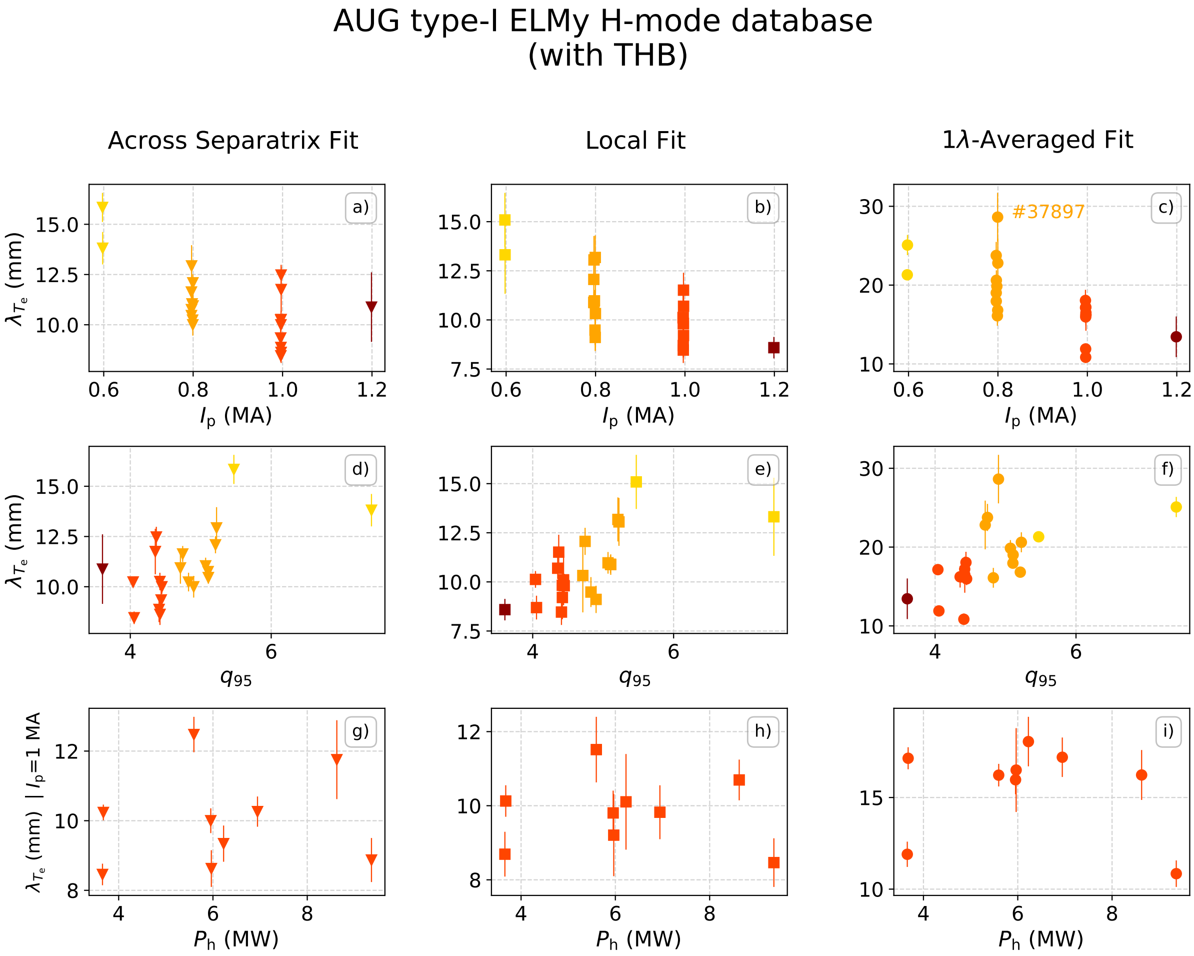

Figure 6.4.: Parametric dependencies for the H-mode database of the temperature fall-off lengths obtained with the three different methods: across separatrix fit in the first column, local fit for the second column, and 1λ-averaged fit in the third column. The figure shows the relation of the temperature fall-off length to the plasma current (inverse relation) in the first row, the safety factor (direct relation) in the second row and the heating power (no relation) for the subgroup of discharges with a I_p =1 MA in the third row.

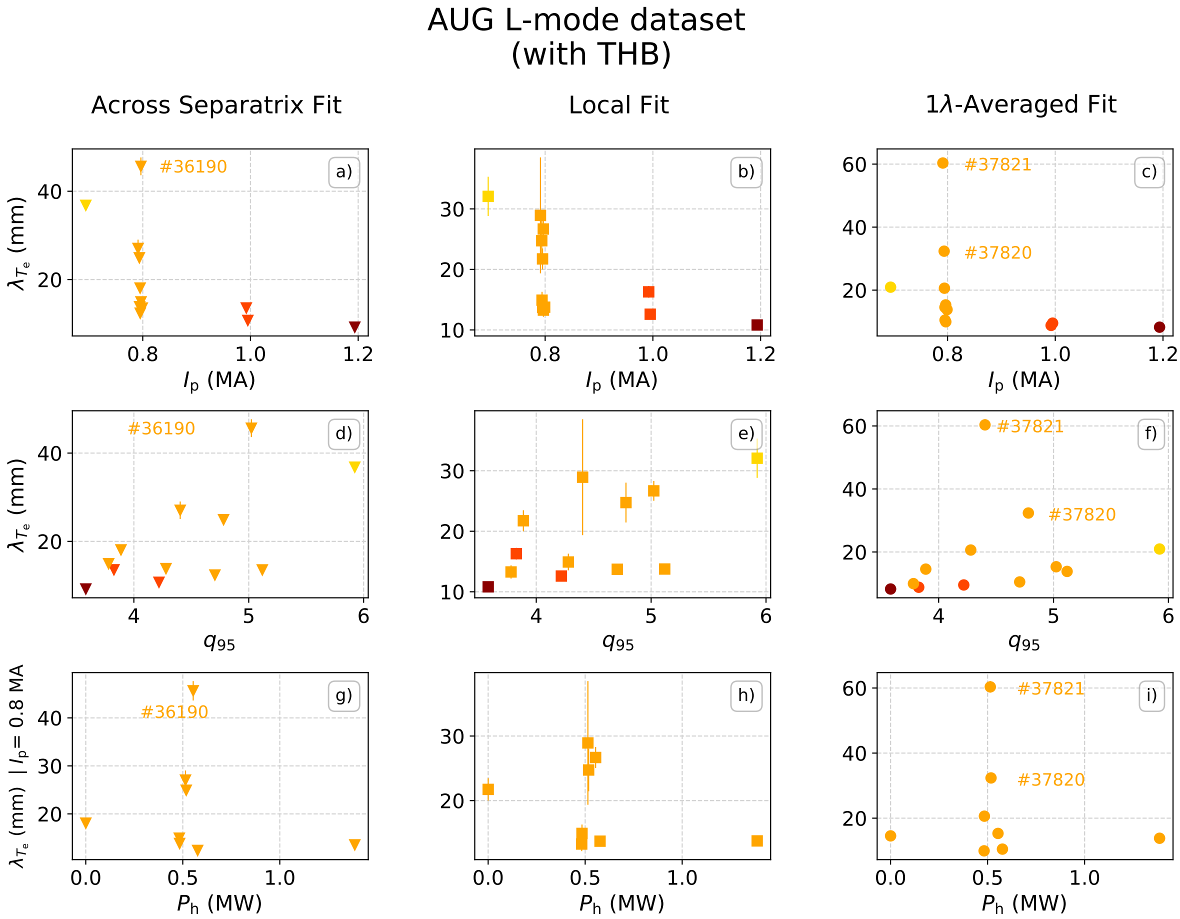

Figure 6.5.: Parametric dependencies for the L-mode database of the temperature fall-off lengths obtained with the three different methods: across separatrix fit in the first column, local fit for the second column, and 1λ-averaged fit in the third column. The figure shows the relation of the temperature fall-off length to the plasma current (inverse relation) in the first row, the safety factor (direct relation) in the second row and the heating power (no relation) for the subgroup of discharges with a I_p =0.8 MA. The density shoulder formation discharges # 37820 and # 37821 do not follow trends for the averaged fit as they are not in an attached regime as the other discharges. For the across separatrix fit, the discharge # 36190 which present the steepest gradient before the separatrix position does not follow the trend for the across separatrix fit, where the outer confined region is also included in the analysis.

6.3. Near SOL Fall-Off Length Comparison between the THB and the TS

In this section the fall-off length dependencies measured with the Thomson Scattering system at the plasma edge are presented. In order to carry out this study, the discharges are selected for analysis with the TS data from the database previously constructed for the THB evaluation. For the selection, it is checked that there is sufficient amount of reliable TS datapoints within the studied time interval. In case of the H-mode dataset, 12 discharges out of the 21 are used for the TS evaluation. For the L-mode dataset, 10 out 12 discharges are chosen.

For the gradient length calculation with TS data, a log-linear fit is carried out, based on the approach in [Sun17a][Sun15]. For this fit also the pedestal region is included and the outer most point used for the fitting is the one at which the error bars are comparable to the measured value. In order to do this, a binning grid with 3 mm of radial resolution is calculated and the mean and standard deviation for all the points within the same subsection in the grid are used to set the outer boundary.

In figure 6.6 the temperature profile read with the TS diagnostic is shown, as well as the log-linear fit carried out for the studied interval. The same analysis for the density profile can be seen in fig. 6.7.

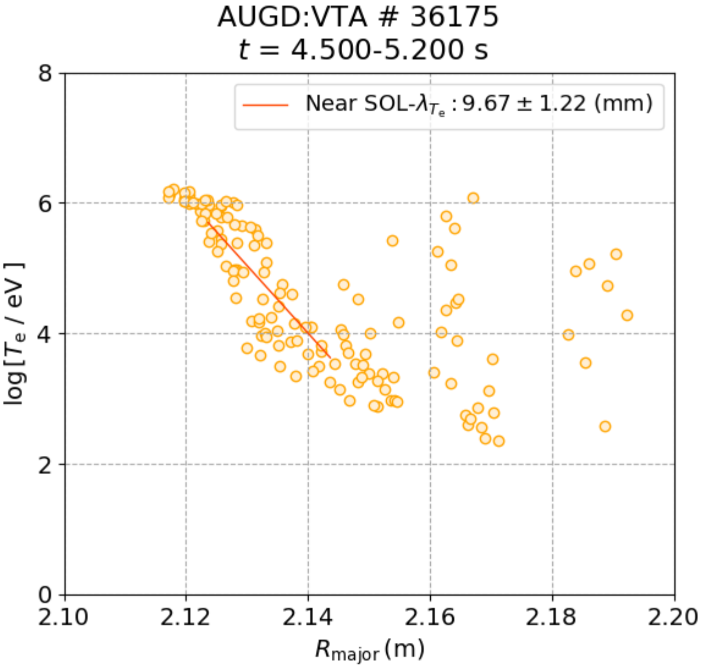

Figure 6.6.: Log-linear fit of the temperature profile for the discharge 36175 with I_p= 1 MA for the interval 4.5–5.2 s. For the ELM filtering, the data is synchronized in time relative to the onset of an ELM defined from −3.5–−1.5 ms relative to the onset time but 4 ms after the previous ELM (cf. appendix A.5

This is done for all the discharges selected for the TS evaluation and compared with the fitting approaches with THB data, the results for the H-mode dataset are shown in figure 6.8. The results for the L-mode can be found in fig. 6.9.

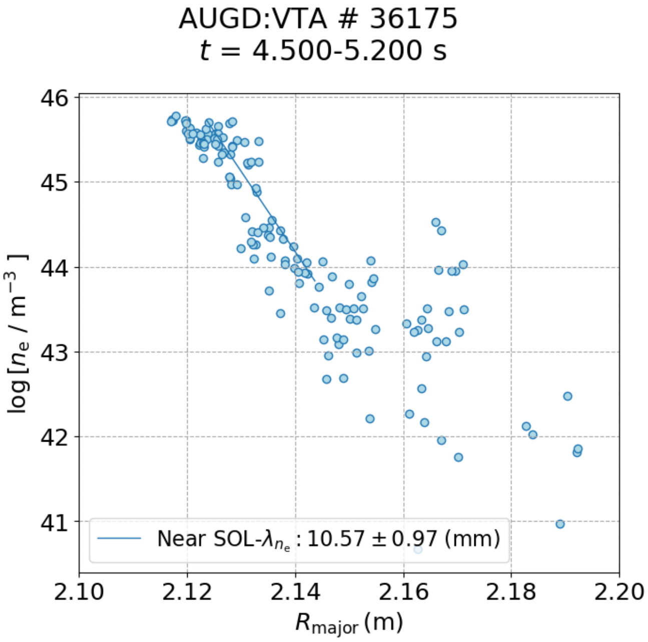

Figure 6.7.: Log-linear fit of the density profile for the H-mode discharge # 36 175 with $I_p = 1\,\mathrm{MA}$ for the interval 4.5–5.2 s. For the ELM filtering, the data is synchronized in time relative to the onset of an ELM defined from -3.5 to -1.5 ms relative to the onset time but at least 4 ms after the previous ELM.

It can be seen that all fits show the same trend between the temperature fall-off lengths and the plasma current. TS data has the narrowest values, while the averaged fit shows the widest decay length results. A quantitative comparison of the temperature and density fall-off length values obtained with TS and the three fits with THB data can be found in appendix A.6. Therefore it should be noted that the range of values obtained with the different methods is comparable and shows the same dependencies. However, the TS data are the narrowest (in agreement with the results of previous studies [Sun15, Sun17b]). This discrepancy of the absolute values could be because the studies do not comprise the same radial regions. Furthermore, the TS system presents misalignments that make it more complicated to determine the radial regions. The different equilibria codes used may also play an important role: while in TS evaluation, EQH is used (with a negligible impact), in the THB evaluation, the IDE package has been used. The agreement between the diagnostics is good, especially when the local or across separatrix fit is used. There even the absolute numbers match quite well. As expected, the averaged fit to the SOL delivers much higher values, as the temperature decay length is higher in the SOL than in the confined region.

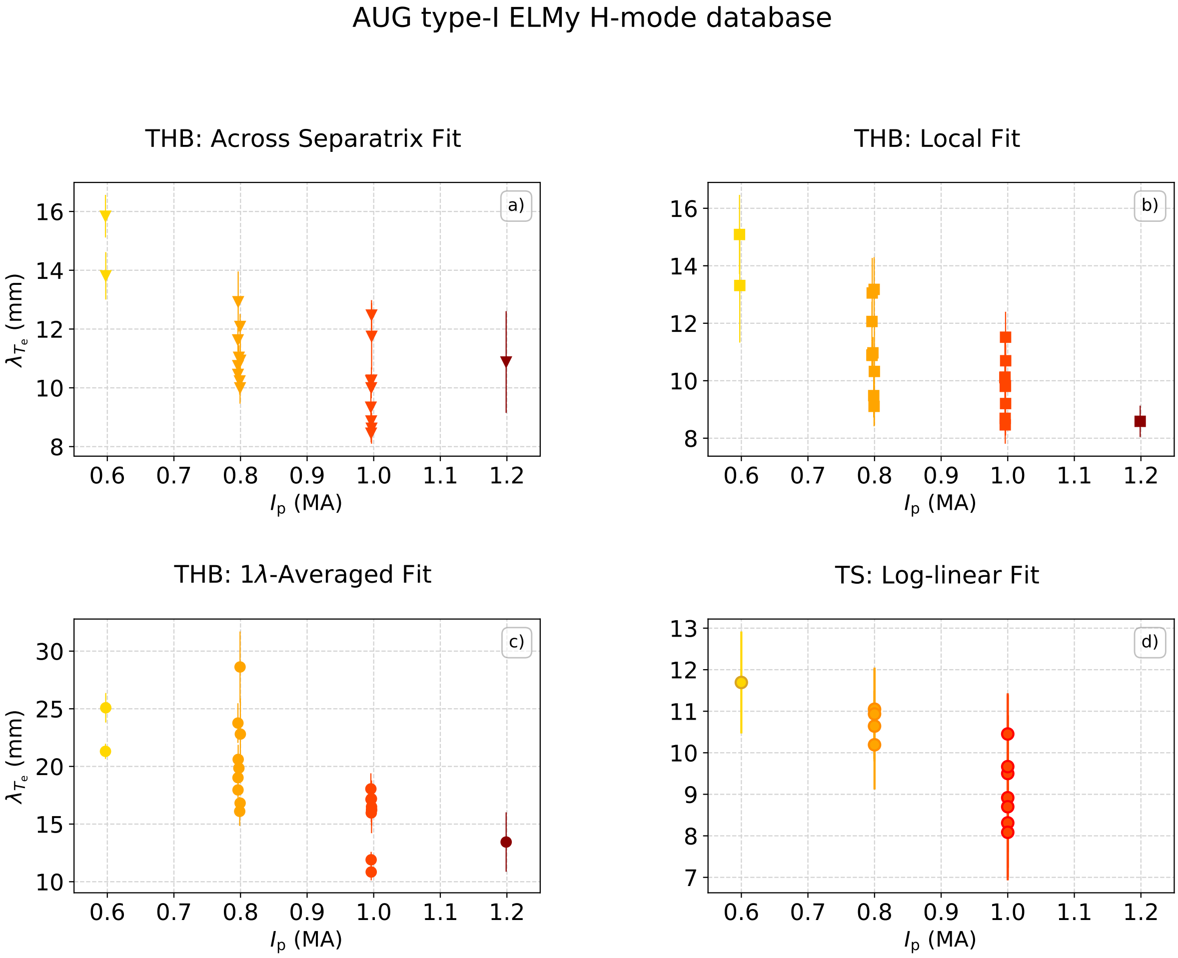

Figure 6.8.: Comparison of all the studies (THB local, across separatrix and averages fit) and the TS log-linear fit of the temperature fall-off lengths against the plasma current for the H-mode data set.

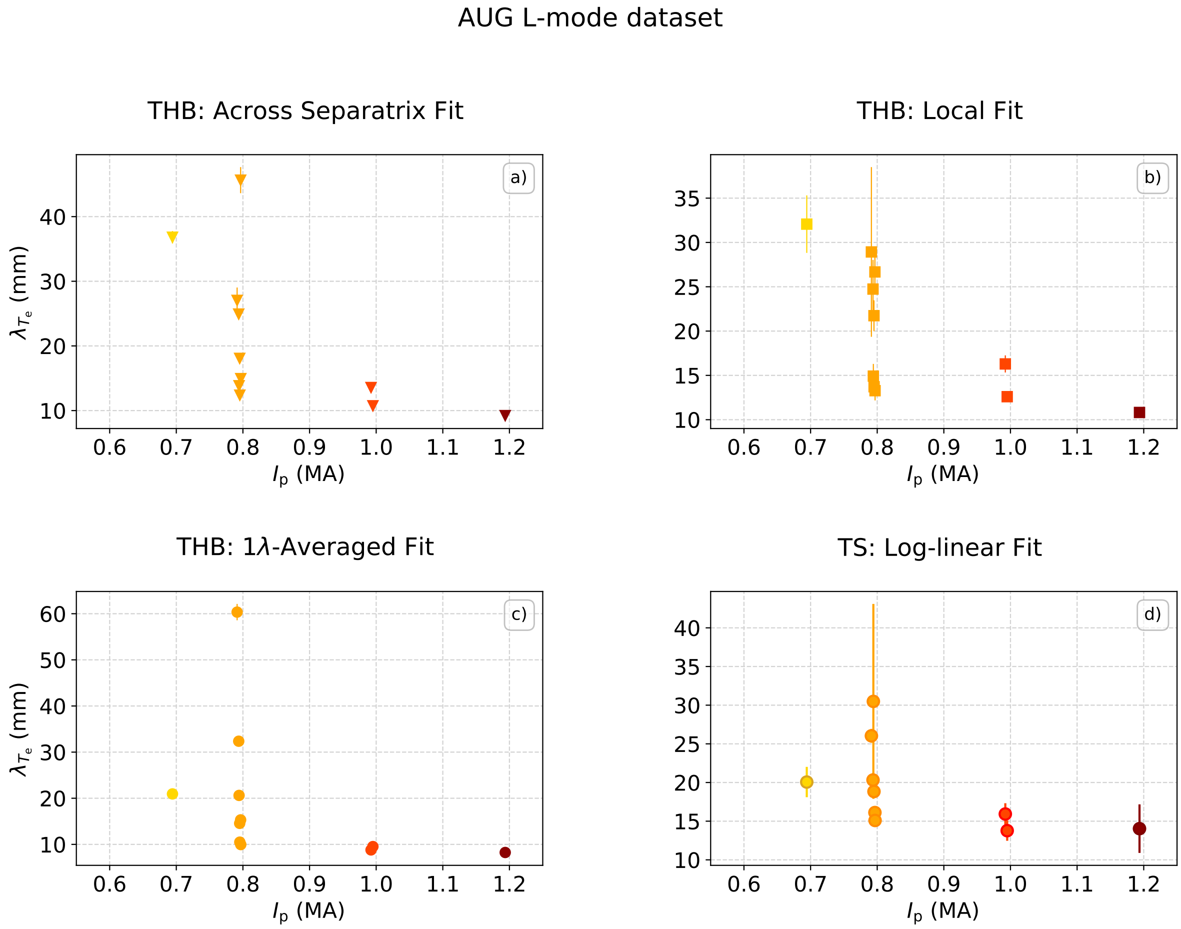

Figure 6.9.: Comparison of all the studies (THB local, across separatrix and averages fit) and the TS log-linear fit of the temperature fall-off lengths against the plasma current for the L-mode data set. The outliers seen in the subplots (a), (c) and (d) with a plasma current of 0.8 MA corresponds to the discharges performed in the linear regime (density shoulder formation studies).

7.Summary and Conclusions

The aim of this thesis is to study the structure of electron temperature profiles and to investigate the near SOL temperature fall-off lengths measured by the thermal helium beam (THB) diagnostic and compare them with the already established Thomson scattering (TS) system at AUG. In order to do this, a database of attached H- and L-modes in the high conducting regime but also linear regime under steady-state conditions is built. As a first step, it has been assumed that the near scrape-off layer is defined for each variable in an independent way ($q_{\|\mathrm{e}}$, n_e, T_e) as the region from the separatrix on where its corresponding fall-off length (namely $\lambda_{q_{\|\mathrm{e}}}$, λ_{n_e}, λ_{T_e}) is kept constant.

From the analysis of the first derivatives of the measured radial plasma profiles, from which the fall-off lengths can be directly read, it is seen that the decay lengths for both temperature and density are not constant but vary hugely around the separatrix due to the transport changes in this region. The second derivatives show a match for the complete H-mode dataset and high-density L-modes between the point of highest positive curvature in the temperature profiles and the position of the separatrix, given by the magnetic reconstruction code IDE. For low and medium-density L-mode discharges, the match is observed between R_sep and the point of lowest negative curvature. Thus a self-consistent connection between the extrema of the profile curvature and the relative position of the separatrix is observed with the THB evaluation.

In order to explain the physical mechanisms of these experimental findings, a modelling of the heat balance equation for the region from closed to open field lines is implemented. A simplified 1.5 D geometry with a full perpendicular description and an assumption-limited description for the parallel coordinate has been used in this model. This model solves the perpendicular heat conduction, treating parallel losses through a sink term describing the parallel heat losses to the divertor. They can be understood by considering that the negative radial gradients of the temperature are proportional to the radial heat flux, and this is reduced going outwards due to the parallel losses. This 1.5 D equation is solved for an attached H-mode case by including a set of parameters based on the experimental H-mode database values. The shape of the solution profile and its derivatives agrees with the experimental data. It is also observed that the chosen separatrix position, given as an input parameter, matches the point of highest positive curvature in the temperature profile. Thus it can be seen that these two transport terms (across and along the field lines) are enough to model the transport mechanisms across the separatrix. The same procedure is applied to model a medium-density L-mode discharge by modifying the parameters set using values from the experimental dataset. For this regime, the experimental profile and its derivatives are also compared with the profile obtained from the turbulence simulation code GRILLIX. It has also been observed that the shape fits well to the corresponding experimental data, which shows that it is possible to obtain the position of the separatrix within the studied profile from the point of highest or lowest curvature for smooth profiles.

The working hypothesis for these agreements between the maximum or minimum of the curvature profile and the position of the separatrix is that the transport changes massively around the separatrix and that the combination of slope at the pedestal and the slope of the near SOL profile are responsible for the different signs in the curvature of the profiles. In particular, in H-modes, the steepness of the edge transport barrier is the responsible mechanism for the matching between the separatrix position and the point of the highest positive curvature. In the case of medium and low-density L-modes, there is no pedestal formation. This implies a flatter slope inside of the separatrix region. The separatrix position (in opposition to the H-mode case) matches the point of lowest negative curvature. In the case of high-density shoulder formation L-modes, there is no edge transport barrier. However, because the near SOL profiles become flatter, the curvature at the separatrix is positive, as in the H-mode case.

A study of the near SOL decay lengths with the THB was also carried out. As the fall-off length was proved not to be constant around the separatrix, three different fits comprising different radial regions have been implemented: the local fit (including only the radial channel closest to the separatrix position), the across-separatrix fit (from R_{sep} -$\lambda/2$ to R_{sep} + $\lambda/2$) and the 1-λ-averaged fit (from R_{sep} to $R_{\text{sep}}+\lambda$). All the fits follow the Goldston scaling, showing an inverse dependence with the plasma current and no dependence with the heating power. Both, across-separatrix fit and local fit, have similar values, while the averaged fit shows broader values as the fall-off length broadens quickly after crossing the separatrix. The comparison with TS data presents comparable results with the local and across-separatrix fits. Thus it can be stated that in case the studied radial regions overlap, similar THB and TS fall-off length values are obtained.

As outlook, the simple modelling presented in this work could be established as a method to determine the position of the separatrix from the curvature of the electron temperature profiles. It would also be interesting to study the relationship of heat and particle transport mechanisms for H-mode and L-mode cases. Discharges under detached conditions and other convective-predominant plasma scenarios could be included in the study. Smooth profiles from other machines could also be used to test this model. A new convention for the definition of the near SOL would be needed, as in this work it was proved that the temperature and density fall-off length is not constant in a broad SOL region.

Bibliography

[Arf84] G. B. Arfken, D. F. Griffing, D. C. Kelly, et al. chapter 23 - HEAT TRANSFER. In *International Edition University Physics*, pages 430–443. Academic Press, 1984. URL http://dx.doi.org/https://doi.org/10.1016/B978-0-12-059858-8.50028-5.

[Aym02] R. Aymar, P. Barabaschi, and Y. Shimomura. The ITER design. *Plasma Physics and Controlled Fusion*, 44(5):304, 2002. URL http://dx.doi.org/10.1088/0741-3335/44/5/304.

[Bai21] G. Bailey, O. Vilkhivskaya, and M. Gilbert. Waste expectations of fusion steels under current waste repository criteria. *Nuclear Fusion*, 61(3):036010, 2021. URL http://dx.doi.org/10.1088/1741-4326/abc933.

[Boz13] S. Bozhenkov, J. Geiger, M. Grahl, et al. Service oriented architecture for scientific analysis at W7-X. An example of a field line tracer. *Fusion Engineering and Design*, 88(11):2997–3006, 2013. URL http://dx.doi.org/https://doi.org/10.1016/j.fusengdes.2013.07.003.

[Bre90] G. L. Bretthorst. *An Introduction to Parameter Estimation Using Bayesian Probability Theory. In: Fougère P.F. (eds) Maximum Entropy and Bayesian Methods.* Fundamental Theories of Physics, vol 39. Springer, Dordrecht, 1990. URL https://doi.org/10.1007/978-94-009-0683-9_5.

[Car17] D. Carralero, J. Madsen, S. Artene, et al. A study on the density shoulder formation in the SOL of H-mode plasmas. *Nuclear Materials and Energy*, 12:1189–1193, 2017. URL http://dx.doi.org/https://doi.org/10.1016/j.nme.2016.11.016. Proceedings of the 22nd International Conference on Plasma Surface Interactions 2016, 22nd PSI.

[Cav16] M. Cavedon. *The role of the radial electric field in the development of the edge transport barrier in the ASDEX Upgrade tokamak.* Dissertation, Technical University Munich, 2016.

[Coo89] N. D. Cook. Computing nuclear properties in the fcc model. *Computers in Physics3*, 73, 1989. URL http://dx.doi.org/https://doi.org/10.1063/1.168319.

[Cos16] A. Costley. On the fusion triple product and fusion power gain of tokamak pilot plants and reactors. *Nuclear Fusion*, 56(6):066003, 2016. URL http://dx.doi.org/10.1088/0029-5515/56/6/066003.

[Eic11a] T. Eich, B. Sieglin, A. Scarabosio, et al. Inter-ELM Power Decay Length for JET and ASDEX Upgrade: Measurement and Comparison with Heuristic Drift-Based Model.

Phys. Rev. Lett., 107:215001, 2011. URL http://dx.doi.org/10.1103/PhysRevLett.107.215001.

[Eic11b] T. Eich, B. Sieglin, A. Scarabosio, et al. Inter-ELM Power Decay Length for JET and ASDEX Upgrade: Measurement and Comparison with Heuristic Drift-Based Model. *Phys. Rev. Lett.*, 107:215001, 2011. URL http://dx.doi.org/10.1103/PhysRevLett.107.215001.

[Eic13] T. Eich, A. Leonard, R. Pitts, et al. Scaling of the tokamak near the scrape-off layer H-mode power width and implications for ITER. *Nuclear Fusion*, 53(9):093031, 2013. URL http://dx.doi.org/10.1088/0029-5515/53/9/093031.

[Fis10] R. Fischer, C. J. Fuchs, B. Kurzan, et al. Integrated Data Analysis of Profile Diagnostics at ASDEX Upgrade. *Fusion Science and Technology*, 58(2):675–684, 2010. URL http://dx.doi.org/10.13182/FST10-110.

[Fis16] R. Fischer, A. Bock, M. Dunne, et al. Coupling of the Flux Diffusion Equation with the Equilibrium Reconstruction at ASDEX Upgrade. *Fusion Science and Technology*, 69(2):526–536, 2016. URL http://dx.doi.org/10.13182/FST15-185.

[Gol11] R. Goldston. Heuristic drift-based model of the power scrape-off width in low-gas-puff H-mode tokamaks. *Nuclear Fusion*, 52(1):013009, 2011. URL http://dx.doi.org/10.1088/0029-5515/52/1/013009.

[Gri18] M. Griener, E. Wolfrum, M. Cavedon, et al. Helium line ratio spectroscopy for high spatiotemporal resolution plasma edge profile measurements at ASDEX Upgrade (invited). *Review of Scientific Instruments*, 89(10):10D102, 2018. URL http://dx.doi.org/10.1063/1.5034446.

[Gri20] M. Griener, E. Wolfrum, G. Birkenmeier, et al. Continuous observation of filaments from the confined region to the far scrape-off layer. *Nuclear Materials and Energy*, 25:100854, 2020. URL http://dx.doi.org/10.1016/j.nme.2020.100854.

[Her02] A. Herrmann. Overview on stationary and transient divertor heat loads. *Plasma Physics and Controlled Fusion*, 44(6):883, 2002. URL http://stacks.iop.org/0741-3335/44/i=6/a=318.

[Hos19] M. Hosner. Power Fall-Off Length Dependence on the Ion/Electron Temperature Ratio at the Plasma Edge in ASDEX Upgrade. *MSc Thesis, TUM*, 2019.

[Hut02] I. H. Hutchinson. *Principles of Plasma Diagnostics*. Cambridge University Press, 2002. URL https://doi.org/10.1017/CBO9780511613630.

[Isa10] Isabella Milch (Red.). *50 Jahre Max-Planck-Institut für Plasmaphysik : Forschung für die Energie der Zukunft*. Max-Planck-Institut für Plasmaphysik (IPP), Garching/ Greifswald, 2010. URL `https://www.ipp.mpg.de/ippcms/de/pr/publikationen/buecher/festschrift`.

[Kal04] A. Kallenbach, Y. Andrew, M. Beurskens, et al. EDGE2D modelling of edge profiles obtained in JET diagnostic optimized configuration. *Plasma Physics and Controlled Fusion*, 46(3):431–446, 2004. URL `http://dx.doi.org/10.1088/0741-3335/46/3/001`.

[Kei82] M. Keilhacker, K. Lackner, K. Behringer, et al. Plasma Boundary Layer in Limiter and Divertor Tokamaks. *Physica Scripta*, T2B:443–453, 1982. URL `http://dx.doi.org/10.1088/0031-8949/1982/t2b/022`.

[Kir14] A. Kirk, D. Dunai, M. Dunne, et al. Recent progress in understanding the processes underlying the triggering of and energy loss associated with type I ELMs. *Nuclear Fusion*, 54(11):114012, 2014. URL `http://dx.doi.org/10.1088/0029-5515/54/11/114012`.

[Kno19] M. Knolker, T. Evans, A. Wingen, et al. Observation of divertor currents during type-I ELMs on the DIII-D tokamak. *Nuclear Materials and Energy*, 18:222–226, 2019. URL `http://dx.doi.org/https://doi.org/10.1016/j.nme.2019.01.003`.

[Kon17] S. Konishi, M. Enoeda, M. Nakamichi, et al. Functional materials for breeding blankets—status and developments. *Nuclear Fusion*, 57(9):092014, 2017. URL `http://dx.doi.org/10.1088/1741-4326/aa7e4e`.

[Kur11] B. Kurzan and H. D. Murmann. Edge and core Thomson scattering systems and their calibration on the ASDEX Upgrade tokamak. *Review of Scientific Instruments*, 82(10), 2011. URL `http://dx.doi.org/http://dx.doi.org/10.1063/1.3643771`.

[Lan10] R. Landau, M. J. Paez, and C. Bodeianu. *A Survey of Computational Physics*. PRINCETON UNIVERSITY PRESS AND OXFORD, 2010. URL `https://www.uio.no/studier/emner/matnat/fys/FYS3150/h14/undervisningsmateriale/Lecture%20Notes/Landau.pdf`.

[Loa07] A. Loarte, B. Lipschultz, A. Kukushkin, et al. Chapter 4: Power and particle control. *Nuclear Fusion*, 47(6):S203–S263, 2007. URL `http://dx.doi.org/10.1088/0029-5515/47/6/s04`.

[Man18] P. Manz. The microscopic picture of plasma edge turbulence. Habilitation Thesis. 2018.

[Man20] P. Manz, C. Hufnagel, A. Zito, et al. The diffusion limit of ballistic transport in the scrape-off layer. *Physics of Plasmas*, 27(2):022506, 2020. URL `http://dx.doi.org/10.1063/1.5133839`.

[Mey19] H. Meyer, C. Angioni, C. Albert, et al. Overview of physics studies on ASDEX Upgrade. *Nuclear Fusion*, 59(11):112014, 2019. URL `http://dx.doi.org/10.1088/1741-4326/ab18b8`.

[Miy05] *Tokamaks*, pages 269–317. Springer Berlin Heidelberg, Berlin, Heidelberg, 2005. URL http://dx.doi.org/10.1007/3-540-28097-9_16.

[NAT15] U. NATIONS. The Paris Agreement. 2015. URL https://unfccc.int/process-and-meetings/the-paris-agreement/the-paris-agreement.

[Neu02] J. Neuhauser, D. Coster, H. U. Fahrbach, et al. Transport into and across the scrape-off layer in the ASDEX Upgrade divertor tokamak. *Plasma Physics and Controlled Fusion*, 44(6):855–869, 2002. URL http://dx.doi.org/10.1088/0741-3335/44/6/316.

[Nil20] D. Nille. 2020. URL https://gitlab.mpcdf.mpg.de/dnille/pwl_fit.

[Pit97] C. S. Pitcher and P. C. Stangeby. Experimental divertor physics. *Plasma Physics and Controlled Fusion*, 39(6):779–930, 1997. URL http://dx.doi.org/10.1088/0741-3335/39/6/001.

[Pou17] S. Pourshahian. Mass Defect from Nuclear Physics to Mass Spectral Analysis. *Journal of The American Society for Mass Spectrometry*, 28, 2017. URL http://dx.doi.org/https://doi.org/10.1007/s13361-017-1741-9.

[Pî12] C. Pîrlogea. The Human Development Relies on Energy. Panel Data Evidence. *Procedia Economics and Finance*, 3:496 – 501, 2012. URL http://dx.doi.org/https://doi.org/10.1016/S2212-5671(12)00186-4. International Conference Emerging Markets Queries in Finance and Business, Petru Maior University of Tîrgu-Mures, ROMANIA, October 24th - 27th, 2012.

[San20] S. Sandri, G. M. Contessa, M. D'arienzo, et al. A Review of Radioactive Wastes Production and Potential Environmental Releases at Experimental Nuclear Fusion Facilities. *Environments*, 7:6, 2020. URL http://dx.doi.org/10.3390/environments7010006.

[Sen08] F. Sensfuß, M. Ragwitz, and M. Genoese. The merit-order effect: A detailed analysis of the price effect of renewable electricity generation on spot market prices in Germany. *Energy Policy*, 36(8):3086–3094, 2008. URL http://dx.doi.org/https://doi.org/10.1016/j.enpol.2008.03.035.

[Sin17] P. Sinha, H. Hölbe, T. Pedersen, et al. Numerical studies of scrape-off layer connection length in Wendelstein7-X. *Nuclear Fusion*, 58(1):016027, 2017. URL http://dx.doi.org/10.1088/1741-4326/aa9496.

[Sny04] P. Snyder, H. Wilson, J. Ferron, et al. ELMs and constraints on the H-mode pedestal: peeling–ballooning stability calculation and comparison with experiment. *Nuclear Fusion*, 44(2):320–328, 2004. URL http://dx.doi.org/10.1088/0029-5515/44/2/014.

[Spi53] L. Spitzer and R. Härm. Transport Phenomena in a Completely Ionized Gas. *Phys. Rev.*, 89:977–981, 1953. URL http://dx.doi.org/10.1103/PhysRev.89.977.

[Sta10] P. Stangeby, J. Canik, and D. Whyte. The relation between upstream density and temperature widths in the scrape-off layer and the power width in an attached divertor. *Nuclear Fusion*, 50(12):125003, 2010. URL `http://dx.doi.org/10.1088/0029-5515/50/12/125003`.

[Ste18] A. Stegmeir, D. Coster, A. Ross, et al. GRILLIX: a 3D turbulence code based on the flux-coordinate independent approach. *Plasma Physics and Controlled Fusion*, 60(3):035005, 2018. URL `http://dx.doi.org/10.1088/1361-6587/aaa373`.

[Str11] U. Stroth. *Plasmaphysik: Phänomene, Grundlagen, Anwendungen*. Vieweg+Teubner Verlag, Wiesbaden, 2011. URL `https://www.springer.com/de/book/9783834883261`.

[Sun15] H. J. Sun, E. Wolfrum, T. Eich, et al. Study of near scrape-off layer (SOL) temperature and density gradient lengths with Thomson scattering. *Plasma Physics and Controlled Fusion*, 57(12):125011, 2015. URL `http://stacks.iop.org/0741-3335/57/i=12/a=125011`.

[Sun17a] H. J. Sun, E. Wolfrum, B. Kurzan, et al. Study of near SOL decay lengths in ASDEX Upgrade under attached and detached divertor conditions. *Plasma Physics and Controlled Fusion*, 59(10):105010, 2017. URL `http://dx.doi.org/10.1088/1361-6587/aa7777`.

[Sun17b] H. J. Sun, E. Wolfrum, B. Kurzan, et al. Study of near SOL decay lengths in ASDEX Upgrade under attached and detached divertor conditions. *Plasma Physics and Controlled Fusion*, 59(10):105010, 2017. URL `http://dx.doi.org/10.1088/1361-6587/aa7777`.

[Tay] C. Taylor. Finite Difference Coefficients Calculator. URL `https://web.media.mit.edu/~crtaylor/calculator.html`.

[Tsa20] J. Tsao, N. Lewis, and G. Crabtree. Solar FAQs . 2020. URL `https://www.sandia.gov/~jytsao/SolarFAQs.pdf`.

[UN19] D. o. E. United Nations and P. D. Social Affairs. 2019 Revision of World Population Prospects. *World Population Prospects 2019: Highlights (ST/ESA/SER.A/423)*, 2019. URL `https://population.un.org/wpp/Publications/Files/WPP2019_Highlights.pdf`.

[Wag82] F. Wagner, G. Becker, K. Behringer, et al. Regime of Improved Confinement and High Beta in Neutral-Beam-Heated Divertor Discharges of the ASDEX Tokamak. *Phys. Rev. Lett.*, 49(19):1408–1412, 1982. URL `http://dx.doi.org/10.1103/PhysRevLett.49.1408`.

[Wen21] D. Wendler, R. Dux, R. Fischer, et al. New collisional radiative model for the evaluation of the Thermal Helium Beam Diagnostic at ASDEX Upgrade. *not submitted yet*, (planed) 2021.

[Wes05] J. Wesson. Tokamaks 3rd Edition. *Journal of Plasma Physics*, 71:377–377, 2005. URL `http://dx.doi.org/10.1017/S0022377804003058`.

[Zho21] W. Zholobenko, T. Body, P. Manz, et al. Electric field and turbulence in global Braginskii simulations across the ASDEX Upgrade edge and scrape-off layer. *Plasma Physics and Controlled Fusion*, 63(3):034001, 2021. URL `http://dx.doi.org/10.1088/1361-6587/abd97e`.

[Zoh96] H. Zohm. Edge localized modes (ELMs). *Plasma Physics and Controlled Fusion*, 38(2):105–128, 1996. URL `http://dx.doi.org/10.1088/0741-3335/38/2/001`.

A. Appendix

A.1. ELM Synchronization (THB)

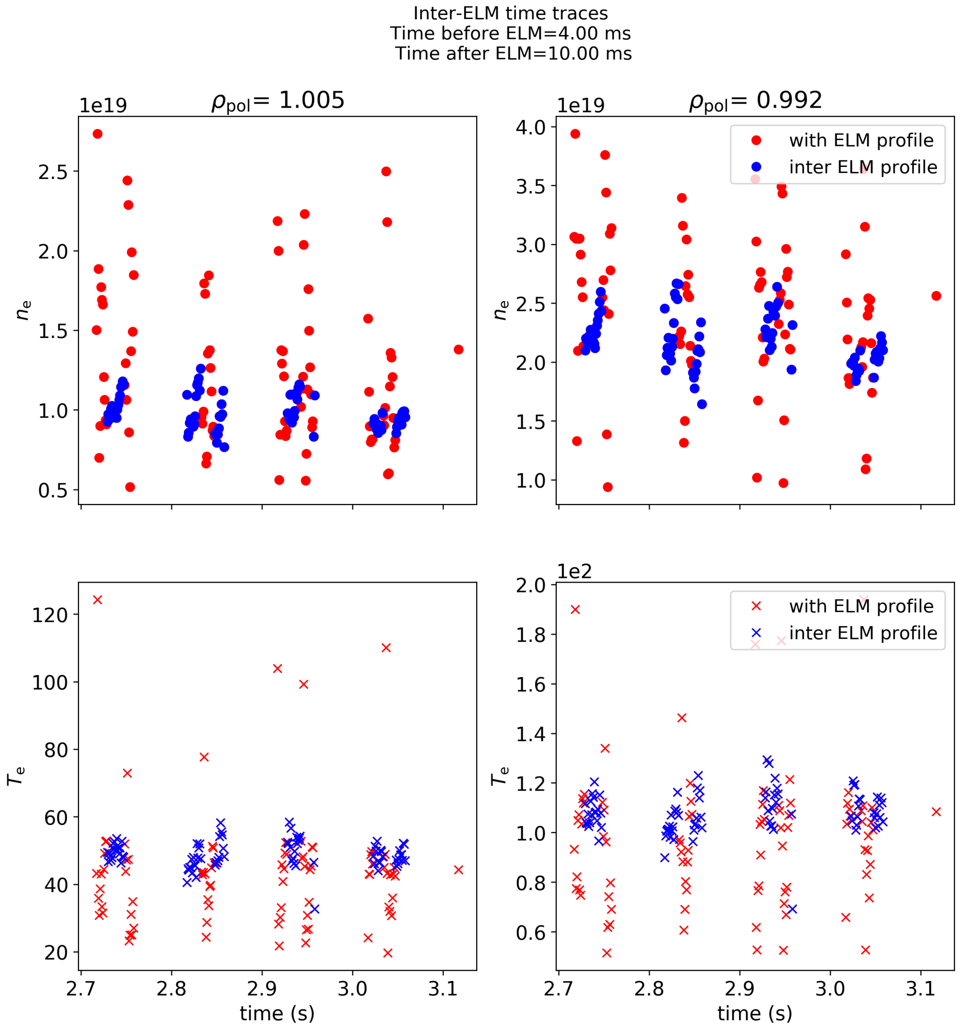

Figure A.1.: ELM synchronization for a type-I-ELMy H-mode discharge #36 300 for the time interval $t = 2.7$–3.1 s using Boolean masking to separate the time trace signal in data with and without ELMs taking into the account the recovery time for an ELM (t_{afterELM} and the shift time between the signal in the divertor and the midplane, to where the diagnostics are mapped ($t_{\mathrm{beforeELM}}$). The first rows show the density time trace for two different magnetic flux surfaces. The second rows show the temperature time traces. The phases with ELMs are shown in red and the inter-ELM phases in blue.

A.2. Curvature Profiles (L-mode)

The different morphologies found in the L-mode database for the structure of the electron temperature and density curvature profiles are shown in the following:

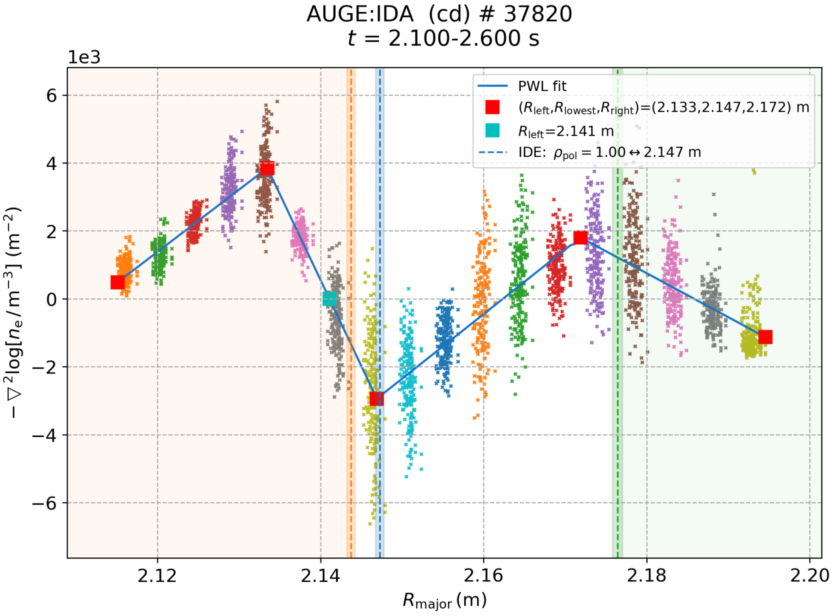

Figure A.2.: Density curvature profile for the L-mode discharge #37 820 for the time interval $t = 2.1$–$2.6\,\mathrm{s}$ showing the match between the position of the separatrix and the point of highest positive curvature: $R_{\mathrm{sep}} = R_{\mathrm{Ne,POS}}$

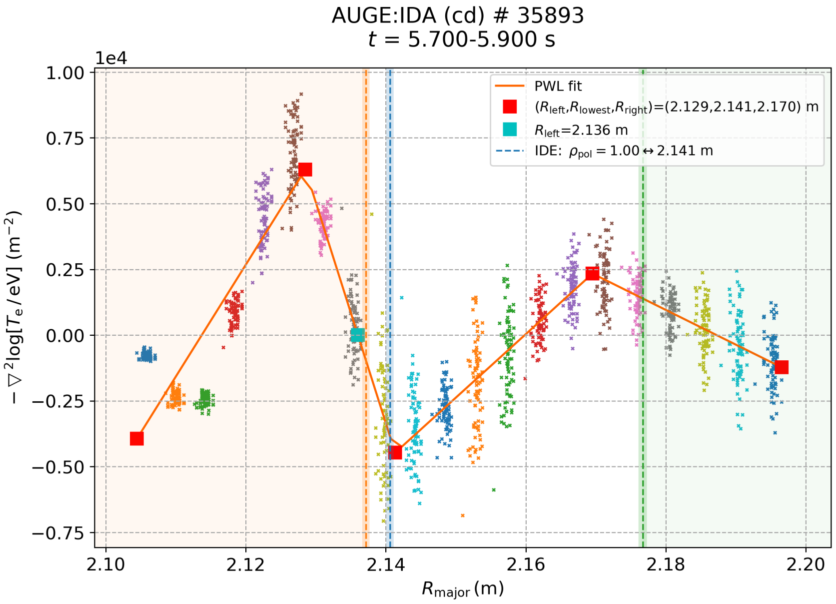

Figure A.3.: Temperature curvature profile for the L-mode discharge #35 893 for the time interval $t = 5.7$–$5.9\,\mathrm{s}$ showing the match between the position of the separatrix and the point of highest positive curvature: $R_{\mathrm{sep}} = R_{\mathrm{Te,POS}}$

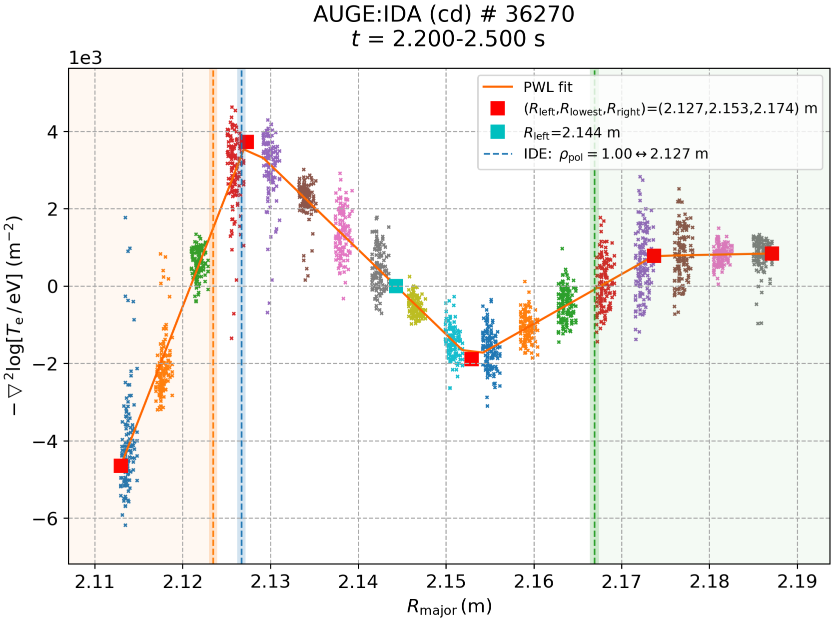

Figure A.4.: Temperature curvature profile for the L-mode discharge #36 270 for the time interval $t = 2.2$–2.5 s showing the match between the position of the separatrix and the point of highest positive curvature: $R_{\text{sep}} = R_{\text{Te,NEG}}$

A.3. Direct Central Differentiation for a non-constant grid

One can calculate the optimal coefficients for arbitrary lattices via Taylor expansion, an interesting tool with explanation can be found in [Tay]. Here a direct central differentiation for the second derivative (f”) using directly the closest neighbours (i-1 and i+1) from the original profile (f) is implemented.

$$f_i'' = \frac{2 \cdot f_{i+1}}{(x_{i+1} - x_i) \cdot (x_{i+1} - x_{i-1})} \tag{A.1}$$

$$+ \frac{2 \cdot f_i}{(x_{i-1} - x_i) \cdot (x_{i+1} - x_i)} + \frac{2 \cdot f_{i-1}}{(x_{i-1} - x_i) \cdot (x_{i-1} - x_{i+1})}$$

A.4. Temperature Curvature Matches with EQH

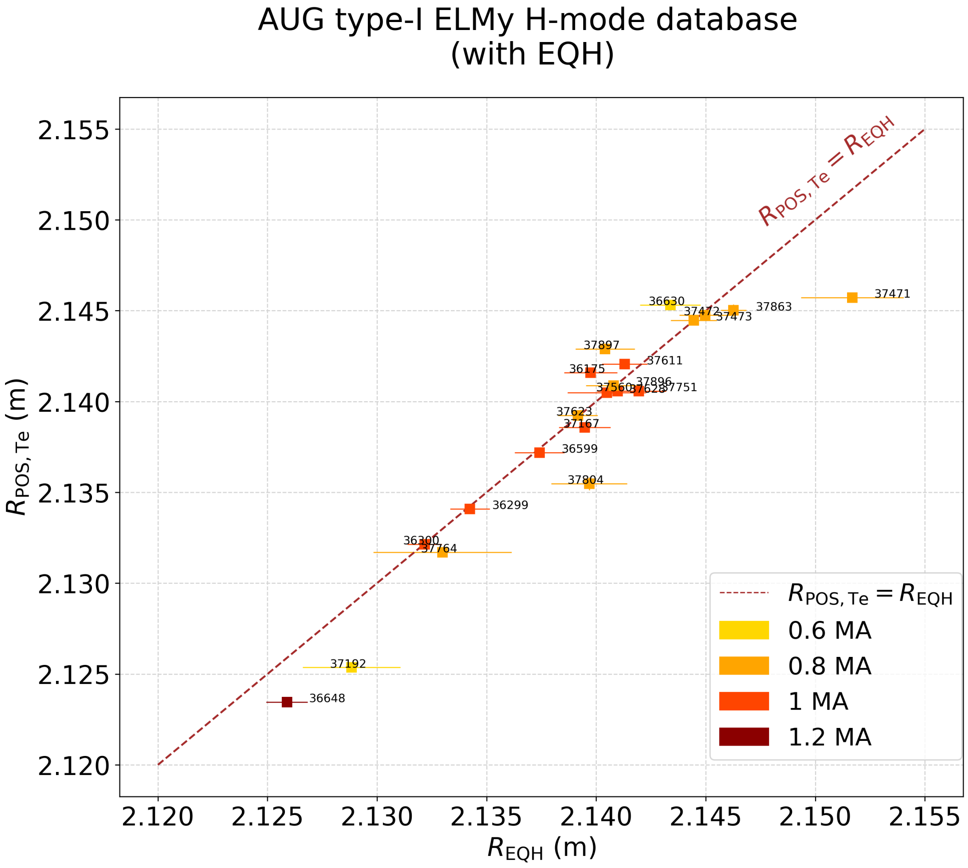

Figure A.5.: Correlation between the separatrix position, read with the equilibria package EQH, and the point of highest positive curvature in the temperature profiles for 21 discharges that compose the built database with the color-coded discharges showing different plasma currents.

A.5. ELM Synchronization (TS)

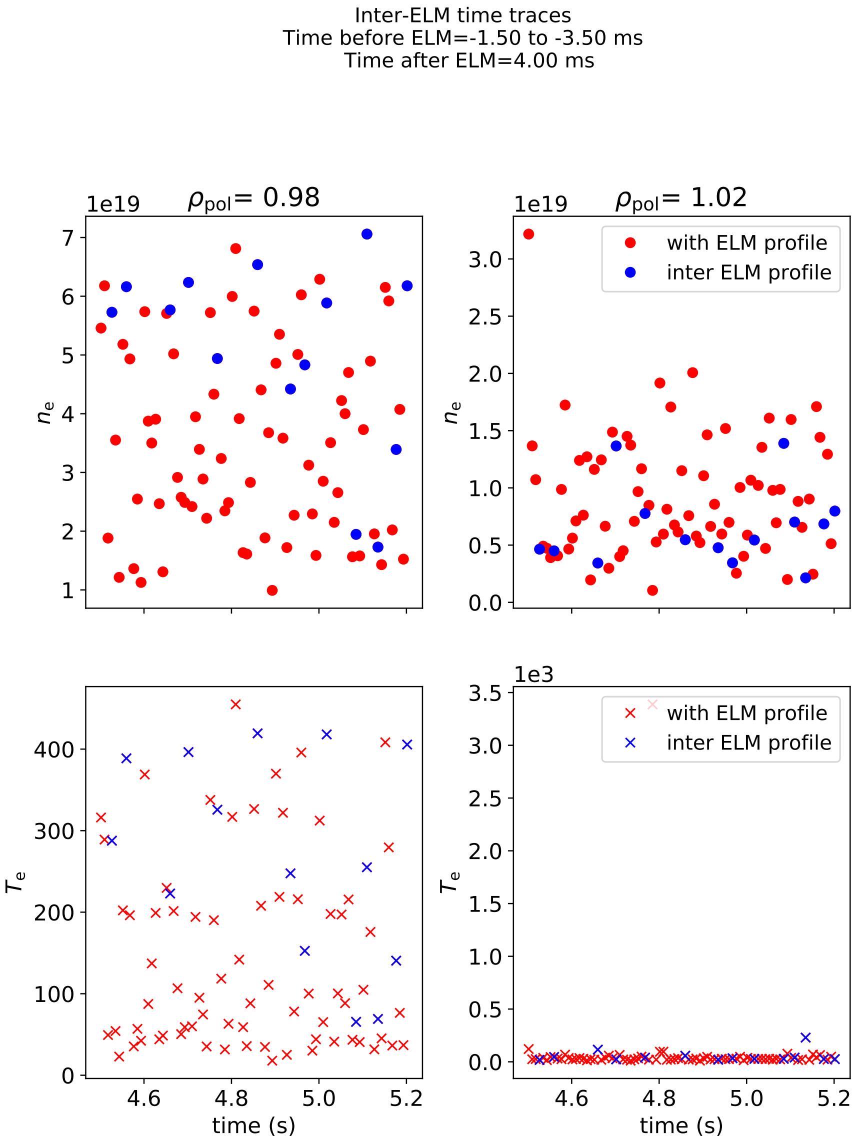

Figure A.6.: ELM Synchronization for the TS Profile for # 36 175. Data is synchronized in time relative to the onset of an ELM defined from −3.5–−1.5 ms relative to the onset time but 4 ms after the previous ELM. The first rows show the density time trace for two different magnetic flux surfaces. The second rows show the temperature time traces. The phases with ELMs are shown in red and the inter-ELM phases in blue.

A.6. Fall-Off Lengths Comparison

Table A.1.: Density decay lengths with data from the both diagnostics studied, Thomson scattering and the thermal helium beam diagnostic (three different fits).

I_p **(MA)**	**Thomson Scattering**	**Thermal Helium Beam**		
	λ_{n_e} **(mm)**	λ_{n_e} **(mm)**		
–	Pedestal-Near SOL	Local	Across-Sep.	λ-averaged
0.8	3,4 ± 0.7	10.7 ± 1.0	10.6 ± 1.1	12.2 ± 2.3
1	11.18 ±1.2	10.9 ±1.3	11.1 ±1.7	10.2 ±1.5

Table A.2.: Temperature decay lengths with data from the both diagnostics studied, Thomson scattering and the thermal helium beam diagnostic.

I_p **(MA)**	**Thomson Scattering**	**Thermal Helium Beam**		
	λ_{n_e} **(mm)**	λ_{n_e} **(mm)**		
–	Pedestal-Near SOL	Local	Across-Sep.	λ-averaged
0.8 MA	10.7 ± 0.3	11.1 ± 1.3	11.1 ± 0.9	20.6 ± 3.7
1 MA	9.1 ±0.8	9.8 ±0.9	10.0 ±1.3	15.6 ±2.3

From the derived values, it can be seen that the fall-off lenghts for the density profiles are similar for the three fittings with THB data, while the values obtained with TS are much lower for the lower current case. For the temperature analysis, similar values are observed between the local fit, the across-separatrix fit and the analysis using the TS diagnostic. The values corresponding to averaged fit are much higher due to the steep drop the temperature profiles suffer at the beginning of the SOL.

A.7. Discharge Selection

Shotnumber	Edition THB, TS	Time (s)	Scenario
36 175	1,1	4.60–4.80	Type I ELMy H-mode
36 299	9	3.45–3.80	Type I ELMy H-mode
36 300	14,1	2.70–3.10	Type I ELMy H-mode
36 599	2,1	3.40–3.70	Type I ELMy H-mode
36 630	1	2.60–2.95	Type I ELMy H-mode
36 648	4	2.50–2.65	Type I ELMy H-mode
37 167	1,1	4.60–4.90	Type I ELMy H-mode
37 192	1,1	2.00–2.30	Type I ELMy H-mode
37 471	1,1	5.00–5.45	Type I ELMy H-mode
37 472	1,1	4.50–5.00	Type I ELMy H-mode
37 473	1	4.00–4.50	Type I ELMy H-mode
37 560	1,1	4.40–4.70	Type I ELMy H-mode
37 611	1	4.10–4.50	Type I ELMy H-mode
37 623	1	5.50–6.00	Type I ELMy H-mode
37 628	1,1	4.00–4.40	Type I ELMy H-mode
37 751	1,1	5.20–5.70	Type I ELMy H-mode
37 764	1	6.60–7.10	Type I ELMy H-mode
37 804	1	5.20–5.50	Type I ELMy H-mode
37 863	1	3.70–3.90	Type I ELMy H-mode
37 896	1,1	2.30–2.80	Type I ELMy H-mode
37 897	1,1	4.00–4.50	Type I ELMy H-mode
35 893	2,1	5.70–5.90	L-mode
36 190	6,1	3.75–4.00	L-mode
36 270	2,1	2.20–2.50	L-mode
36 558	2,1	2.30–2.40	L-mode
36 609	1,1	1.85–2.10	L-mode
37 295	1	1.60–2.00	L-mode
37 741	1,1	2.40–2.90	L-mode
37 763	1,1	2.80–3.10	L-mode
37 769	1	3.20–3.70	L-mode
37 820	2,1	2.10–2.60	L-mode
37 821	1,1	2.80–3.10	L-mode
37 894	1,1	2.65–2.85	L-mode

B. Acknowledgements

I would like to take this opportunity to express my sincere thanks to all those who have helped me during my master's thesis in this complicated year.

First of all I would like to thank my supervisor *Michael Griener*, for all the support and time he has dedicated to me. Whenever I have had a question, whether physical, technical or from the everyday life at the institute, he has always helped me with the best of his disposition. Thanks to him I have been able to know first hand without intermediaries everything I wanted to know about THB diagnostic. I am also very thankful to him for having proof read my thesis so patiently. I am also deeply grateful to my supervisor *Prof. Elisabeth Wolfrum*, for giving me this opportunity. I am very grateful to her for taking the time to guide me through this adventure, always providing me with the tools, advices and suggestions that I needed. I am also very thankful to *Rainer Fischer*, who has taken so much of his time for the evaluation of the discharges presented in this work. In the same way, I am grateful to *Daniel Wendler*, for his help every time I was having a programming doubt and for writing all the calibration shotfiles I needed. Many thanks also to *Dirk Nille*, for all his help on python and for sharing with me his knowledge of Bayesian statistics. I am also very grateful to *Prof. Karl Lackner*, for taking his time to help me to find the physical mechanisms responsible for the experimental results I was observing. I will always be grateful to *Christan Schuster* for having helped me so competent and cordially with the modeling chapter of my thesis. Many thanks also to *Gregor Birkenmeier* for his tutorial exercise classes and for his help in the preparation of the plasma physics seminar. To *Prof. Ulrich Stroth* I am very grateful for all his lectures at TUM, which motivated me to do my master thesis on the field of plasma physics. I am also very grateful to him for giving me access to the IPP. Many thanks too to my colleague and friend *Alberto Castillo*, for all the support he has gave me and for all of our meals together in the I-building. In this adventure I do not want to forget my colleagues and friends *Pablo Ruiz* and *Rosa Arenales*, who together with me decided to come from the UCM in Madrid to study in Munich and have made my days here sunnier. I am also very thankful to my friends in Munich, specially to *Sophia zur Oven* and *Alice Wan* for all the support they have given me. A mi familia, tanto a los que están como a los que no, les estoy completamente agradecida por haberme apoyado siempre. Muchas gracias a mis hermanos *Cristina Díaz* y *Marco Díaz* por estar ahí cuando que lo he necesitado. Especialmente estoy muy agradecida a mi padre *Antonio Díaz* por todos sus consejos y a mi madre *Paloma Esteban* por haberme escuchado y apoyado en todo momento a encontrar mi propio camino.

C. Declaration

I hereby certify that I have written independently for this thesis and used no other than the specified sources, references and resources.

Sofía Díaz Esteban

Munich, 30.5.2021